

Electronic Thesis and Dissertation Repository

10-8-2015 12:00 AM

Inkjet Printed Thin Film Electrodes for Lithium-Ion Batteries

Stephen D. Lawes

The University of Western Ontario

Supervisor

Dr. Andy (Xueliang) Sun

The University of Western Ontario

Graduate Program in Mechanical and Materials Engineering

A thesis submitted in partial fulfillment of the requirements for the degree in Master of Engineering Science

© Stephen D. Lawes 2015

Follow this and additional works at: <https://ir.lib.uwo.ca/etd>

 Part of the [Materials Science and Engineering Commons](#)

Recommended Citation

Lawes, Stephen D., "Inkjet Printed Thin Film Electrodes for Lithium-Ion Batteries" (2015). *Electronic Thesis and Dissertation Repository*. 3252.

<https://ir.lib.uwo.ca/etd/3252>

This Dissertation/Thesis is brought to you for free and open access by Scholarship@Western. It has been accepted for inclusion in Electronic Thesis and Dissertation Repository by an authorized administrator of Scholarship@Western. For more information, please contact wlsadmin@uwo.ca.

INKJET PRINTED THIN FILM ELECTRODES FOR LITHIUM-ION BATTERIES

(Thesis format: Integrated Article)

by

Stephen Lawes

Graduate Program in Mechanical and Materials Engineering

A thesis submitted in partial fulfillment
of the requirements for the degree of
Master of Engineering Science

The School of Graduate and Postdoctoral Studies
The University of Western Ontario
London, Ontario, Canada

© Stephen Lawes 2015

Abstract

With the miniaturization of wireless electronics, the demand for ever-smaller energy storage devices has increased. Thin film batteries can meet this need by providing higher energy densities at smaller scales than conventional lithium-ion batteries. However, the fabrication of thin films batteries by vapor deposition methods typically involves expensive equipment and high temperatures, which limits their commercial application. This thesis reports the development of an inexpensive inkjet printing method of fabricating thin film electrodes for thin film lithium-ion batteries. Inks containing various electrode materials were first developed and optimized in terms of physical properties to ensure ideal jetting conditions. Then, thin film anodes comprised of silicon and titanium dioxide were fabricated with a household inkjet printer and their physical and electrochemical properties were characterized. Critical parameters involved in inkjet printing (e.g. the polymer binder used and the electrode thickness) were thoroughly studied, based on which high-capacity and stable anodes were finally achieved. Overall, this work demonstrates the efficacy and future potential of using inkjet printing for fabricating thin film battery electrodes.

Keywords

Inkjet Printing, Lithium-ion Batteries, Thin Film Batteries, Silicon, Titanium Dioxide, PEDOT:PSS

Co-Authorship Statement

Title: Printing nanostructured carbon for energy storage and conversion applications

Authors: Stephen Lawes, Adam Riese, Qian Sun, Niancai Cheng, and Xueliang Sun

This review paper was organized by Stephen under the guidance of Dr. Xueliang Sun and Dr. Qian Sun. Stephen Lawes wrote the entirety of the manuscript except for the section on fuel cells, which was written by Adam Riese and Niancai Cheng. The parts of this paper used in this thesis were written by Stephen Lawes; no part of this thesis deals with fuel cells. The final version of this manuscript has been published in *Carbon* **2015**, 92, 150-176.

Title: High performance inkjet-printed silicon anodes for lithium-ion batteries

Authors: Stephen Lawes, Qian Sun, Andrew Lushington, Biwei Xiao, Yulong Liu, and Xueliang Sun

The experimental work was carried out by Stephen Lawes under the supervision of Dr. Xueliang Sun and Dr. Qian Sun. The manuscript was organized and written by Stephen Lawes under the guidance of Dr. Xueliang Sun and Dr. Qian Sun. Co-authors contributed by helping with related characterization, providing valuable discussions, and polishing the draft. The final version of this manuscript is to be submitted for peer-reviewed publication.

Title: High performance inkjet-printed titanium dioxide anodes for lithium-ion batteries

Authors: Stephen Lawes, Qian Sun, Hanting Guo, Mohammad Norouzi Banis, and Xueliang Sun

The experimental work was carried out by Stephen Lawes and Hanting Guo under the supervision of Dr. Xueliang Sun and Dr. Qian Sun. The theoretical work was carried out by Stephen Lawes and the manuscript was organized and written by Stephen Lawes under the guidance of Dr. Xueliang Sun and Dr. Qian Sun. Co-authors contributed by helping with related characterization, providing valuable discussions, and polishing the draft. The final version of this manuscript is to be submitted for peer-reviewed publication.

Acknowledgments

Over the past two years that I've spent in Dr. Sun's Nanomaterials and Clean Energy Group, I've had the chance to meet and work with a number of great people. First, I'd like to thank Dr. Andy Sun for providing me with this opportunity and for his full support throughout my master's degree. He always provided guidance and encouragement during my thesis project and is an invaluable resource for anything related to nanomaterials and energy storage and conversion.

I am also grateful to our lab manager and research engineer, Kathy Li. She has always been interested in the well-being of all our group members and her kindness is unending. Her hard work to keep the lab running smoothly has played a large role in the success of this group and she has always been willing to help whenever I needed it.

I would also like to express my greatest thanks to Dr. Qian Sun. He has supervised and guided me from my very first day in the lab and has trained me on nearly everything I know about batteries. Despite his tremendous workload, he has always been available to spare some time for my questions. He is an excellent mentor. Qian is the most knowledgeable person that I know in this field and our many discussions have taught me more than any textbook or course ever could.

I would also like to thank my family for their support throughout my life, both my parents and my brother.

Lastly, thank you to all my friends and fellow lab members who have contributed to making UWO and London a great place to work and live.

Table of Contents

Abstract.....	ii
Co-Authorship Statement.....	iii
Acknowledgments.....	v
List of Tables	ix
List of Figures.....	x
Chapter 1.....	1
1 Introduction and Literature Review	1
1.1 Introduction to Lithium-Ion Batteries.....	1
1.1.1 Fundamental Principles of Lithium-Ion Batteries.....	1
1.1.2 Thin Film Lithium-Ion Batteries.....	3
1.1.3 Anode Materials for Lithium-Ion Batteries	5
1.2 Introduction to Printing Technologies	11
1.2.1 Principles of Inkjet Printing	12
1.2.2 Other Printing Technologies	16
1.3 Battery Electrode Fabrication Methods	20
1.3.1 Conventional Fabrication Methods.....	20
1.3.2 Inkjet Printing of Battery Electrodes	22
1.4 Thesis Objectives	25
1.5 Thesis Organization	26
References	27
Chapter 2.....	36
2 Experimental and Characterization Methods.....	36
2.1 Inkjet printing of nanomaterials.....	36

2.1.1	Ink preparation	36
2.1.2	Inkjet printing.....	38
2.2	Characterization methods.....	39
2.2.1	Physical and compositional characterization	39
2.2.2	Electrochemical characterization	42
	References	45
Chapter 3	46
3	High performance inkjet-printed silicon anodes for lithium-ion batteries.....	46
3.1	Introduction.....	46
3.2	Methods.....	48
3.2.1	Silicon ink preparation	48
3.2.2	Electrode and coin cell preparation.....	48
3.2.3	Characterization	49
3.3	Results.....	49
3.3.1	Electrode fabrication and physical characterization	49
3.3.2	Electrochemical performance	51
3.3.3	Physical characterization	55
3.4	Discussion.....	57
3.5	Conclusions.....	59
	Acknowledgements	60
	References	60
	Supporting Information.....	65
Chapter 4	70
4	High performance inkjet-printed titanium dioxide anodes for lithium-ion batteries ...	70
4.1	Introduction.....	70

4.2	Methods.....	72
4.2.1	TiO ₂ ink preparation	72
4.2.2	Electrode and coin cell preparation.....	73
4.2.3	Characterization	73
4.3	Results and Discussion	74
4.3.1	Printing process and morphological characterization of the inkjet-printed thin films.....	74
4.3.2	Structural and compositional characterization of the inkjet-printed thin films	76
4.3.3	Electrochemical characterization	78
4.4	Conclusions.....	83
	Acknowledgements	83
	References	84
	Chapter 5.....	88
5	Conclusions and Future Work.....	88
5.1	Conclusions.....	88
5.2	Recommendations for Future Work.....	90
	References	91
	Curriculum Vitae	93

List of Tables

Table 1.1. Alloys of silicon and lithium with their respective unit cell volumes. Data gathered from [23].	8
Table 1.2. Comparison of the four printing techniques discussed in this chapter.	20

List of Figures

Figure 1.1. Schematic illustration showing the basic operating principles of LIBs [2].....	2
Figure 1.2. Cross-sectional schematic illustration of a TFB.....	3
Figure 1.3. Weight and volume percentages of the different components in a typical LIB. Data gathered from [4, 7].....	4
Figure 1.4. Volumetric and gravimetric energy densities of different types of batteries [4].	5
Figure 1.5. The specific capacities and operating voltages of various anode materials for LIBs.....	6
Figure 1.6. Plot showing how the full cell theoretical specific capacity is related to the capacity of the anode, for a cell with a silicon anode and LiCoO ₂ cathode [30].....	9
Figure 1.7. Crystal structures of TiO ₂ polymorphs commonly used for LIB anodes [33].	11
Figure 1.8. Schematic illustration of the inkjet printing process [47].	13
Figure 1.9. Influence of ink properties on (a) droplet formation [57] and (b) droplet spreading [58]. The shaded area in (b) is the region of high quality inkjet printing.	15
Figure 1.10. Schematic illustration of screen printing [46].	18
Figure 1.11. Schematic illustration of the transfer printing process [84].	19
Figure 1.12. Standard electrode fabrication process for LIBs [94].....	21
Figure 1.13. Schematic illustration of the inkjet printing process for battery electrodes.	23
Figure 1.14. SEM images of the (a) surface and (b) cross-section of an inkjet-printed LTO anode (the inset is a TEM image of LTO particles in the film) [38].	24

Figure 1.15. (a) Graphene/TiO ₂ ink for printing flexible thin film LIB electrodes. (b) Schematic diagram showing the major components of the cell. (c) Demonstrating the flexibility of a printable graphene electrode [97].	25
Figure 2.1. A schematic illustration (left) and photo (right) of the U-tube viscometer used to measure ink viscosity.	37
Figure 2.2. Injecting a silicon ink solution into an HP 61 ink cartridge (left) and the HP Deskjet 2540 inkjet printer used to print LIB anodes (right).	38
Figure 2.3. A photo of the Hitachi S-4800 field emission SEM equipped with an EDX spectrometer.	40
Figure 2.4. A photo of the Bruker D8 Advance XRD instrument.	40
Figure 2.5. A photo of the Nicolet 6700 FTIR spectrometer.	41
Figure 2.6. A photo of the HORIBA Scientific LabRAM HR Raman spectrometer.	41
Figure 2.7. A photo of the TA Instruments SDT Q600 TGA.	42
Figure 2.8. A photo of the Arbin BT-2000 battery test station.	44
Figure 2.9. A photo of the VMP3 multichannel potentiostat 3/Z for CV and EIS measurements.	45
Figure 3.1. Procedure used to print SiNP anodes on copper foil. (a,b) First, the ink was prepared by mixing SiNPs, carbon black, and the polymer binder in water. (c) After 3 hours of sonication, the solution was well-mixed and (d) injected into an inkjet printer cartridge and printed. (e) Photograph of the Western University logo printed with the SiNP ink. (f) Optical photographs and SEM images of the inkjet-printed SiNP anode films on copper foil. Scale bars red, white, and black represent 3 cm, 5 cm, and 500 nm, respectively.	51
Figure 3.2. (a) Cycling performance of inkjet-printed silicon anodes prepared with different polymer binders at 0.1C. (b) Voltage profiles of selected cycles for the	

PEDOT:PSS (DMC:FEC) cell from (a). (c, d) Rate capability measurements of Si anodes with PEDOT:PSS binder in DMC:FEC electrolyte. (e) Limited depth-of-discharge tests performed to a capacity cut-off of 1000 mAh g⁻¹. The Coulombic efficiency shown is for PEDOT:PSS (DMC:FEC). (f) Voltage profiles of selected cycles for the PEDOT:PSS (DMC:FEC) cell shown in (e)..... 54

Figure 3.3. Ex-situ (a) SEM images and (b) FTIR spectra of SiNP anodes with PEDOT:PSS binder taken at three stages of a discharge/charge cycle: before cycling (pristine), after first discharge (lithiated), and after first full discharge and charge (delithiated). The green highlighted regions in the FTIR spectra indicate the PEDOT:PSS thiophene C=C and C-S stretching vibrations, the blue highlighted regions indicate SEI formation and residual electrolyte salt, and the purple highlighted regions indicate the sulfonic acid groups. (c) The structure of PEDOT:PSS. Scale bars are 500 nm. 57

Figure 3.4. Schematic illustration of the proposed mechanism explaining the electrochemical performance of anodes prepared with different binders. The use of non-conductive binders (CMC, Na-alginate, and PVP) leads to electrical isolation of SiNPs. In the case of CMC and Na-alginate, electrical isolation occurs from the start, leading to poor initial capacity, while in the case of PVP the conductive carbon black network is destroyed during large volume changes. With PEDOT:PSS, the SiNPs remain electrically connected throughout charging/discharging and are therefore able to maintain a stable cycling capacity. 59

Figure S3.1. (a) Photographs of printed films with different numbers of printing passes. Too few passes (10x) results in non-uniform films that cannot be used for electrodes. More passes (25x and 40x) result in uniform films. However, too many passes decreases capacity. (b) Discharge capacity of Si anodes with PEDOT:PSS binder and DMC:FEC electrolyte, with different numbers of printing passes..... 65

Figure S3.2. EDX mapping of inkjet printed Si films with four different binders, each prepared with 25 printing passes. The top images show the SEM image of where the mapping was performed and the bottom images show the EDX mapping for Si. All four

films show uniform Si dispersion throughout, with some fluctuations due to variations in the surface morphology. Scale bars are 2 μm 65

Figure S3.3. Cycling performance of Si anodes with PEDOT:PSS binder and DMC:FEC electrolyte at 1 C. The average CE over 2000 cycles is 99.8%. 66

Figure S3.4. EIS spectra of inkjet printed SiNP anodes prepared with PEDOT:PSS binder. Cells were fabricated with EC:DEC:EMC electrolyte. The electrode starts with relatively high impedance that decreases during cycling. This may be due to increased electrolyte wetting of the printed anode layers and the higher conductivity of Li-doped Si, as discussed in [30]. 66

Figure S3.5. Raman spectra taken at three stages of a discharge/charge cycle: before cycling (pristine), after one discharge cycle (lithiated), and after one full discharge/charge cycle (delithiated). The peak at 1435 cm^{-1} represents thiophene ring stretching vibrations, from the thiophene ring present in the PEDOT molecules. Similar to the C=C and C-S thiophene stretching shown in the FTIR spectra, the thiophene ring stretching peak disappears after lithiation, due to stretching being inhibited by the already stretched polymer chains. However, after delithiation there is no return of this peak. This may be due to the SEI binding to the PEDOT molecules and preventing further stretching of the thiophene rings. 67

Figure S3.6. TGA of a film of inkjet printed SiNP anode material prepared with PEDOT:PSS binder, used to determine the mass percentage of Si in the printed films. Since Si is stable in the temperature range used here, all mass loss is due to the removal of the polymer binder and carbon black. We therefore used the minimum point (46%) on the curve as the % mass of Si in the anode for calculating charge/discharge rates and capacities. To confirm that this assumption was valid, we also measured a sample of Si powder. No mass loss was observed; in fact, oxidation of the SiNPs resulted in a mass gain. This increase is negligible (2%) at the minimum point of the printed Si anode curve and will anyways result in lower reported capacity values. 68

Figure S3.7. Cyclic voltammetry curves of inkjet printed SiNP anodes prepared with four different binders. All cells were fabricated with EC:DEC:EMC electrolyte.....	69
Figure 4.1. Ink solutions prepared with three different polymer binders: (a) PVP, (b) PVDF, and (c) PEDOT:PSS. (d) Optical image of the TiO ₂ nanoparticle solution with PEDOT:PSS binder inkjet-printed on copper foil with 25 layers. SEM images of the printed film (e) before and (f) after cycling.....	75
Figure 4.2. Cross-sectional SEM images of TiO ₂ films printed with different number of layers.....	76
Figure 4.3. XRD patterns of inkjet-printed TiO ₂ films before and after cycling. A reference of TiO ₂ powder is shown for comparison. Peaks marked with an asterisk (*) are from the underlying copper foil substrate.....	77
Figure 4.4. TGA curves of an inkjet-printed TiO ₂ anode and each of its components individually.....	78
Figure 4.5. (a) Galvanostatic cycling at 0.1C and (b) EIS measurements of three inkjet-printed TiO ₂ anodes with different thicknesses, controlled by the number of printed layers. 15 layers = 1.9 μm, 25 layers = 3.0 μm, and 35 layers = 4.4 μm.....	80
Figure 4.6. (a) Rate capability of a TiO ₂ -25 anode and (b) the corresponding 2 nd -cycle charge and discharge voltage profiles at each different current rate. (c) Long-term cycling performance of TiO ₂ -25 anodes at varying charge/discharge rates.....	81
Figure 4.7. (a) CV scans of inkjet-printed TiO ₂ anodes at varying scan rates. (b) Plot of peak current vs. square root of the scan rate for both anodic (top) and cathodic (bottom) peaks.....	82

Chapter 1

1 Introduction and Literature Review

*Parts of this chapter have been published in *Carbon*, vol. 92, pp. 150-176, **2015**.

1.1 Introduction to Lithium-Ion Batteries

Lithium-ion batteries (LIBs) were first commercialized by Sony in 1991. Today, LIBs are the most widely-used portable energy storage devices, with the global market estimated to grow from \$15 billion in 2012 to \$32 billion in 2016 to \$76 billion in 2020 [1]. LIBs have been adopted for a variety of portable electronics, such as cell phones, cameras, and laptops, and are becoming increasingly used in electric vehicles. This is due to their unique merits of high energy density, low self-discharge rate, no memory effect, and relatively low price.

1.1.1 Fundamental Principles of Lithium-Ion Batteries

LIBs are comprised of electrochemical cells connected in series and/or parallel to achieve a desired voltage and capacity. A typical cell is made of two electrodes separated by a separator and electrolyte, through which lithium ions can travel. Commercial LIBs are typically composed of a graphite negative electrode (anode) and a lithium metal oxide positive electrode (cathode) separated by a polymer separator immersed in a nonaqueous liquid electrolyte (Figure 1.1). During charging, lithium ions are extracted from the cathode, migrate through the electrolyte, and intercalate between graphite layers in the anode, forming LiC_6 . During discharge, the reverse electrochemical reaction occurs – lithium ions deintercalate from the graphite and reinsert into the cathode. These processes produce and consume electrons via oxidation and reduction reactions, respectively. The electrons are then free to move around the external circuit, storing their energy as chemical potential energy (charging) or supplying energy to an external load (discharging).

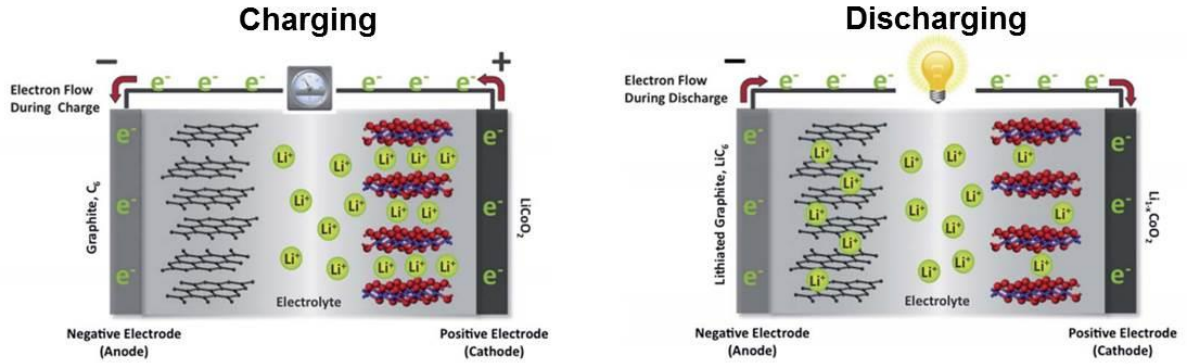


Figure 1.1. Schematic illustration showing the basic operating principles of LIBs [2].

The half-reaction at the anode is given by:



And the half-reaction at the cathode is given by:



The overall cell reaction is given by:



where the forward direction is charging and the reverse direction is discharging. MO_2 is a transition metal oxide, typically CoO_2 , but occasionally NiO_2 , MnO_2 , or $FePO_4$.

The miniaturization of electronic devices over the last thirty years has led to an increased demand for smaller energy sources. However, a smaller battery inherently contains less electrochemically active material, reducing the amount of energy that can be stored. And as devices such as laptops, wireless sensors, and medical implants become smaller and more complex, they require more energy to operate. This compounding problem of size reduction with increased energy demand has fueled intensive research in the field of portable energy storage. The United States Department of Energy (DOE) has set a target energy density for lithium-ion batteries (LIBs) of 750 Wh/L by 2020 [3]. There are two main approaches that researchers are using to meet this goal: (1) designing novel fabrication techniques to load more material into a cell and (2) developing new materials

with higher energy densities. This thesis will aim to combine both of these methods, by developing a technique for fabricating thin film batteries comprised of novel anode materials for next-generation LIBs.

1.1.2 Thin Film Lithium-Ion Batteries

As portable electronics decrease in size, a need has arisen for more compact batteries. Oftentimes, the size of a device is limited by the size of its battery; it cannot be made smaller without major tradeoffs in battery life. Over the past two decades, many studies have focused on reducing the size of LIBs while maintaining their capacity [4, 5]. Thin film batteries (TFBs) have been developed to meet this challenge, with the first lithium TFB reported in 1983 [6]. A schematic illustration of the design of a typical TFB is shown in Figure 1.2.

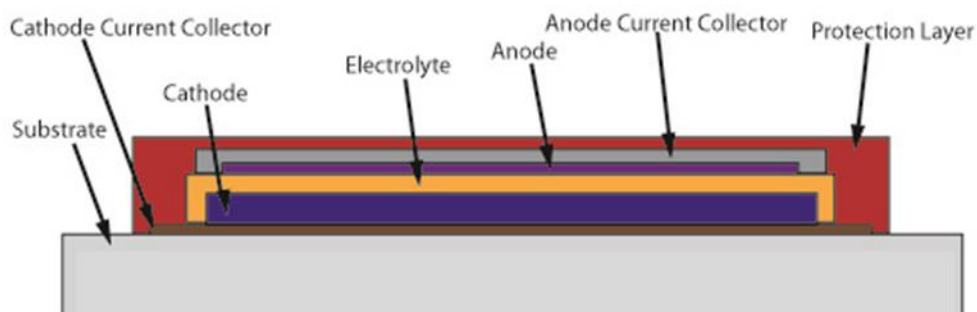


Figure 1.2. Cross-sectional schematic illustration of a TFB.

The various components of TFBs are typically on the order of microns to hundreds of microns thick, giving a full cell thickness on the order of millimeters or less. Because of their reduced size, TFBs are fundamentally comprised of less material. This includes both the electrochemically active materials and the inactive components.

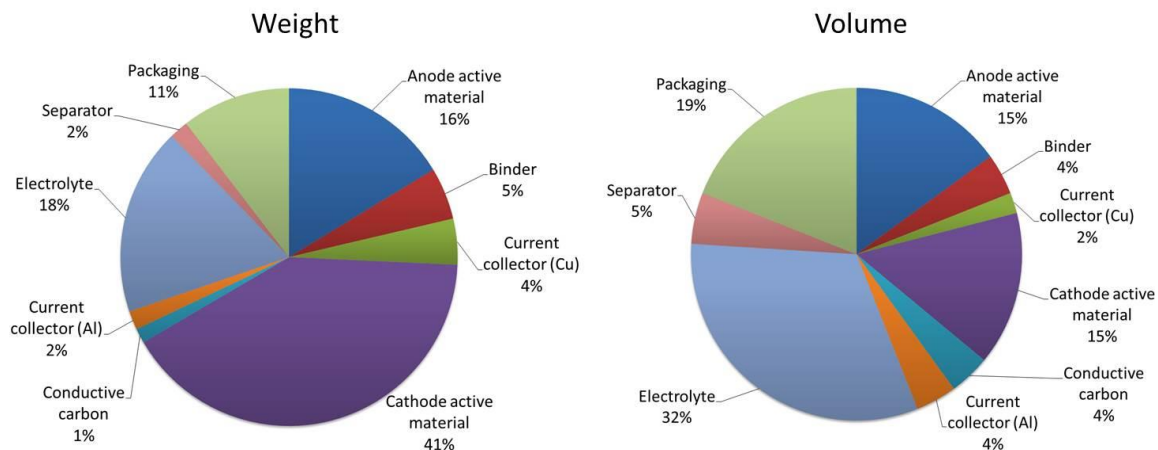


Figure 1.3. Weight and volume percentages of the different components in a typical LIB. Data gathered from [4, 7].

Typical weight and volume percentages of the various battery components are shown for a standard LIB in Figure 1.3. As shown, the active materials account for only 57.4% of the total weight and 30% of the total volume, while the cell packaging, electrolyte, and other inactive materials account for 42.6% of the weight and 70% of the volume. In TFBs, a solid-state electrolyte is typically used, which can contribute to reducing both the weight and volume of the electrolyte and eliminating the need for a separator and excessive packaging to properly contain a liquid electrolyte. Thus, the total loading percentage of active materials is increased, resulting in higher volumetric and gravimetric energy densities, as shown in Figure 1.4.

Although the energy density can be improved by using TFBs, a number of challenges still exist. A shorter distance between electrodes makes the battery more likely to short circuit, a major safety concern [8]; the use of a solid-state electrolyte can prevent this problem, but results in lower lithium-ion diffusion rates. And mechanical stresses during cycling of the battery may cause the layers to separate from one another, resulting in poor cycle life [9, 10]. The fabrication of TFBs can also pose a problem due to adhesion issues between the various layers as well as the temperature limits of the substrate [11]. Conventional methods for fabricating full TFBs or thin film electrodes for TFBs mainly include sputtering [12, 13], chemical vapor deposition [14, 15], pulsed laser deposition [16, 17], spin coating [18], and sol-gel methods [19, 20]. However, these can require

expensive equipment, high temperatures, and/or post-annealing treatments that can damage the films and the substrate. Therefore, a facile and cost-efficient method of thin film electrode fabrication for LIBs is in high demand. Standard fabrication methods for LIBs and thin film LIBs are discussed in more detail in section 1.3.

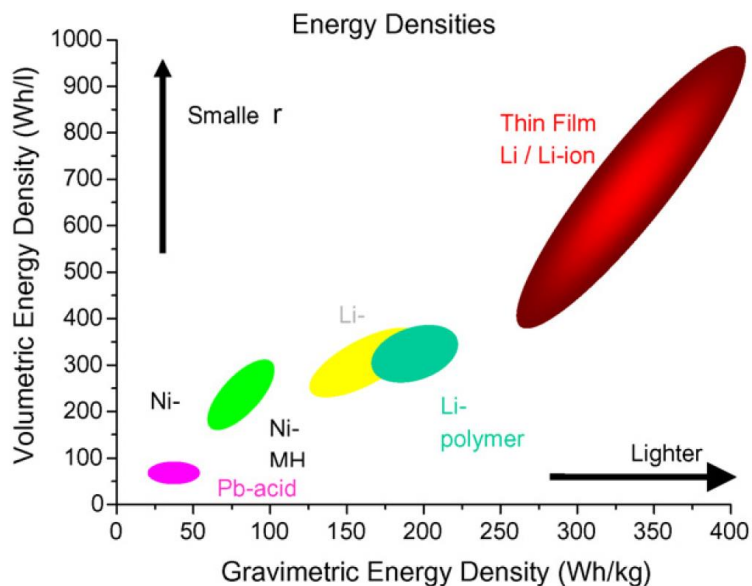


Figure 1.4. Volumetric and gravimetric energy densities of different types of batteries [4].

1.1.3 Anode Materials for Lithium-Ion Batteries

Graphite has been the most common anode material for LIBs over the past two decades due to its decent specific capacity, long cycle life, chemical stability, low cost, and flat working potential. However, as LIBs are used for new applications requiring high energy outputs, particularly electric vehicles and household energy storage, a number of problems with graphite anodes have arisen. First, the theoretical capacity of graphite (372 mAh g^{-1}) is not sufficient to achieve the high energy densities required for future demands. Second, graphite's relatively low lithium-ion diffusion rate limits its cycling performance at high current densities and therefore its power density [21]. And third, when a LIB is fully charged, the graphite anode becomes lithiated and has a similar reactivity to lithium metal [22]. Upon catastrophic failure of the cell, a highly exothermic

reaction can take place, leading to ignition of the flammable electrolyte and a possible explosion, which is a major safety concern. Therefore, new anode materials with higher specific capacities, higher rate capabilities, and improved safety are needed.

A number of alternative anode materials have been intensively developed and studied over the past decade, and are shown in Figure 1.5. The anode's specific capacity and working potential are both important to developing cells with high energy density. We want to maximize the capacities of the anode and cathode as well as the potential difference between them to maximize the energy density. However, these are not the only considerations when choosing an electrode material. Cycle life, rate capability, cost, and safety must also be taken into account. For example, lithium metal has a very high theoretical specific capacity of 3860 mAh g^{-1} . However, dendrite formation, chemical reactivity, and safety concerns have so far prevented its widespread adoption in rechargeable batteries.

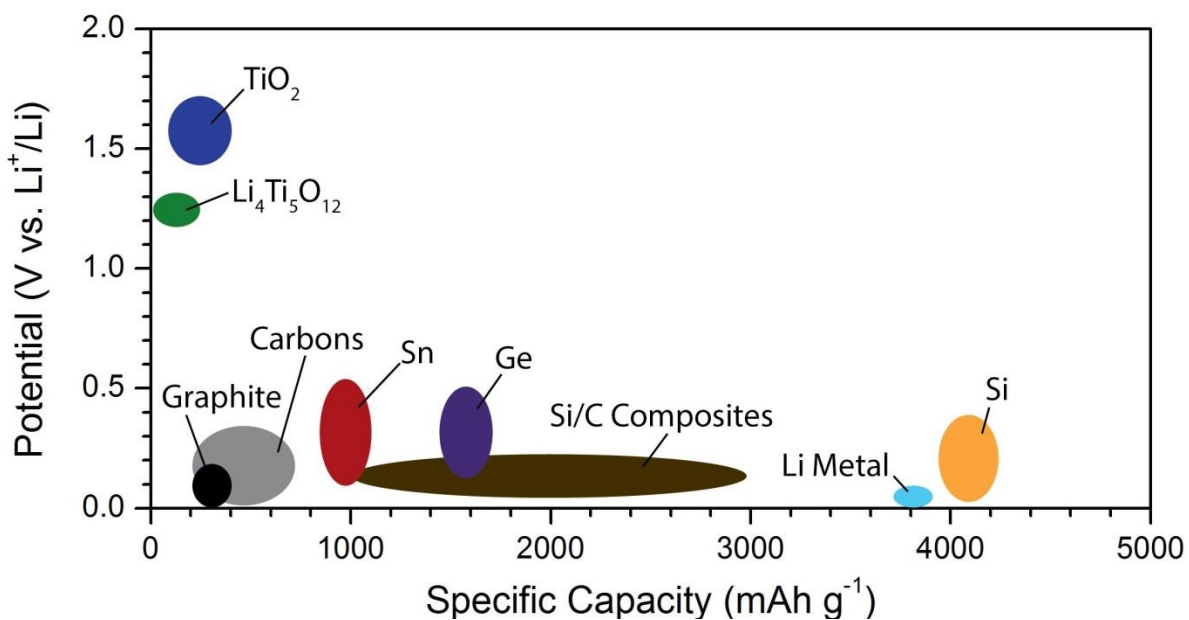


Figure 1.5. The specific capacities and operating voltages of various anode materials for LIBs.

The criteria for LIB anode materials are summarized as follows:

- (1) **High specific capacity.** This results in a higher energy density of the cell.

- (2) **Low working potential.** A greater difference between the anode and cathode working potentials leads to higher energy density of the cell.
- (3) **Long cycling life (high Coulombic efficiency).** The capacity must not fade too rapidly during cycling to ensure the cell can be charged/discharged for hundreds or thousands of cycles.
- (4) **High rate capability.** The cell must be able to be charged and discharged in a reasonable amount of time
- (5) **Chemical stability.** The anode material should not continuously react with the electrolyte or undergo other side reactions within the electrochemical window of the cell.
- (6) **Low cost.** For commercial purposes, the cost of the material and processing must be justified by the cell's performance.
- (7) **Safety.** The anode material should have low toxicity and not react violently when exposed to the atmosphere.

The definitions of “high specific capacity” or “long cycling life”, for example, depend on the particular application and there are typically trade-offs between these criteria. As examples, cycling at higher rates tends to decrease the cycling life, and safer anode materials usually operate at higher potentials. It is important to understand the needs of the specific application when choosing or developing an anode material.

In this thesis, two promising candidates for next-generation LIB anodes are investigated by inkjet printing fabrication technology: silicon and titanium dioxide. The advantages and challenges of using these alternative anode materials in LIBs are introduced here.

1.1.3.1.1 Silicon Anodes

Silicon shows great potential to be used as an anode material for LIBs in the near future. It possesses a very high theoretical capacity of 4200 mAh g^{-1} , due to its ability to alloy with up to 4.4 lithium atoms per silicon atom. Silicon also has a long discharge plateau at a low operating voltage, providing a stable voltage while discharging. In addition, it is

nontoxic and is one of the most abundant elements in the earth's crust, making it an economical choice for LIB anodes.

Unlike graphite and titanium dioxide, silicon forms alloys with lithium at different stages of the charging and discharging processes. The half-reaction at the anode is given by:



where x is the molar ratio of lithium to silicon and varies from 0 to 4.4. The forward direction is charging and the reverse direction is discharging. Silicon forms four distinct alloys with lithium during electrochemical cycling, which are given in Table 1.1 along with their respective unit cell volumes.

Table 1.1. Alloys of silicon and lithium with their respective unit cell volumes. Data gathered from [23].

Compound	Crystal Structure	Unit Cell Volume (\AA^3)
Si	Cubic	160.2
$Li_{12}Si_7$ ($Li_{1.71}Si$)	Orthorhombic	243.6
$Li_{14}Si_6$ ($Li_{2.33}Si$)	Rhombohedral	308.9
$Li_{13}Si_4$ ($Li_{3.25}Si$)	Orthorhombic	538.4
$Li_{22}Si_5$ ($Li_{4.4}Si$)	Cubic	659.2

As can be seen, the alloying process leads to a volume expansion up to 400% of the initial volume of silicon upon full lithiation. This creates large internal stresses in the silicon particles, leading to pulverization of the electrode and loss of electrical contact due to repeated volume expansion and contraction during cycling. This ultimately results in very short lifetimes for silicon anodes and has so far prevented their widespread adoption. A lot of research has focused on developing novel nanostructured silicon electrodes, such as nanowires [24], nanotubes [25], hollow nanospheres [26], and core-shell structures [27, 28] to overcome the poor cycling stability of silicon.

Thin film silicon electrodes may alleviate this problem by limiting the total volume expansion of the electrode and increasing the critical fracture stress, according to the Griffith-Irwin equation [29]:

$$\sigma_{fracture} = \frac{K_{Ic}}{\sqrt{\pi h}} \quad (1.5)$$

where $\sigma_{fracture}$ is the critical fracture stress, K_{Ic} is the fracture toughness of the material, and h is the thickness of the film. Based on this, thinner films require greater stress to fracture and therefore have better cycling stability than thicker films.

In the design of LIBs, limiting the specific capacity to a lower depth of discharge (DOD) in order to increase the cycle life is acceptable. In fact, above a certain point, increasing the capacity of the anode does not increase the capacity of the full cell significantly. Figure 1.6 shows the theoretical capacity of a full cell with a silicon anode and LiCoO_2 cathode as a function of the capacity of the silicon anode. From this graph, it is clear that only minor gains are made by increasing the capacity of the silicon negative electrode above about 1000 mAh g^{-1} . Therefore, limiting the anode's capacity to increase the lifetime will not significantly reduce the cell's overall capacity. Until higher capacity cathodes are developed, this should be considered an acceptable tradeoff. For these reasons, silicon is considered a very promising candidate for the next generation of LIBs.

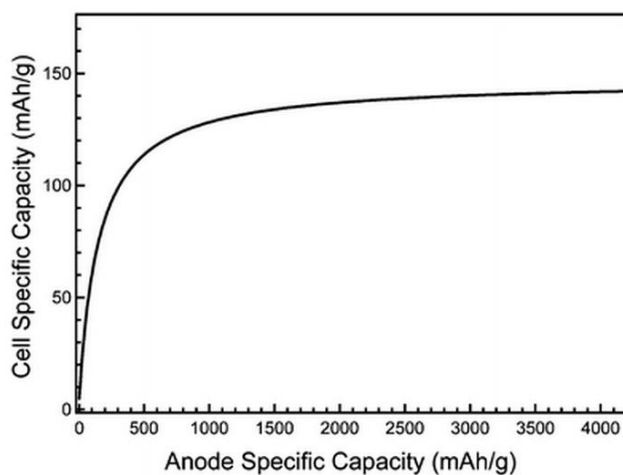


Figure 1.6. Plot showing how the full cell theoretical specific capacity is related to the capacity of the anode, for a cell with a silicon anode and LiCoO_2 cathode [30].

1.1.3.1.2 Titanium Dioxide Anodes

Titanium dioxide (TiO_2) is another promising anode material for LIBs in applications where safety is a primary concern or where high current densities are required. This is because TiO_2 anodes have a high working potential (1.5-1.8 V vs. Li/Li^+), meaning that side reactions with the electrolyte and lithium deposition on the Cu current collector are avoided, unlike with graphite anodes. Furthermore, during lithium insertion TiO_2 undergoes a volume change of only 4% [31], making it very stable at high cycling rates and results in long cycle lives.

TiO_2 is an intercalation-type compound, in which lithium ions can insert into and be stored in its crystal structure. The half-reaction at the anode is given by:



where x is the insertion coefficient. The forward direction is charging and the reverse direction is discharging. In theory, TiO_2 can host up to 1 mole of lithium per mole of TiO_2 , corresponding to a theoretical capacity of 335 mAh g^{-1} . However, experimentally lower insertion coefficients are measured, due to anisotropic and slow lithium-ion diffusion rates in lithiated TiO_2 [32].

There are four different crystal structures of TiO_2 that have been used as LIB anode materials (Figure 1.7). For bulk anatase and rutile TiO_2 , which are the most studied for LIBs, the maximum insertion coefficients are 0.5 and 0.1, respectively [34]. These values correspond to capacities of 167.5 mAh g^{-1} and 33.5 mAh g^{-1} , respectively, which are much lower than that of graphite. However, the capacity dramatically increases when TiO_2 is made into nanostructures, due to a larger electrode/electrolyte interfacial area and shorter electron and lithium ion diffusion lengths in nano-sized TiO_2 [33]. Nanoparticles of anatase and rutile TiO_2 are reported to have maximum capacities of 285 and 251 mAh g^{-1} , respectively.

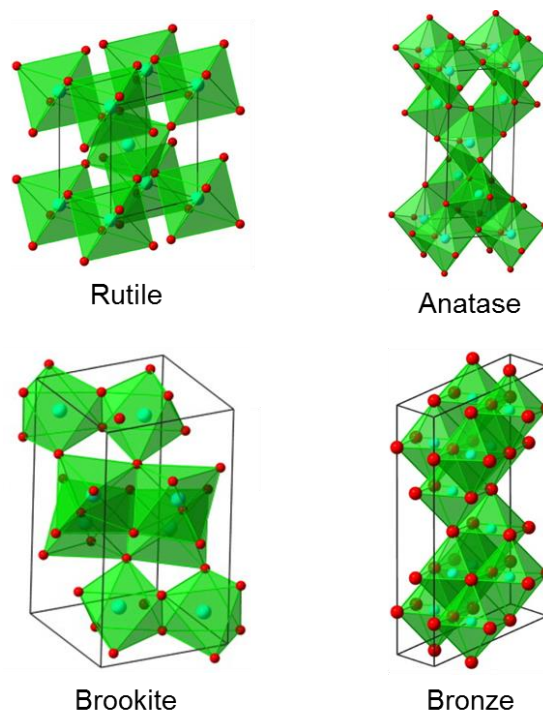


Figure 1.7. Crystal structures of TiO₂ polymorphs commonly used for LIB anodes [33].

At first glance, it may appear that the low capacity of TiO₂ makes it an unattractive anode material for LIBs. However, its low volume expansion, high stability, and the ability to easily tailor its structure make it a great candidate for long-life and high-rate LIBs, which cannot be achieved with other anode materials.

1.2 Introduction to Printing Technologies

The fundamental principles of four major printing technologies are introduced here. Inkjet printing is by far the most common of these techniques for depositing nanomaterials onto substrates of varying size, surface energy, and flexibility. Screen printing and transfer printing are popular for specific applications (e.g. in the textile industry and for flexible electronics), while 3D printing is an emerging technology with the potential to replace many conventional prototyping and manufacturing processes.

1.2.1 Principles of Inkjet Printing

Inkjet printing is an additive technique for patterning two-dimensional structures onto a substrate. It precisely deposits ink droplets at desired locations without pre-patterning the substrate, making it simple to use while minimizing wasted material. It has been widely adopted in industry as a rapid fabrication technique that can be used on a variety of substrates, with applications ranging from advertisements to printed circuit boards.

Inkjet printing has also been successfully applied to fabricating energy storage and conversion devices, such as battery electrodes [35-40], supercapacitors [41-45], and solar cells [46-50]. It can be used to fabricate thin films or patterns of uniform thickness, which can be controlled by the number of layers printed on top of one another. Inkjet printing technology has many advantages over other fabrication techniques, including cost-effectiveness, ease of use, minimal wasted material, scalability, and the ability to deposit designed patterns.

Principally, inkjet printing can be divided into continuous inkjet (CIJ) and drop-on-demand (DOD) methods. CIJ printing involves pumping liquid ink through a nozzle where a continuous stream of droplets is formed by a vibrating piezoelectric crystal. Some droplets are charged by passing them through an electric field, which can be varied to control the degree of charging. The droplets then pass through another electric field, with the more highly charged droplets deflecting more than those with a lesser charge. In this way an image can be produced, with unused ink being collected in a gutter and recycled. On the other hand, DOD printers eject material only when required. This involves forcing ink out of a series of nozzles mounted on a print head. Because DOD printers do not recycle ink, which may result in degradation upon exposure to atmosphere, they are the standard choice for printing functional materials. In addition, DOD printing generally wastes less material; it is therefore a more suitable technique for printing expensive materials.

The three main stages of inkjet printing are illustrated in Figure 1.8: droplet ejection, droplet spreading, and droplet solidification. The print head is first moved to the desired position, where droplets are ejected through the nozzle and travel to the substrate. Upon

impact, they spread along the surface and join with other droplets, forming a thin film of liquid ink. Finally, the solvent evaporates, leaving the solid contents of the ink remaining on the substrate.

To achieve droplet ejection in DOD printers, there are two main types of inkjet print heads: thermal and piezoelectric. Thermal print heads contain a resistor inside the ink chamber which, upon an applied voltage, will superheat the ink above the bubble nucleation temperature. The bubble expands, forcing ink out of the chamber and through the nozzle. Once the ink is ejected, the chamber rapidly cools, allowing more ink to refill the chamber. This entire process occurs within a few microseconds [51]. Piezoelectric inkjet print heads, on the other hand, contain a piezoelectric element that pulsates upon electrical excitation, which forms a pressure wave that forces ink out of the chamber. The vibration of the piezoelectric material can be precisely tuned to control droplet ejection from the nozzle. Typically, inkjet print heads comprise of hundreds of ink chambers and nozzles to achieve high throughput. A higher number of nozzles allows for printing of higher resolution patterns in shorter time frames, an important metric for large-scale production.

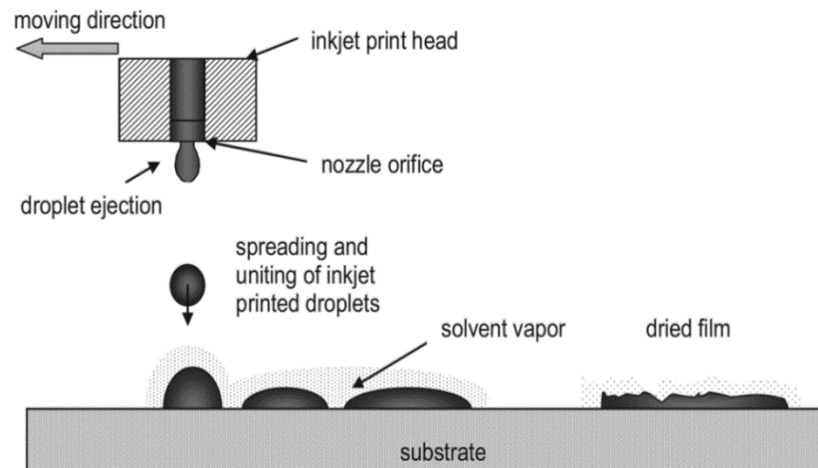


Figure 1.8. Schematic illustration of the inkjet printing process [47].

Thermal print heads are generally cheaper and require less maintenance than piezoelectric print heads because they contain no moving parts. The cartridge on which the print heads are mounted can simply be replaced by the user for relatively low cost if

the nozzles become clogged or broken. Piezoelectric print heads, however, typically require more expensive maintenance procedures by a technician if their piezoelectric crystals become damaged. On the other hand, piezoelectric print heads are preferable for printing a wide range of functional materials since they do not require any heating of the ink, which can result in degradation of active material in the ink. In addition, a wider range of solvents can be used with the piezoelectric systems, including water, oils, and organic solvents; thermal print heads are generally limited to aqueous inks due to the nucleation temperature required for droplet ejection. Also, the viscosity, surface tension, and density of the ink must be more precisely controlled when using thermal print heads. Typically the ink viscosity should be approximately 10 cP [52, 53]. Therefore, piezoelectric print heads are more commonly used for inkjet printing of nanomaterials due to their versatility in terms of the ink's composition and physical properties.

For both types of print head, droplet ejection is dependent on the viscosity, surface tension, and density of the ink, the shape and size of the nozzle, and the ejection velocity of the droplet. These parameters are described by the Reynolds (Re), Weber (We), and Ohnesorge (Oh) numbers. As shown in Figure 1.9a, there is a region in which Re , We , and Oh are optimized for ideal jetting. In the figure, Z is defined as the reciprocal of the Ohnesorge number, $1/Oh$. Generally, high Z fluids (high viscosity, low surface tension) will be unable to form droplets that can eject from the nozzle, whereas low Z inks (low viscosity, high surface tension) will result in the formation of satellite droplets. Satellite droplets lead to blurred line edges and misplaced drops, ultimately leading to lower resolution. Therefore, when developing an ink formulation it is important to control these physical properties with the addition of surfactants, thickeners, stabilizers, and other additives.

The second stage of inkjet printing is droplet spreading, which is dependent on the interactions between the ink and the substrate. When the droplet contacts the surface of the substrate, inertial and capillary forces will influence the spreading behaviour, while gravitational forces can be neglected [54]. Again, these forces are related by Re , We , and Oh , as shown in Figure 1.9b. These parameters determine the surface energy and contact angle of the liquid droplets on the substrate and can be controlled by varying the

viscosity, surface tension, and density of the ink, as well as the morphology, composition, and temperature of the substrate. Generally, the simplest method to ensure good spreading behaviour, and therefore high resolution of the printing process, is a surface treatment on the substrate prior to printing [55].

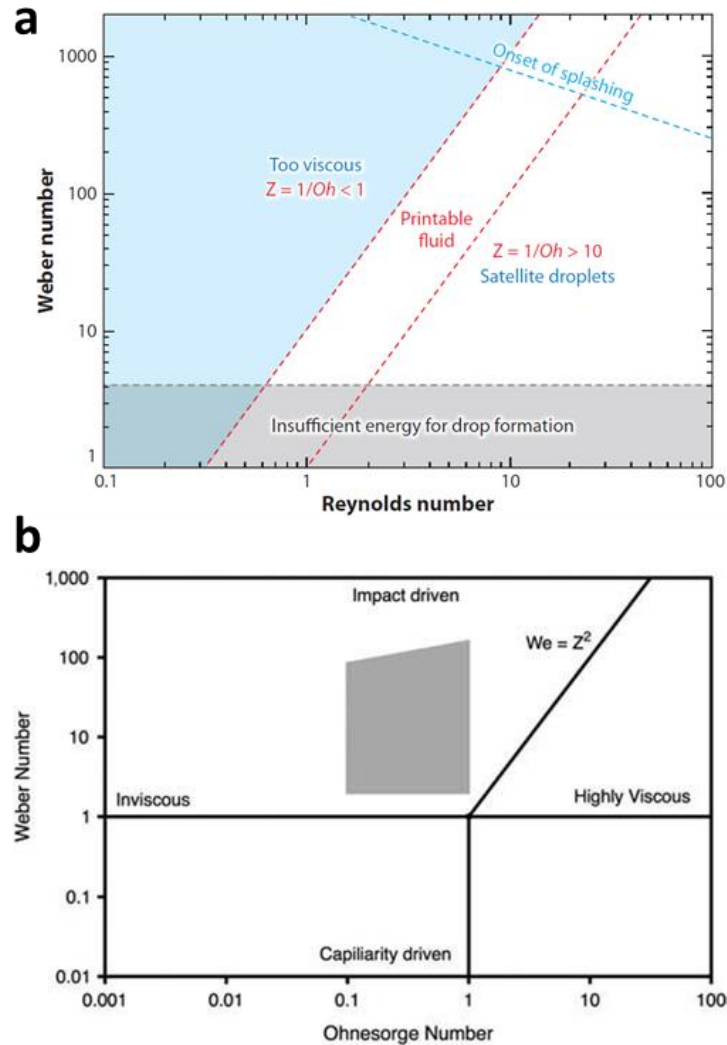


Figure 1.9. Influence of ink properties on (a) droplet formation [57] and (b) droplet spreading [58]. The shaded area in (b) is the region of high quality inkjet printing.

Inkjet solutions for printing functional materials are usually comprised of a nanomaterial dispersed in a solvent, often with a surfactant. As an approximation, the size of the solids in the ink should be less than one-fiftieth the size of the print head nozzles. Typically, inkjet printer nozzles have diameters on the order of tens of microns, so the

nanomaterials should have dimensions less than a few hundred nanometers to prevent clogging of the nozzles [56]. Agglomeration of the solids can also lead to clogging; therefore, the choice of solvent is very important to achieve a uniform dispersion. When the printer is not in use the solvent around the nozzles will evaporate, increasing the local viscosity and disrupting ideal droplet formation. The time for this gelation to occur is referred to as the latency time of the ink and is one of the major challenges of developing inks for inkjet printing [49]. Inkjet printer inks must have relatively low viscosity, compared to other techniques such as screen printing and 3D printing.

During and after spreading, the solvent evaporates and leaves behind a solid film. Solidification is dependent on the solvent used and the temperature of the substrate. During solvent evaporation there is usually a significant decrease in volume, especially when the solid loading concentration is low, as is generally the case when printing nanomaterials. This can be problematic if the ink is not well dispersed, as agglomeration of the solid content may occur, resulting in the formation of disconnected islands. The coffee-ring effect is another commonly encountered problem, in which the concentration of solids becomes higher at the droplet perimeter compared to in the centre upon drying [59]. This can lead to fluctuations in the conductivity within a printed pattern and complications in device operation. A number of techniques have been shown to reduce this coffee-ring effect [60-64]. More detailed explanations of the major stages involved in inkjet printing can be found in references [57] and [58].

1.2.2 Other Printing Technologies

Three additional printing technologies are discussed here: screen printing, transfer printing, and 3D printing. While inkjet printing is the most commonly-used technique for printing nanomaterials, these other technologies have their own unique advantages and are becoming increasingly popular for printing functional materials, especially 3D printing.

Screen printing is a technique using a mesh mask to deposit ink onto a substrate in a given pattern. The ink is placed on top of a thin plastic or metal screen that contains open areas that the ink is forced through with a squeegee (Figure 1.10). Screen printing is commonly used to apply patterns to textiles, wood, and glass. However, researchers have also used it to fabricate electronic devices, such as transistors [65, 66], battery electrodes [39, 67, 68], solar cells [69-72], and fuel cells [73-75].

Screen printing differs from inkjet printing in that it is not an additive process, so there is more wasted material and generally less control of film thickness. However, it can be simpler to make films as the ink can be of a wider range of viscosities and surface tensions, whereas these parameters must be tightly controlled in the inkjet printing process. Usually screen-printed films are much thicker than inkjet-printed films. Similar to inkjet printing, screen printing uses inks composed of solids dispersed in a solvent. However, for screen printing, the inks have a higher viscosity and are less volatile. The solvent usually consists of water or an organic compound that is more stable at room temperature, making the drying process slower than for inkjet printing. Due to the required high viscosity and low volatility, the use of screen printing has been somewhat limited in the field of energy storage and conversion. However, low solid concentration and the coffee-ring effect are not problems when screen printing due to the high pressures used and the fact that the ink is not deposited as droplets. Additionally, screen printing can be adapted to roll-to-roll processing [69], meaning it may soon be a suitable fabrication technique for large-scale production of batteries, supercapacitors, fuel cells, and solar cells.

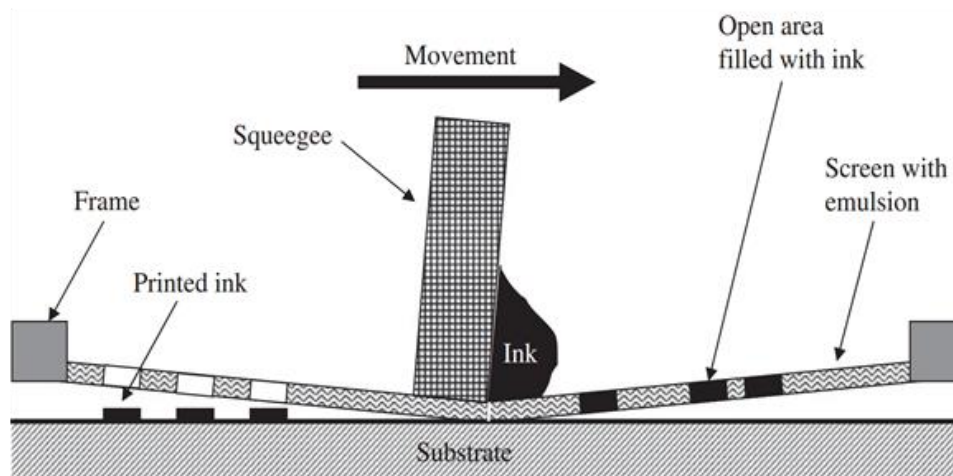


Figure 1.10. Schematic illustration of screen printing [46].

A third printing technique, transfer printing, involves patterning a material onto one substrate initially and then moving it to a second substrate. It has recently become a popular technique for printing a wide variety of materials, including graphene [76], carbon nanotubes [77], quantum dots [78], DNA [79], and metal nanostructures [80]. While inkjet and screen printing are limited to resolutions of approximately 12 μm and 40 μm [57, 81], respectively, transfer printing can be used to pattern features below 100 nm [82, 83].

The transfer printing process is shown schematically in Figure 1.11. First the material to be transferred is synthesized or patterned on its initial substrate. It is then brought into contact with the transfer substrate, generally a flexible elastomeric polymer, and peeled off from the first substrate. Then the transfer substrate with the transfer material is applied to the final substrate. In these last two steps, the temperature and pressure must be tightly controlled in order to get defect-free transfers. Lastly, the transfer substrate is removed and the transfer material remains.

Device fabrication can be performed separately from the assembly stage, which is beneficial for a number of materials and applications, especially graphene and flexible electronics. High quality graphene is usually synthesized by chemical vapour deposition (CVD) at high temperature, which is limited to only a few substrates such as silicon or

copper. However, many applications cannot use graphene in this form and it must therefore be transferred to a second substrate without introducing defects and compromising its quality. This is especially critical for flexible device fabrication, which are assembled on low melting point polymers, usually polyethylene terephthalate (PET). Transfer printing can accomplish this process without exposing the material to any chemicals or solvents that may damage it.

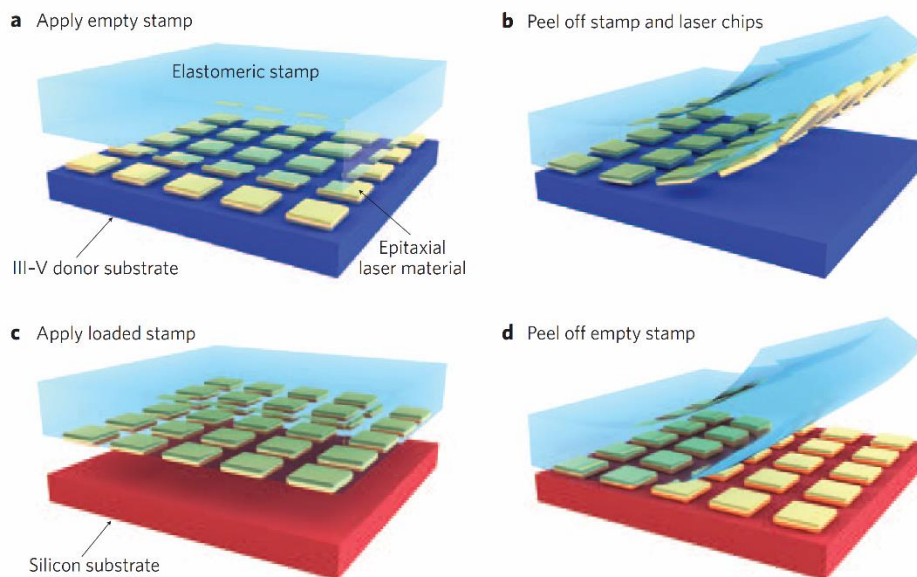


Figure 1.11. Schematic illustration of the transfer printing process [84].

Lastly, 3D printing is a rapidly growing printing technique and is finding applications in an increasing number of fields. Recently it has been used to assemble a 3D battery [85], supercapacitor electrodes [86], tissue engineering scaffolds [87], strain sensors [88], and reduced graphene oxide nanowires [89].

3D printing of functional materials involves extruding material through a nozzle onto a substrate. The pattern is passed over multiple times to build up a three-dimensional structure. Similar to inkjet and screen printing, 3D printing uses an ink comprised of solids dispersed in a solvent that dries upon contact with the substrate. By optimizing the ink's rheological properties, features below 10 μm have been achieved [90]. 3D printing will be especially effective for energy storage and conversion device fabrication. For

example, it is predicted that 3D-printed architectures can double the volumetric energy density of conventional batteries [85].

Table 1.2. Comparison of the four printing techniques discussed in this chapter.

	Inkjet Printing	Screen Printing	Transfer Printing	3D Printing
Minimum Line Width	~12 μm [57]	~40 μm [81]	< 100 nm [82, 83]	~10 μm [90]
Film Thickness	10 nm [91] – 500 μm [46]	400 nm [81] – 500 μm [46]	0.34 nm [92] – 20 μm [93]	> 10 μm [90]
Drying Time	Seconds	Minutes to hours	N/A	Seconds
Printing Speed [46]	Slow to Moderate	Moderate	Moderate to Fast	Slow
Dimensions [46]	2D or quasi-3D	2D	2D	3D
Roll-to-roll compatible [46]	Yes	Yes	Yes	No
Solvent	Low viscosity, high volatility	High viscosity, low volatility	None	Very high viscosity, high volatility

1.3 Battery Electrode Fabrication Methods

1.3.1 Conventional Fabrication Methods

Battery electrode fabrication processes have been developed over the past few decades with an emphasis on increasing throughput and decreasing costs, without compromising the performance of the cells. Different companies may have different production techniques with differing levels of automation, but their general processes will be similar. And although overall battery pack assembly methods will vary between different cell

types (coin, cylindrical, prismatic, pouch), the production of the electrodes is the same. Figure 1.12 shows a typical LIB electrode fabrication process developed by Siemens.

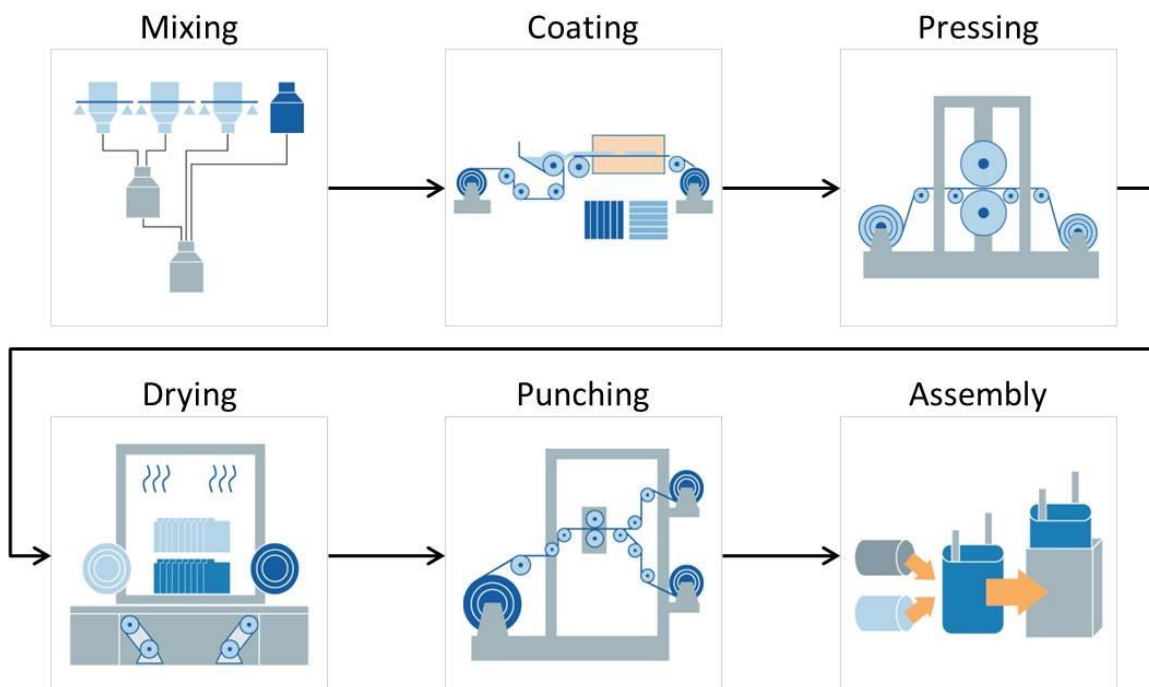


Figure 1.12. Standard electrode fabrication process for LIBs [94].

The first step is to mix the constituent electrode materials together (active material, conductive carbon, and binder) in a non-aqueous solvent, usually N-methyl-2-pyrrolidone (NMP). It is important to achieve a uniform dispersion with no agglomerations or precipitates. Second, this mixture is coated onto the current collector (copper foil for anodes and aluminum foil for cathodes). For thick electrodes, coating is usually performed with a doctor blading or roller coating process to prepare films with uniform thicknesses of hundreds of microns. For thin film electrodes, a number of different techniques are used, which are discussed below. Third, after the solvent has been dried out of the coated films, the electrodes are compressed to reduce porosity and ensure good contact with the current collector. Fourth, the electrodes are dried in a low-humidity chamber to remove any residual water. The fifth stage involves cutting the electrodes into shape with a die punch or other machinery. And finally, the electrodes are stacked, with many cells going into each battery to give the desired voltage and capacity.

The major difference between the fabrication of thick electrodes and thin electrodes is the coating step. This is because the methods used for thick electrodes typically cannot be used to form uniform films thinner than 100 μm . For TFBs, coating the electrode materials on the current collector can be done using sputtering [12, 13], chemical vapor deposition [14, 15], pulsed laser deposition [16, 17], spin coating [18], sol-gel [19, 20], or other methods. All of these techniques can be used to form films with thicknesses below 1 μm . Film thickness can also be finely controlled, meaning the exact desired loading of active material can be achieved. Additionally, by using techniques such as sputtering, chemical vapor deposition, or pulsed laser deposition, one can eliminate the need for polymer binders since the active materials can be strongly bonded to the surface. And if the films are thin enough, conductive carbons are not necessary to carry electrons through the electrode. This eliminates the initial mixing step and removes any chance of inhomogeneity in the electrode [15].

However, these thin film deposition techniques also have their downsides. Sputtering, chemical vapor deposition, and pulsed laser deposition require expensive, complex equipment and high temperatures, which can damage the electrode materials or the underlying substrate. Spin coating and sol-gel methods often require substrate pre-treatments and are not easily scalable. Recently, an alternative fabrication method for LFBs, inkjet printing, has been investigated as a solution to these problems.

1.3.2 Inkjet Printing of Battery Electrodes

Inkjet printing is an alternative technique for fabricating thin film electrodes and provides a few advantages over the other techniques discussed above. First, it is inexpensive, with household inkjet printers costing under \$100 and larger piezoelectric printers designed for functional materials costing in the range of a few thousand dollars. Second, inkjet printing is simple. Once an ink formulation has been developed, printing can be automated. Third, inkjet printing is scalable, with industrial-sized printers or roll-to-roll inkjet printers available. And lastly, it can be used as a more efficient way to deposit patterned electrodes. Instead of cutting the electrodes to size and shape in a punching

step, inkjet printers can deposit droplets only where necessary, eliminating wasted material.

The inkjet printing process for battery electrodes can be divided into two main stages (Figure 1.13). First, ink solutions must be prepared with tightly controlled physical properties to ensure proper jetting. This involves optimizing the ink's viscosity, surface tension, and density to within specifications discussed in section 1.2 above. Inks are typically comprised of nanoparticles of active material, conductive carbon, and a binder dispersed in a volatile solvent. The nanoparticles must be small enough and have minimal agglomeration in the solvent to prevent clogging of the printer's nozzles. Second, after an ink has been prepared it is transferred into a cleaned printer cartridge and inkjet printed onto the current collector. In all studies in which battery electrodes were fabricated by inkjet printing, multiple printing passes were necessary to achieve the desired thickness and uniformity. After printing, the fabrication stages are similar to those discussed for conventional battery electrodes: pressing, drying, punching (if necessary), and assembly.

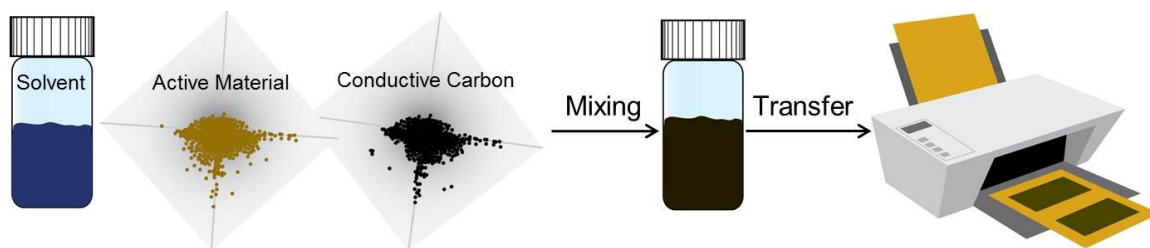


Figure 1.13. Schematic illustration of the inkjet printing process for battery electrodes.

The first instance of inkjet printing used to fabricate battery electrodes was in 2003 when Xu *et al.* printed thin film MnO_2 electrodes for alkaline (Zn/MnO_2) batteries [35]. Following this work, researchers expanded this technique to LIBs, fabricating different anode and cathode materials by inkjet printing. Tin oxide (SnO_2) [36] and lithium titanate ($\text{Li}_4\text{Ti}_5\text{O}_{12}$, LTO) [38] nanoparticles have been printed as anodes, while lithium cobalt oxide (LiCoO_2) [37, 40, 95] and lithium manganese oxide (LiMn_2O_4) [96] have been printed as cathodes.

As a representative example, Zhao *et al.* fabricated thin film LTO electrodes via an inkjet printing process [38]. They synthesized an ink composed of LTO nanoparticles, acetylene black, and carboxymethyl cellulose sodium (CMCS) binder dispersed in a water and alcohol solution. Printing with a standard desktop Canon inkjet printer, they were able to achieve uniform thin films with a thickness of about 1.7-1.8 μm by printing 10 consecutive layers. Figure 1.14 shows both surface and cross-sectional views of the printed thin films on a gold substrate. The LTO particles form a uniform layer with a somewhat porous structure.

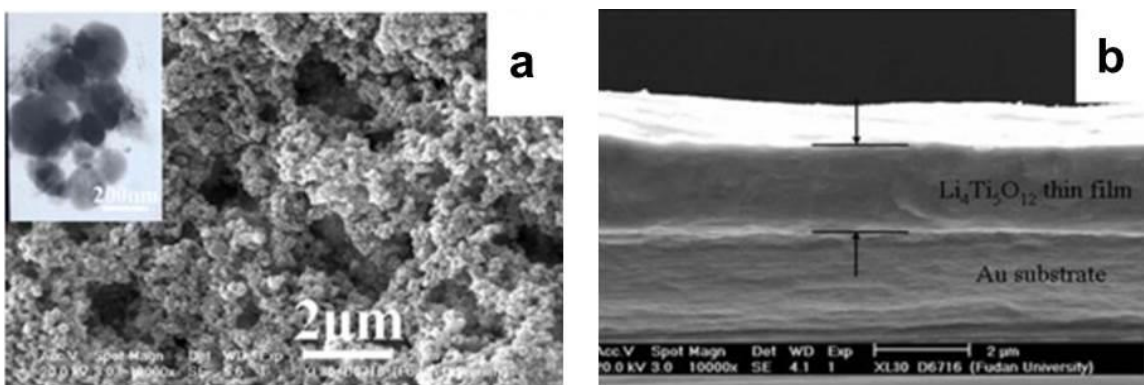


Figure 1.14. SEM images of the (a) surface and (b) cross-section of an inkjet-printed LTO anode (the inset is a TEM image of LTO particles in the film) [38].

Flexible thin film LIBs have also been fabricated by inkjet printing ink onto a flexible substrate. Wei *et al.* printed a flexible solid-state LIB (Figure 1.15) comprised of anatase titanate (TiO_2) nanoparticles mixed with graphene sheets dispersed in water [97]. The graphene was modified with either n-type or p-type anionic groups to help stabilize the graphene dispersions in water, allowing them to be printed without agglomeration and subsequent clogging of the nozzles. The printable electrodes exhibited stable cycling performance comparable to other flexible LIBs [98]. Overall, these studies have demonstrated that inkjet printing is a simple and low-cost fabrication method for thin film LIB electrodes.

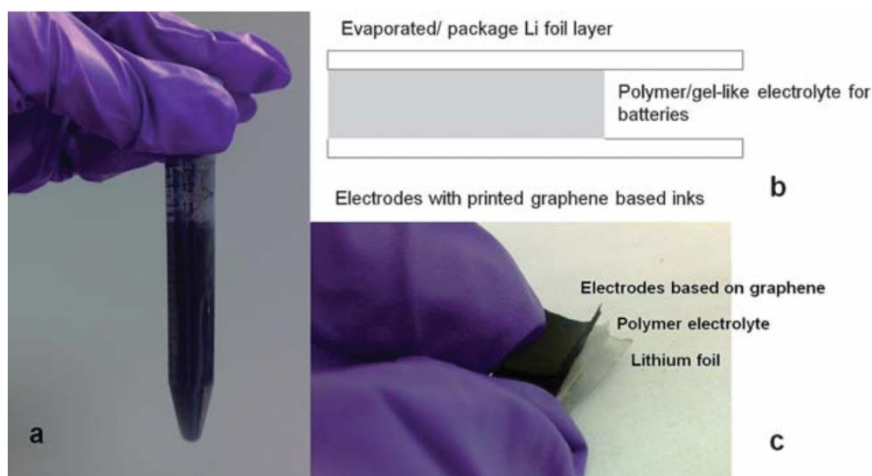


Figure 1.15. (a) Graphene/TiO₂ ink for printing flexible thin film LIB electrodes. (b) Schematic diagram showing the major components of the cell. (c) Demonstrating the flexibility of a printable graphene electrode [97].

1.4 Thesis Objectives

Thin film LIBs are excellent on-board power sources for wireless sensors, implantable medical devices, and flexible electronics. Their small size in the z-dimension allows them to be used in applications where traditional LIBs are too large, or to decrease the thickness of the electronic devices in which they are used. Additionally, higher charging and discharging rates are possible with thin film batteries due to shorter lithium-ion diffusion lengths. However, the methods used to fabricate thin film electrodes are limited by the expensive equipment required, intensive energy needs, and damaging post-annealing treatments.

Therefore, the main objective of this thesis was to develop a simple, cost-effective, and versatile inkjet-printing method for fabricating LIB electrodes. In particular, the goal was to fabricate thin film electrodes comprised of next-generation anode materials by inkjet printing. Specifically, silicon and titanium dioxide were chosen for reasons stated above. Second, the electrochemical performance of these thin film electrodes produced by inkjet printing was investigated. The objectives of this thesis are summarized as follows:

- (1) Develop an inkjet-printing fabrication method for LIB thin film electrodes

- a) Fabricate silicon nanoparticle anodes by inkjet printing
 - b) Fabricate titanium dioxide nanoparticle anodes by inkjet printing
 - c) Explore the effect of printing parameters on film formation and morphology
- (2) Investigate and improve the electrochemical performance of inkjet-printed electrodes
- a) Establish relationships between printing parameters and the electrochemical performance of inkjet-printed thin film electrodes
 - b) Explore the effect of different polymer binders on the specific capacity and cycling performance of inkjet-printed silicon anodes
 - c) Study the rate capability of inkjet-printed titanium dioxide anodes

1.5 Thesis Organization

This thesis consists of five chapters, an introduction, a summary of the experimental methods, two articles, and a concluding chapter, organized in integrated article format. It has been submitted in accordance with the Thesis Regulation Guide of the School of Graduate and Postdoctoral Studies at the University of Western Ontario. In more detail, the following chapters are included:

Chapter 1 gives a general introduction to lithium-ion batteries and printing technologies. It goes into specific details about thin film batteries, the anode materials examined in this work, and inkjet printing, as well as summarizes the conventional battery electrode fabrication techniques and the field of inkjet-printed battery electrodes. Additionally, the objectives of the thesis are stated.

Chapter 2 summarizes the experimental methods used to develop nanomaterial inks and inkjet print them for LIB anodes. It also discusses the various characterization tools used to investigate the morphology, chemical composition, and electrochemical performance of the inkjet-printed films.

Chapter 3 presents the inkjet printing process for fabricating high performance silicon anodes for LIBs. The effects of printing parameters on the film morphology and

electrochemical performance are examined and the electrochemical effects of using different polymer binders are studied in detail.

Chapter 4 reports the use of inkjet printing to fabricate titanium dioxide anodes for LIBs. It details how the thickness of the electrode has a significant effect on its electrochemical performance and also investigates the rate capability of these inkjet-printed anodes.

Chapter 5 summarizes the results presented in chapters 3 and 4 and reflects on the original objectives of the thesis. The prospects of using inkjet printing for commercial fabrication of LIBs are discussed and future work is also suggested.

References

- [1] V. Sapru, "Analysis of the Global Lithium-ion Battery Market: Growth Opportunities and Market Outlook," Frost & Sullivan, San Antonio, Texas, 2014.
- [2] M. M. Thackeray, C. Wolverton, and E. D. Isaacs, "Electrical energy storage for transportation—approaching the limits of, and going beyond, lithium-ion batteries," *Energy & Environmental Science*, vol. 5, pp. 7854-7863, 2012.
- [3] D. Howell, T. Q. Duong, P. W. Faguy, and B. Cunningham, "2013 Energy Storage R&D Progress Report: Advanced Battery Development," U.S. Department of Energy, 2013.
- [4] A. Patil, V. Patil, D. Wook Shin, J.-W. Choi, D.-S. Paik, and S.-J. Yoon, "Issue and challenges facing rechargeable thin film lithium batteries," *Materials Research Bulletin*, vol. 43, pp. 1913-1942, 2008.
- [5] J. F. M. Oudenhoven, L. Baggetto, and P. H. L. Notten, "All-Solid-State Lithium-Ion Microbatteries: A Review of Various Three-Dimensional Concepts," *Advanced Energy Materials*, vol. 1, pp. 10-33, 2011.
- [6] K. Kanehori, K. Matsumoto, K. Miyauchi, and T. Kudo, "Thin film solid electrolyte and its application to secondary lithium cell," *Solid State Ionics*, vol. 9–10, Part 2, pp. 1445-1448, 1983.
- [7] L. Gaines and R. Cuenca, "Costs of Lithium-Ion Batteries for Vehicles," Argonne National Laboratory, Argonne, Illinois, 2000.
- [8] K.-H. Choi, S.-J. Cho, S.-H. Kim, Y. H. Kwon, J. Y. Kim, and S.-Y. Lee, "Thin, Deformable, and Safety-Reinforced Plastic Crystal Polymer Electrolytes for

- High-Performance Flexible Lithium-Ion Batteries," *Advanced Functional Materials*, vol. 24, pp. 44-52, 2014.
- [9] K. Wang, S. Luo, Y. Wu, X. He, F. Zhao, J. Wang, K. Jiang, and S. Fan, "Super-Aligned Carbon Nanotube Films as Current Collectors for Lightweight and Flexible Lithium Ion Batteries," *Advanced Functional Materials*, vol. 23, pp. 846-853, 2013.
- [10] N. Aliahmad, M. Agarwal, S. Shrestha, and K. Varahramyan, "Paper-Based Lithium-Ion Batteries Using Carbon Nanotube-Coated Wood Microfibers," *Nanotechnology, IEEE Transactions on*, vol. 12, pp. 408-412, 2013.
- [11] J. Perelaer, P. J. Smith, D. Mager, D. Soltman, S. K. Volkman, V. Subramanian, J. G. Korvink, and U. S. Schubert, "Printed electronics: the challenges involved in printing devices, interconnects, and contacts based on inorganic materials," *Journal of Materials Chemistry*, vol. 20, pp. 8446-8453, 2010.
- [12] W.-S. Kim, "Characteristics of LiCoO₂ thin film cathodes according to the annealing ambient for the post-annealing process," *Journal of Power Sources*, vol. 134, pp. 103-109, 2004.
- [13] S.-J. Kim, H.-C. Park, M.-C. Kim, D.-M. Kim, Y.-W. Lee, and K.-W. Park, "Sputtered amorphous thin film nanocomposites as an anode for lithium-ion batteries," *Journal of Power Sources*, vol. 273, pp. 707-715, 2015.
- [14] H. Jung, M. Park, S. H. Han, H. Lim, and S.-K. Joo, "Amorphous silicon thin-film negative electrode prepared by low pressure chemical vapor deposition for lithium-ion batteries," *Solid State Communications*, vol. 125, pp. 387-390, 2003.
- [15] A. Jena, N. Munichandraiah, and S. A. Shivashankar, "Metal-organic chemical vapor-deposited cobalt oxide films as negative electrodes for thin film Li-ion battery," *Journal of Power Sources*, vol. 277, pp. 198-204, 2015.
- [16] J. D. Perkins, C. S. Bahn, J. M. McGraw, P. A. Parilla, and D. S. Ginley, "Pulsed Laser Deposition and Characterization of Crystalline Lithium Cobalt Dioxide (LiCoO₂) Thin Films," *Journal of the Electrochemical Society*, vol. 148, pp. A1302-A1312, 2001.
- [17] D. Fujimoto, N. Kuwata, Y. Matsuda, J. Kawamura, and F. Kang, "Fabrication of solid-state thin-film batteries using LiMnPO₄ thin films deposited by pulsed laser deposition," *Thin Solid Films*, vol. 579, pp. 81-88, 2015.
- [18] J. P. Maranchi, A. F. Hepp, and P. N. Kumta, "LiCoO₂ and SnO₂ thin film electrodes for lithium-ion battery applications," *Materials Science and Engineering: B*, vol. 116, pp. 327-340, 2005.

- [19] Y. H. Rho and K. Kanamura, "Preparation of $\text{Li}_{4/3}\text{Ti}_{5/3}\text{O}_4$ Thin Film Electrodes by a PVP Sol-Gel Coating Method and Their Electrochemical Properties," *Journal of the Electrochemical Society*, vol. 151, pp. A106-A110, 2004.
- [20] T. Kwon, T. Ohnishi, K. Mitsuishi, T. C. Ozawa, and K. Takada, "Synthesis of LiCoO_2 epitaxial thin films using a sol-gel method," *Journal of Power Sources*, vol. 274, pp. 417-423, 2015.
- [21] N. A. Kaskhedikar and J. Maier, "Lithium Storage in Carbon Nanostructures," *Advanced Materials*, vol. 21, pp. 2664-2680, 2009.
- [22] Z. Chen, I. Belharouak, Y. K. Sun, and K. Amine, "Titanium-Based Anode Materials for Safe Lithium-Ion Batteries," *Advanced Functional Materials*, vol. 23, pp. 959-969, 2013.
- [23] B. A. Boukamp, G. C. Lesh, and R. A. Huggins, "All-Solid Lithium Electrodes with Mixed-Conductor Matrix," *Journal of The Electrochemical Society*, vol. 128, pp. 725-729, 1981.
- [24] C. K. Chan, H. Peng, G. Liu, K. McIlwrath, X. F. Zhang, R. A. Huggins, and Y. Cui, "High-performance lithium battery anodes using silicon nanowires," *Nat Nano*, vol. 3, pp. 31-35, 2008.
- [25] M.-H. Park, M. G. Kim, J. Joo, K. Kim, J. Kim, S. Ahn, Y. Cui, and J. Cho, "Silicon Nanotube Battery Anodes," *Nano Letters*, vol. 9, pp. 3844-3847, 2009.
- [26] Y. Yao, M. T. McDowell, I. Ryu, H. Wu, N. Liu, L. Hu, W. D. Nix, and Y. Cui, "Interconnected Silicon Hollow Nanospheres for Lithium-Ion Battery Anodes with Long Cycle Life," *Nano Letters*, vol. 11, pp. 2949-2954, 2011.
- [27] H. Kim and J. Cho, "Superior Lithium Electroactive Mesoporous Si@Carbon Core-Shell Nanowires for Lithium Battery Anode Material," *Nano Letters*, vol. 8, pp. 3688-3691, 2008.
- [28] P. Gao, J. Fu, J. Yang, R. Lv, J. Wang, Y. Nuli, and X. Tang, "Microporous carbon coated silicon core/shell nanocomposite via in situ polymerization for advanced Li-ion battery anode material," *Physical Chemistry Chemical Physics*, vol. 11, pp. 11101-11105, 2009.
- [29] R. A. Huggins and W. D. Nix, "Decrepitation model for capacity loss during cycling of alloys in rechargeable electrochemical systems," *Ionics*, vol. 6, pp. 57-63, 2000.
- [30] J. R. Szczech and S. Jin, "Nanostructured silicon for high capacity lithium battery anodes," *Energy & Environmental Science*, vol. 4, pp. 56-72, 2011.

- [31] M. Wagemaker, A. P. M. Kentgens, and F. M. Mulder, "Equilibrium lithium transport between nanocrystalline phases in intercalated TiO₂ anatase," *Nature*, vol. 418, pp. 397-399, 2002.
- [32] R. van de Krol, A. Goossens, and J. Schoonman, "Spatial Extent of Lithium Intercalation in Anatase TiO₂," *The Journal of Physical Chemistry B*, vol. 103, pp. 7151-7159, 1999.
- [33] Z. Yang, D. Choi, S. Kerisit, K. M. Rosso, D. Wang, J. Zhang, G. Graff, and J. Liu, "Nanostructures and lithium electrochemical reactivity of lithium titanates and titanium oxides: A review," *Journal of Power Sources*, vol. 192, pp. 588-598, 2009.
- [34] A. G. Dylla, G. Henkelman, and K. J. Stevenson, "Lithium Insertion in Nanostructured TiO₂(B) Architectures," *Accounts of Chemical Research*, vol. 46, pp. 1104-1112, 2013.
- [35] F. Xu, T. Wang, W. Li, and Z. Jiang, "Preparing ultra-thin nano-MnO₂ electrodes using computer jet-printing method," *Chemical Physics Letters*, vol. 375, pp. 247-251, 2003.
- [36] Y. Zhao, Q. Zhou, L. Liu, J. Xu, M. Yan, and Z. Jiang, "A novel and facile route of ink-jet printing to thin film SnO₂ anode for rechargeable lithium ion batteries," *Electrochimica Acta*, vol. 51, pp. 2639-2645, 2006.
- [37] J. Huang, J. Yang, W. Li, W. Cai, and Z. Jiang, "Electrochemical properties of LiCoO₂ thin film electrode prepared by ink-jet printing technique," *Thin Solid Films*, vol. 516, pp. 3314-3319, 2008.
- [38] Y. Zhao, G. Liu, L. Liu, and Z. Jiang, "High-performance thin-film Li₄Ti₅O₁₂ electrodes fabricated by using ink-jet printing technique and their electrochemical properties," *Journal of Solid State Electrochemistry*, vol. 13, pp. 705-711, 2008.
- [39] M. Hilder, B. Winther-Jensen, and N. B. Clark, "Paper-based, printed zinc-air battery," *Journal of Power Sources*, vol. 194, pp. 1135-1141, 2009.
- [40] J.-H. Lee, S.-B. Wee, M.-S. Kwon, H.-H. Kim, J.-M. Choi, M. S. Song, H. B. Park, H. Kim, and U. Paik, "Strategic dispersion of carbon black and its application to ink-jet-printed lithium cobalt oxide electrodes for lithium ion batteries," *Journal of Power Sources*, vol. 196, pp. 6449-6455, 2011.
- [41] C. Zhao, C. Wang, R. Gorkin, S. Beirne, K. Shu, and G. G. Wallace, "Three dimensional (3D) printed electrodes for interdigitated supercapacitors," *Electrochemistry Communications*, vol. 41, pp. 20-23, 2014.
- [42] M. R. Arcila-Velez, J. Zhu, A. Childress, M. Karakaya, R. Podila, A. M. Rao, and M. E. Roberts, "Roll-to-roll synthesis of vertically aligned carbon nanotube

- electrodes for electrical double layer capacitors," *Nano Energy*, vol. 8, pp. 9-16, 2014.
- [43] P. Chen, H. Chen, J. Qiu, and C. Zhou, "Inkjet printing of single-walled carbon nanotube/RuO₂ nanowire supercapacitors on cloth fabrics and flexible substrates," *Nano Research*, vol. 3, pp. 594-603, 2010.
- [44] D. Pech, M. Brunet, P.-L. Taberna, P. Simon, N. Fabre, F. Mesnilgrete, V. Conédéra, and H. Durou, "Elaboration of a microstructured inkjet-printed carbon electrochemical capacitor," *Journal of Power Sources*, vol. 195, pp. 1266-1269, 2010.
- [45] M. Kaempgen, C. K. Chan, J. Ma, Y. Cui, and G. Gruner, "Printable Thin Film Supercapacitors Using Single-Walled Carbon Nanotubes," *Nano Letters*, vol. 9, pp. 1872-1876, 2009.
- [46] F. C. Krebs, "Fabrication and processing of polymer solar cells: A review of printing and coating techniques," *Solar Energy Materials and Solar Cells*, vol. 93, pp. 394-412, 2009.
- [47] C. N. Hoth, S. A. Choulis, P. Schilinsky, and C. J. Brabec, "High Photovoltaic Performance of Inkjet Printed Polymer:Fullerene Blends," *Advanced Materials*, vol. 19, pp. 3973-3978, 2007.
- [48] H. S. Kim, J. S. Kang, J. S. Park, H. T. Hahn, H. C. Jung, and J. W. Joung, "Inkjet printed electronics for multifunctional composite structure," *Composites Science and Technology*, vol. 69, pp. 1256-1264, 2009.
- [49] C. N. Hoth, P. Schilinsky, S. A. Choulis, and C. J. Brabec, "Printing Highly Efficient Organic Solar Cells," *Nano Letters*, vol. 8, pp. 2806-2813, 2008.
- [50] K. X. Steirer, J. J. Berry, M. O. Reese, M. F. A. M. van Hest, A. Miedaner, M. W. Liberatore, R. T. Collins, and D. S. Ginley, "Ultrasonically sprayed and inkjet printed thin film electrodes for organic solar cells," *Thin Solid Films*, vol. 517, pp. 2781-2786, 2009.
- [51] J. Aden, J. Bohórquez, D. Collins, M. Crook, A. García, and U. Hess, "The Third-Generation HP Thermal InkJet Printhead," *Hewlett-Packard Journal*, pp. 41-45, 1994.
- [52] J. Li, F. Ye, S. Vaziri, M. Muhammed, M. C. Lemme, and M. Östling, "Efficient Inkjet Printing of Graphene," *Advanced Materials*, vol. 25, pp. 3985-3992, 2013.
- [53] X. Wang, W. W. Carr, D. G. Bucknall, and J. F. Morris, "High-shear-rate capillary viscometer for inkjet inks," *Review of Scientific Instruments*, vol. 81, p. 065106, 2010.

- [54] J. Stringer and B. Derby, "Limits to feature size and resolution in ink jet printing," *Journal of the European Ceramic Society*, vol. 29, pp. 913-918, 2009.
- [55] J. A. Lim, J. H. Cho, Y. Jang, J. T. Han, and K. Cho, "Precise control of surface wettability of mixed monolayers using a simple wiping method," *Thin Solid Films*, vol. 515, pp. 2079-2084, 2006.
- [56] Y. Su, J. Du, D. Sun, C. Liu, and H. Cheng, "Reduced graphene oxide with a highly restored π -conjugated structure for inkjet printing and its use in all-carbon transistors," *Nano Research*, vol. 6, pp. 842-852, 2013.
- [57] B. Derby, "Inkjet Printing of Functional and Structural Materials: Fluid Property Requirements, Feature Stability, and Resolution," *Annual Review of Materials Research*, vol. 40, pp. 395-414, 2010.
- [58] G. Cummins and M. P. Y. Desmulliez, "Inkjet printing of conductive materials: a review," *Circuit World*, vol. 38, pp. 193-213, 2012.
- [59] R. D. Deegan, O. Bakajin, T. F. Dupont, G. Huber, S. R. Nagel, and T. A. Witten, "Capillary flow as the cause of ring stains from dried liquid drops," *Nature*, vol. 389, pp. 827-829, 1997.
- [60] D. Soltman and V. Subramanian, "Inkjet-Printed Line Morphologies and Temperature Control of the Coffee Ring Effect," *Langmuir*, vol. 24, pp. 2224-2231, 2008.
- [61] R. D. Deegan, O. Bakajin, T. F. Dupont, G. Huber, S. R. Nagel, and T. A. Witten, "Contact line deposits in an evaporating drop," *Physical Review E: Statistical Physics, Plasmas, Fluids, and Related Interdisciplinary Topics*, vol. 62, pp. 756-765, 2000.
- [62] D. Kim, S. Jeong, B. K. Park, and J. Moon, "Direct writing of silver conductive patterns: Improvement of film morphology and conductance by controlling solvent compositions," *Applied Physics Letters*, vol. 89, p. 264101, 2006.
- [63] J. Park and J. Moon, "Control of Colloidal Particle Deposit Patterns within Picoliter Droplets Ejected by Ink-Jet Printing," *Langmuir*, vol. 22, pp. 3506-3513, 2006.
- [64] B.-J. de Gans and U. S. Schubert, "Inkjet Printing of Well-Defined Polymer Dots and Arrays," *Langmuir*, vol. 20, pp. 7789-7793, 2004.
- [65] Z. Bao, Y. Feng, A. Dodabalapur, V. R. Raju, and A. J. Lovinger, "High-Performance Plastic Transistors Fabricated by Printing Techniques," *Chemistry of Materials*, vol. 9, pp. 1299-1301, 1997.

- [66] J. A. Rogers, Z. Bao, and V. R. Raju, "Nonphotolithographic fabrication of organic transistors with micron feature sizes," *Applied Physics Letters*, vol. 72, pp. 2716-2718, 1998.
- [67] M.-S. Park, S.-H. Hyun, and S.-C. Nam, "Mechanical and electrical properties of a LiCoO₂ cathode prepared by screen-printing for a lithium-ion micro-battery," *Electrochimica Acta*, vol. 52, pp. 7895-7902, 2007.
- [68] S. Ohta, S. Komagata, J. Seki, T. Saeki, S. Morishita, and T. Asaoka, "All-solid-state lithium ion battery using garnet-type oxide and Li₃BO₃ solid electrolytes fabricated by screen-printing," *Journal of Power Sources*, vol. 238, pp. 53-56, 2013.
- [69] F. C. Krebs, M. Jørgensen, K. Norrman, O. Hagemann, J. Alstrup, T. D. Nielsen, J. Fyenbo, K. Larsen, and J. Kristensen, "A complete process for production of flexible large area polymer solar cells entirely using screen printing—First public demonstration," *Solar Energy Materials and Solar Cells*, vol. 93, pp. 422-441, 2009.
- [70] F. C. Krebs, "Polymer solar cell modules prepared using roll-to-roll methods: Knife-over-edge coating, slot-die coating and screen printing," *Solar Energy Materials and Solar Cells*, vol. 93, pp. 465-475, 2009.
- [71] S. Ito, P. Chen, P. Comte, M. K. Nazeeruddin, P. Liska, P. Péchy, and M. Grätzel, "Fabrication of screen-printing pastes from TiO₂ powders for dye-sensitised solar cells," *Progress in Photovoltaics: Research and Applications*, vol. 15, pp. 603-612, 2007.
- [72] S. E. Shaheen, R. Radspinner, N. Peyghambarian, and G. E. Jabbour, "Fabrication of bulk heterojunction plastic solar cells by screen printing," *Applied Physics Letters*, vol. 79, pp. 2996-2998, 2001.
- [73] M. R. Somalu, V. Yufit, I. P. Shapiro, P. Xiao, and N. P. Brandon, "The impact of ink rheology on the properties of screen-printed solid oxide fuel cell anodes," *International Journal of Hydrogen Energy*, vol. 38, pp. 6789-6801, 2013.
- [74] P. Von Dollen and S. Barnett, "A Study of Screen Printed Yttria-Stabilized Zirconia Layers for Solid Oxide Fuel Cells," *Journal of the American Ceramic Society*, vol. 88, pp. 3361-3368, 2005.
- [75] M. R. Somalu and N. P. Brandon, "Rheological Studies of Nickel/Scandia-Stabilized-Zirconia Screen Printing Inks for Solid Oxide Fuel Cell Anode Fabrication," *Journal of the American Ceramic Society*, vol. 95, pp. 1220-1228, 2012.
- [76] J. H. Chen, M. Ishigami, C. Jang, D. R. Hines, M. S. Fuhrer, and E. D. Williams, "Printed Graphene Circuits," *Advanced Materials*, vol. 19, pp. 3623-3627, 2007.

- [77] D. R. Hines, S. Mezheny, M. Breban, E. D. Williams, V. W. Ballarotto, G. Esen, A. Southard, and M. S. Fuhrer, "Nanotransfer printing of organic and carbon nanotube thin-film transistors on plastic substrates," *Applied Physics Letters*, vol. 86, p. 163101, 2005.
- [78] T.-H. Kim, K.-S. Cho, E. K. Lee, S. J. Lee, J. Chae, J. W. Kim, D. H. Kim, J.-Y. Kwon, G. Amaratunga, S. Y. Lee, B. L. Choi, Y. Kuk, J. M. Kim, and K. Kim, "Full-colour quantum dot displays fabricated by transfer printing," *Nature Photonics*, vol. 5, pp. 176-182, 2011.
- [79] A. Cerf, T. Alava, R. A. Barton, and H. G. Craighead, "Transfer-Printing of Single DNA Molecule Arrays on Graphene for High-Resolution Electron Imaging and Analysis," *Nano Letters*, vol. 11, pp. 4232-4238, 2011.
- [80] H. Mizuno, T. Kaneko, I. Sakata, and K. Matsubara, "Capturing by self-assembled block copolymer thin films: transfer printing of metal nanostructures on textured surfaces," *Chemical Communications*, vol. 50, pp. 362-364, 2014.
- [81] W. J. Hyun, E. B. Secor, M. C. Hersam, C. D. Frisbie, and L. F. Francis, "High-Resolution Patterning of Graphene by Screen Printing with a Silicon Stencil for Highly Flexible Printed Electronics," *Advanced Materials*, vol. 27, pp. 109-115, 2015.
- [82] Y.-L. Loo, J. W. P. Hsu, R. L. Willett, K. W. Baldwin, K. W. West, and J. A. Rogers, "High-resolution transfer printing on GaAs surfaces using alkane dithiol monolayers," *Journal of Vacuum Science & Technology B*, vol. 20, pp. 2853-2856, 2002.
- [83] J. W. Jeong, S. R. Yang, Y. H. Hur, S. W. Kim, K. M. Baek, S. Yim, H.-I. Jang, J. H. Park, S. Y. Lee, C.-O. Park, and Y. S. Jung, "High-resolution nanotransfer printing applicable to diverse surfaces via interface-targeted adhesion switching," *Nature Communications*, vol. 5, 2014.
- [84] R. W. Kelsall, "Hybrid silicon lasers: Rubber stamp for silicon photonics," *Nature Photonics*, vol. 6, pp. 577-579, 2012.
- [85] K. Sun, T. S. Wei, B. Y. Ahn, J. Y. Seo, S. J. Dillon, and J. A. Lewis, "3D printing of interdigitated Li-ion microbattery architectures," *Advanced Materials*, vol. 25, pp. 4539-43, Sep 6 2013.
- [86] C. Zhao, C. Wang, R. Gorkin Iii, S. Beirne, K. Shu, and G. G. Wallace, "Three dimensional (3D) printed electrodes for interdigitated supercapacitors," *Electrochemistry Communications*, vol. 41, pp. 20-23, 2014.
- [87] S. Bose, S. Vahabzadeh, and A. Bandyopadhyay, "Bone tissue engineering using 3D printing," *Materials Today*, vol. 16, pp. 496-504, 2013.

- [88] J. T. Muth, D. M. Vogt, R. L. Truby, Y. Mengüç, D. B. Kolesky, R. J. Wood, and J. A. Lewis, "Embedded 3D Printing of Strain Sensors within Highly Stretchable Elastomers," *Advanced Materials*, vol. 26, pp. 6307-6312, 2014.
- [89] J. H. Kim, W. S. Chang, D. Kim, J. R. Yang, J. T. Han, G.-W. Lee, J. T. Kim, and S. K. Seol, "3D Printing of Reduced Graphene Oxide Nanowires," *Advanced Materials*, vol. 27, pp. 157-161, 2015.
- [90] Y. Han, C. Wei, and J. Dong, "Super-resolution electrohydrodynamic (EHD) 3D printing of micro-structures using phase-change inks," *Manufacturing Letters*, vol. 2, pp. 96-99, 2014.
- [91] D. M. Goldie, A. C. Hourd, M. R. Harvie, J. Thomson, and A. Abdolvand, "Scatter-limited conduction in printed platinum nanofilms," *Journal of Materials Science*, vol. 50, pp. 1169-1174, 2015.
- [92] S. Bae, H. Kim, Y. Lee, X. Xu, J.-S. Park, Y. Zheng, J. Balakrishnan, T. Lei, H. Ri Kim, Y. I. Song, Y.-J. Kim, K. S. Kim, B. Ozyilmaz, J.-H. Ahn, B. H. Hong, and S. Iijima, "Roll-to-roll production of 30-inch graphene films for transparent electrodes," *Nature Nanotechnology*, vol. 5, pp. 574-578, 2010.
- [93] T.-i. Kim, M. J. Kim, Y. H. Jung, H. Jang, C. Dagdeviren, H. A. Pao, S. J. Cho, A. Carlson, K. J. Yu, A. Ameen, H.-j. Chung, S. H. Jin, Z. Ma, and J. A. Rogers, "Thin Film Receiver Materials for Deterministic Assembly by Transfer Printing," *Chemistry of Materials*, vol. 26, pp. 3502-3507, 2014.
- [94] Siemens. (2015, August 27). *Battery Manufacturing Process*. Available: <http://www.industry.siemens.com/topics/global/en/battery-manufacturing/process/Pages/default.aspx>
- [95] Y. M. Zhao, J. Xu, L. Liu, J. Yang, and Z. Y. Jiang, "Thin Film LiCoO₂ Cathode Prepared by Using Ink-jet Printing Technique and Its Electrochemical Properties," *Chemical Journal of Chinese Universities*, vol. 28, pp. 1122-1125, 2007.
- [96] J. J. Huang and Z. Y. Jiang, "Electrochemical Performance of LiMn₂O₄ Thin Film Electrode Fabricated by Ink-Jet Printing Technique," *Acta Physico-Chimica Sinica*, vol. 24, pp. 1563-1567, 2008.
- [97] D. Wei, P. Andrew, H. Yang, Y. Jiang, F. Li, C. Shan, W. Ruan, D. Han, L. Niu, C. Bower, T. Ryhänen, M. Rouvala, G. A. J. Amaratunga, and A. Ivaska, "Flexible solid state lithium batteries based on graphene inks," *Journal of Materials Chemistry*, vol. 21, p. 9762, 2011.
- [98] Y. Hu and X. Sun, "Flexible rechargeable lithium ion batteries: advances and challenges in materials and process technologies," *Journal of Materials Chemistry A*, vol. 2, pp. 10712-10738, 2014.

Chapter 2

2 Experimental and Characterization Methods

This chapter gives an overview of the methods used to inkjet print thin film electrodes for LIBs and the techniques used to characterize them. It is meant as a brief summary of the equipment used during the thesis work. More details about the specific processes and characterization tools used in each study can be found in the methods sections of their respective chapters.

2.1 Inkjet printing of nanomaterials

2.1.1 Ink preparation

Ink solutions were comprised of three components: (1) an electroactive material, (2) a conductive agent, and (3) a polymer binder, all dispersed in water. In this thesis, commercial silicon nanoparticles (50 nm diameter) and titanium dioxide nanoparticles (21 nm diameter) were used as the electrochemically active components. Carbon black (50 nm primary particles) was used as the conductive filler. And four different polymer binders were investigated for their effects on stabilizing the cycling performance of the printed electrodes: poly(3,4-ethylenedioxythiophene)-poly(styrene sulfonate) (PEDOT:PSS), polyvinylpyrrolidone (PVP), carboxymethyl cellulose (CMC), and Na-alginate.

The ratio of these three components was varied to optimize the jetting properties of the ink, as well as the electrochemical performance of the printed films. For silicon, a ratio of 2:2:1 active material : carbon black : binder was used, while for titanium dioxide a ratio of 8:1:1 was determined to be ideal. The solid materials were dispersed in DI-water and the solutions were sonicated in a bath sonicator (Branson) for at least 3 hours prior to use to break up particle agglomerations and to ensure the ink was uniformly mixed.

The viscosity of the ink was determined with a U-tube viscometer (Cannon Instrument Company), shown in Figure 2.1. By measuring the time it takes for the solution to pass between points A and B, the kinematic viscosity, in cSt ($= 1 \text{ mm}^2/\text{s}$), can be calculated by multiplying by the viscometer constant, in cSt/s, given by the manufacturer. The dynamic viscosity, in mPa·s, is related to the kinematic viscosity by equation 2.1:

$$v = \frac{\eta}{\rho} \quad (2.1)$$

where v is the kinematic viscosity, η is the dynamic viscosity, and ρ is the density. The concentration of the ink was varied until a dynamic viscosity of 10 mPa·s was achieved, which is a standard value for inkjet printing [1]. This typically corresponded to a concentration of around 20 mg/mL.

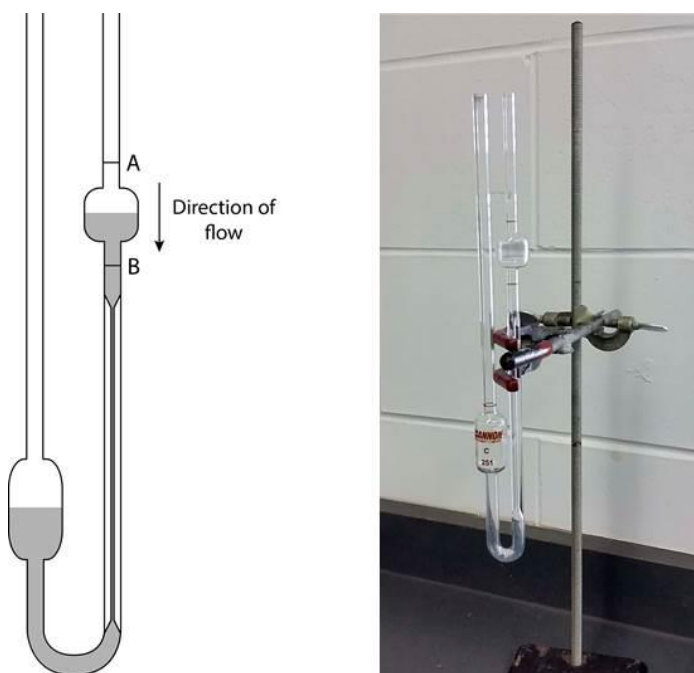


Figure 2.1. A schematic illustration (left) and photo (right) of the U-tube viscometer used to measure ink viscosity.

2.1.2 Inkjet printing

The prepared ink solutions were injected into thoroughly-cleaned ink cartridges, as shown in Figure 2.2. The cartridges were cleaned by first printing out the original black ink until a “low cartridge” warning was given and then injecting DI-water until the liquid passing out was clear, indicating that no black ink remained. The ink was then printed onto copper foil, which acted as the current collector, with the Hewlett-Packard (HP) Deskjet 2540 inkjet printer shown in Figure 2.2. Multiple layers were printed on top of one another until a sufficiently thick and uniform film was formed. After each layer was printed, the films were dried using a compressed air gun. The ideal number of layers was determined to be 25, as discussed in Chapters 3 and 4. After all layers were printed, the films were dried in a vacuum oven at 60°C overnight.

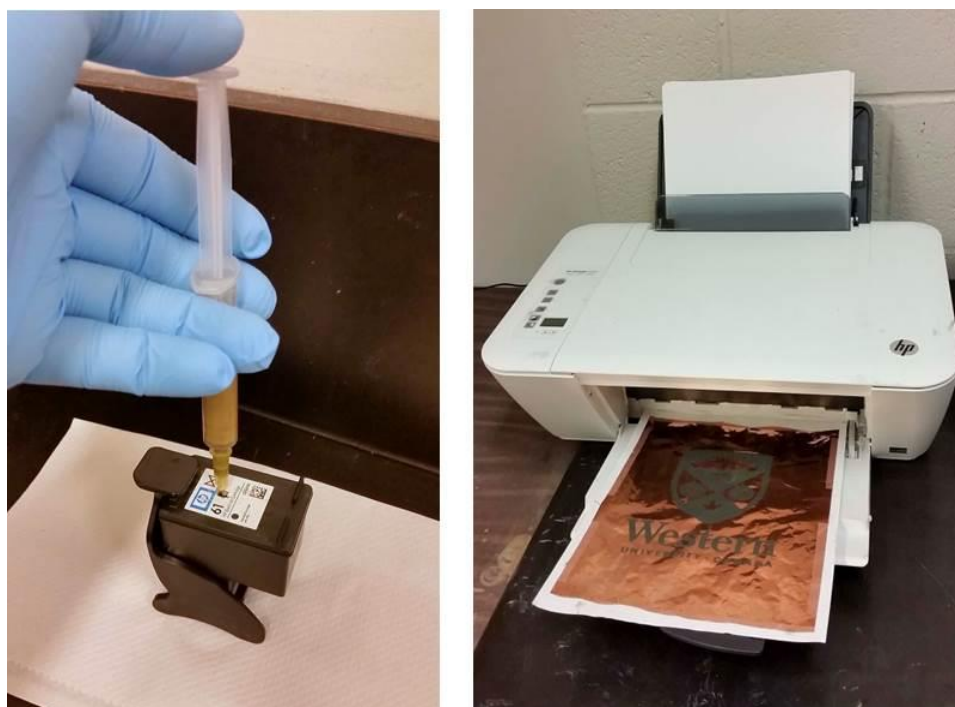


Figure 2.2. Injecting a silicon ink solution into an HP 61 ink cartridge (left) and the HP Deskjet 2540 inkjet printer used to print LIB anodes (right).

2.2 Characterization methods

2.2.1 Physical and compositional characterization

A multitude of techniques were used to examine the physical and chemical properties of the inkjet-printed films, including scanning electron microscopy (SEM), electron dispersive X-ray (EDX) spectroscopy, X-ray diffraction (XRD), Fourier transform infrared (FTIR) spectroscopy, Raman spectroscopy, and thermogravimetric analysis (TGA). All characterization techniques could be used both before and after electrochemical cycling, to observe changes in the electrodes' morphologies and chemical structures. To perform post-cycling tests, cells were disassembled in the glovebox and the electrodes were washed with DMC to remove any residual electrolyte. The samples were kept under argon atmosphere until characterization was performed.

A Hitachi S-4800 field emission SEM (Figure 2.3) was used to characterize the surface morphology of the inkjet-printed electrodes. The resolution of the secondary electron mode is 2 nm at an accelerating voltage of 1 kV. The attached EDX spectrometer was used to measure the elemental composition of the films, giving the atomic percentage of elements present.

A Bruker D8 Advance XRD instrument (Figure 2.4) was used to determine the crystal structure and composition of the printed electrodes. To analyze the thin films, it was necessary to operate at grazing incidence angles in order to minimize the contribution from the copper substrate. When characterizing electrodes after cycling, an airtight chamber with a beryllium window filled with argon was used to hold the sample.

A Nicolet 6700 FTIR spectrometer (Figure 2.5) was used to gather chemical information about the printed electrodes, especially concerning the different functional groups present during charging and discharging. It was a very simple, yet powerful, technique to observe how the polymer binder's chemical interactions with its environment changed during cycling.



Figure 2.3. A photo of the Hitachi S-4800 field emission SEM equipped with and EDX spectrometer.



Figure 2.4. A photo of the Bruker D8 Advance XRD instrument.



Figure 2.5. A photo of the Nicolet 6700 FTIR spectrometer.

As a complementary tool to FTIR spectroscopy, a HORIBA Scientific LabRAM HR Raman spectrometer with a 532.4 nm (green) laser (Figure 2.6) was also used to analyze the chemical structure of the electrodes during cycling.

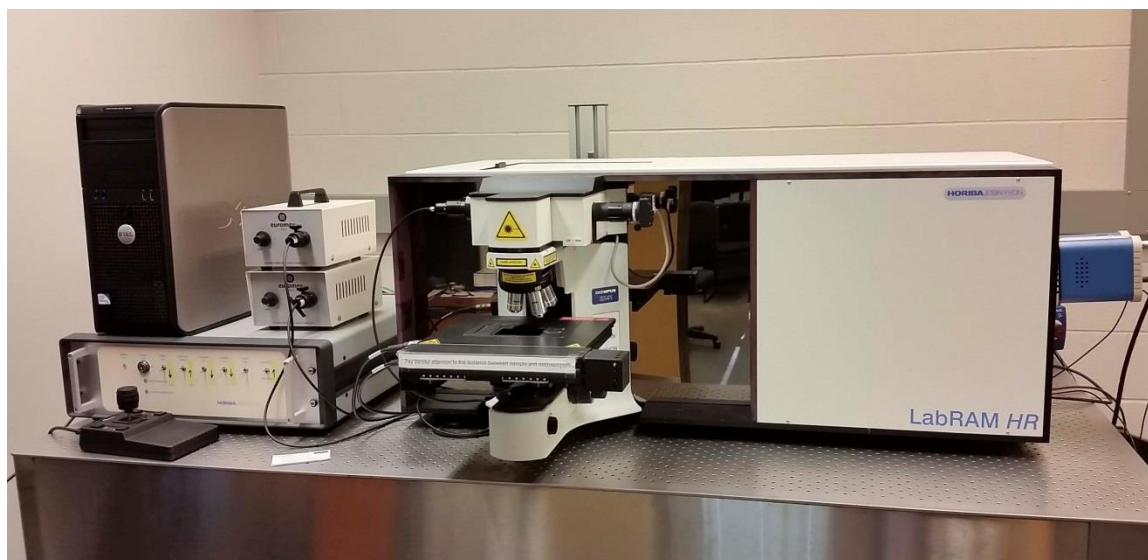


Figure 2.6. A photo of the HORIBA Scientific LabRAM HR Raman spectrometer.

To gather compositional data, as well as thermal stability information, a TA Instruments SDT Q600 TGA was used. By burning off all components of the electrodes except for the

active material, it was possible to determine the loading percentage of electroactive material in the printed films. This value typically differed from the loading percentage in the ink solutions, due to particles becoming trapped in the cartridge's sponge or nozzles. The loading percentage in the printed films measured with TGA was used to calculate the current densities and capacities for electrochemical characterization.



Figure 2.7. A photo of the TA Instruments SDT Q600 TGA.

2.2.2 Electrochemical characterization

In order to test the electrochemical performance of the inkjet-printed electrodes, they were first assembled into CR-2032 coin cells in an argon-filled glovebox (oxygen and moisture concentrations below 1 ppm). The printed films were cut into circular disks with a diameter of 9/16 inches (14.29 mm) and used as the working electrode, while lithium metal was used as the counter and reference electrode. Unless otherwise stated, the electrolyte consisted of LiPF_6 salt dissolved in a solution of ethyl carbonate (EC), diethyl carbonate, (DEC), and ethyl methyl carbonate (EMC), 1:1:1 by volume. In some cases when measuring the performance of inkjet-printed silicon anodes, the electrolyte was

composed of LiPF_6 salt dissolved in a solution of fluoroethylene carbonate (FEC) and dimethyl carbonate (DMC), 1:9 by weight. The assembled coin cells were stored overnight before testing, to ensure sufficient wetting of the polypropylene separator (Celgard 2400).

These half-cells were then studied with galvanostatic cycling, cyclic voltammetry (CV), and electrochemical impedance spectroscopy (EIS). Galvanostatic cycling was performed on an Arbin BT-2000 battery test station, shown in Figure 2.8. This technique involves charging and discharging the cell by maintaining a constant current and measuring its capacity (amount of charge stored or released) and voltage. By repeating charge and discharge steps many times, one can gather information about the cycling performance of the cell (i.e how the capacity fades over the cell's lifetime). It is standard to report the applied current in terms of a C-rate to normalize it to the electrode's theoretical capacity. A rate of 1C corresponds to a full discharge or full charge in one hour, whereas a rate of 0.1C corresponds to a full discharge or full charge in ten hours. A higher C-rate results in a lower capacity. In this thesis, all capacity values are given with the corresponding C-rate used to cycle the cell.

The theoretical capacity, q , of an electrode material can be calculated using equation 2.2:

$$q = \frac{nF}{M} \quad (2.2)$$

where n is the number of electrons involved in the electrochemical reaction, F is Faraday's constant, and M is its molecular weight. The active materials used in this thesis, silicon and titanium dioxide, have theoretical capacities of 4200 mAh g^{-1} and 335 mAh g^{-1} , respectively.

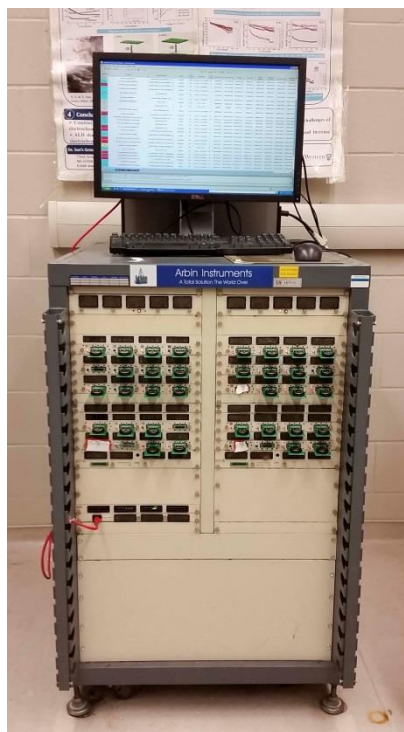


Figure 2.8. A photo of the Arbin BT-2000 battery test station.

CV and EIS measurements were taken with a multichannel potentiostat 3/Z (VMP3), shown in Figure 2.9. CV measures the current through the cell at an applied voltage. The voltage is swept at a constant rate with respect to time until a set potential is reached, at which point the scan is reversed. CV was used to study the reduction and oxidation processes of electrochemical species, giving information about the location of redox potentials and about the reversibility of a reaction. By repeating multiple scans, the formation and stabilization of the solid-electrolyte interface (SEI) was observed. Additionally, varying the scan rate and measuring the change in current was used to calculate the diffusion rate of lithium through the electrode, as discussed in Chapter 4. In general, a faster scan rate gives results in a higher absolute current at a given potential.



Figure 2.9. A photo of the VMP3 multichannel potentiostat 3/Z for CV and EIS measurements.

EIS was used to measure the internal resistance of the half-cells. Of interest were the charge transfer resistance and Warburg impedance, which give information about the kinetics at the electrode-electrolyte interface and lithium-ion diffusion into the electrode, respectively. Additionally, evidence for the mechanism of capacity fade was collected by measuring the impedance after galvanostatic cycling.

References

- [1] J. Li, F. Ye, S. Vaziri, M. Muhammed, M. C. Lemme, and M. Östling, "Efficient Inkjet Printing of Graphene," *Advanced Materials*, vol. 25, pp. 3985-3992, 2013.

Chapter 3

3 High performance inkjet-printed silicon anodes for lithium-ion batteries

*This chapter is to be submitted for peer-reviewed publication.

Thin film batteries have attracted increasing attention recently as the miniaturization of wireless electronics demands ever-smaller energy storage devices. Here we report the fabrication of thin film silicon nanoparticle anodes for lithium-ion batteries by inkjet printing, which allows for precise control over the thickness of the electrode. Silicon's high capacity makes it a promising candidate material for next-generation lithium-ion batteries, but its large volume expansion during cycling ultimately leads to cell failure. To overcome this problem, we investigated the effect of four different polymer binders on the cycling performance of inkjet-printed silicon anodes via ex-situ characterization techniques. Using the conductive polymer PEDOT:PSS as a binder, we demonstrate high capacity retention of over 1000 cycles at a limited depth-of-discharge of 1000 mAh g⁻¹.

3.1 Introduction

Portable energy storage has received worldwide interest as the recent demand for mobile power sources has sky-rocketed. With the miniaturization of wireless devices, rechargeable batteries have had to decrease in size while maintaining the amount of energy stored. Thin film batteries are poised to meet this challenge, as they exhibit a number of unparalleled features including high energy and power densities [1, 2], short ion diffusion lengths [3, 4], and intrinsic flexibility [5, 6]. The successful development of high capacity thin film batteries will enable advances in the fields of wireless sensors, RFID tags, implantable medical devices, and robotics.

Inkjet printing is a promising technique for fabricating thin film electrodes. It can be used to deposit films of precisely controlled thickness, which can be tuned by the number of layers printed on top of one another. It has many advantages over other fabrication techniques, including ease of use, cost-effectiveness, minimal wasted material, scalability, and the ability to deposit patterns. For these reasons, inkjet printing has been successfully used to fabricate supercapacitors [7, 8], transistors [9, 10], and battery electrodes [11, 12]. Commercial graphite anodes for lithium-ion batteries (LIBs), however, cannot meet future energy requirements because of their low theoretical specific capacity (372 mAh/g). Silicon has been widely studied as a candidate to replace graphite [13-16], as it exhibits a high theoretical specific capacity (4200 mAh/g), low lithium extraction potential, and low cost [17, 18].

However, one well-known challenge with using Si as an anode material is its 400% volume expansion upon lithium insertion [19], causing pulverisation of the particles and loss of electrical contact which results in decreased capacity during cycling. Many studies have focused on developing novel nanostructured Si electrodes, such as nanowires [20], nanotubes [21], hollow nanospheres [22], and core-shell structures [23, 24] to overcome the poor cycling stability of Si nanoparticles (SiNPs). However, these synthesis methods typically require large amounts of energy and are not easily translated to commercial mass production. One simpler alternative is to use a polymer binder that can accommodate the volume expansion of SiNPs and maintain electron conduction across the electrode. Previous reports have shown that the mechanical, chemical, and electronic properties of different binders have a significant effect on the cycling performance of SiNPs [25-30].

Herein we prepared inkjet-printed SiNP anodes with four commercially available polymer binders, poly(3,4-ethylenedioxythiophene)-poly(styrene sulfonate) (PEDOT:PSS), polyvinylpyrrolidone (PVP), carboxymethyl cellulose (CMC), and Na-alginate, and investigated their effects on the electrochemical performance of the electrodes in LIBs. We demonstrate that SiNP anodes printed with PEDOT:PSS binder exhibit the most stable cycling at high discharge capacity, due to its excellent jetting properties [31] and electrical conductivity. Scanning electron microscopy (SEM) shows

that PEDOT:PSS conformally coats the SiNPs as a conductive layer, allowing for rapid electron transport while binding the electrode together. *Ex-situ* characterization with SEM, Fourier transform infrared (FTIR) spectroscopy, and Raman spectroscopy reveals that PEDOT:PSS acts as a self-healing polymer, stretching during discharging to effectively accommodate the volume expansion of SiNPs and shrinking during charging to preserve this continuous electronically conductive network.

3.2 Methods

3.2.1 Silicon ink preparation

Inks were prepared by mixing SiNPs (50 nm, Hongwu Nano), carbon black (50 nm, Gunbai), and polymer binder at a ratio of 2:2:1 by weight in an appropriate volume of DI-water to achieve a viscosity of 10 mPa·s, as measured with a U-tube viscometer (Cannon Instrument Company). Four polymer binders were used: PEDOT:PSS (Sigma-Aldrich), PVP (Sigma-Aldrich), CMC (Calbiochem), and sodium alginate (Sigma-Aldrich). Inks were sonicated for at least 3 hours to break up large agglomerates and ensure uniform dispersion prior to use.

3.2.2 Electrode and coin cell preparation

The ink was transferred into a well-cleaned HP 61 ink cartridge and printed using a Hewlett-Packard Deskjet 2540 inkjet printer. Twenty-five layers of each ink were printed on copper foil to ensure sufficient thickness and uniformity. After printing, the films were dried in a vacuum oven at 60°C overnight. The printed films were then cut and assembled in CR-2032 coin cells with lithium metal foil as the counter electrode in an argon-filled glove box. The two electrolytes used were composed of 1 M LiPF₆ salt dissolved in different solvent mixtures: (1) 1:1:1 ratio by volume EC:DEC:EMC and (2) 1:9 ratio by weight FEC:DMC. The coin cells were stored overnight at room temperature before testing.

3.2.3 Characterization

A field emission SEM (Hitachi S-4800) equipped with an EDX spectrometer was used to observe the microstructure and elemental composition of the printed films. Compositional information was also obtained by XRD (Bruker D8 Advance, Cu K α X-ray source) at a grazing incidence angle of 1° and a step size of 0.02°. Galvanostatic charge-discharge measurements were performed on an Arbin BT-2000 battery test station between 0.01 and 1.0V vs. Li/Li⁺. The charge/discharge rates and capacities were calculated based on the mass of Si in the anode, as determined by thermogravimetric analysis (TGA, TA Instruments SDT Q600) (see Figure S3.6). Cyclic voltammetry (CV) (Figure S3.7) and EIS were performed on a multichannel potentiostat 3/Z (VMP3). Ex-situ FTIR spectroscopy (Nicolet 6700) and Raman spectroscopy (532.4 nm laser, HORIBA Scientific LabRAM HR) were performed to analyze anodes with PEDOT:PSS binder before cycling, after first cycle lithiation, and after first cycle delithiation.

3.3 Results

3.3.1 Electrode fabrication and physical characterization

Inkjet printing is a simple method to produce highly uniform thin film electrodes with tunable thicknesses. All inks were prepared with commercially available materials without modification. Ink formulations were comprised of three materials: an electrochemically active material, SiNPs; a conducting agent, carbon black; and one of four polymer binders (Figure 3.1a). These components were mixed in water (Figure 3.1b) and then sonicated for several hours during which large agglomerations of particles were broken up, resulting in a dark brown homogenous suspension (Figure 3.1c). Inks were then transferred into a well-cleaned ink cartridge and printed onto a copper foil current collector with a commercial desktop inkjet printer (Figure 3.1d). The inkjet printing process can be divided into three main stages: droplet ejection and travel, droplet spreading, and droplet solidification. The print head is positioned at the desired location and droplets of ink are forced through the nozzles and are deposited onto the substrate. Upon impact, the deposited droplets spread along the surface and join with other droplets

to form a thin film of liquid ink. Finally, the solvent evaporates and the solid contents of the ink remain on the substrate. To demonstrate the patternability of the inkjet printing technique, the Western University logo was printed using this Si ink on copper foil (Figure 3.1e). In addition, this printing technique uses aqueous solutions, making it an environmentally benign, versatile, and safe fabrication method.

Multiple printing passes were performed to achieve highly uniform films of desired thickness. Printing too few passes resulted in non-uniform films with isolated islands of deposited material, while printing too many passes reduced the electrode's capacity due to higher internal cell resistance (Figure S3.1), consistent with previous reports [32]. The optical images in Figure 3.1f show printed films with 25 layers using the four different polymer binders, along with SEM images demonstrating their morphological differences. These four films were each around 1 μm thick, as measured by cross-section SEM. Energy dispersive X-ray (EDX) spectroscopy mapping demonstrates the uniform distribution of Si within each film (Figure S3.2). The printed anodes with PEDOT:PSS binder exhibited a continuous polymer network, with SiNPs embedded in the matrix. However, the other binders created more discontinuous films containing isolated particles. From this, it is clear that the anodes prepared with PEDOT:PSS are comprised of a single continuous matrix. This is one of the reasons for its superior cycling performance, as will be discussed in the next section.

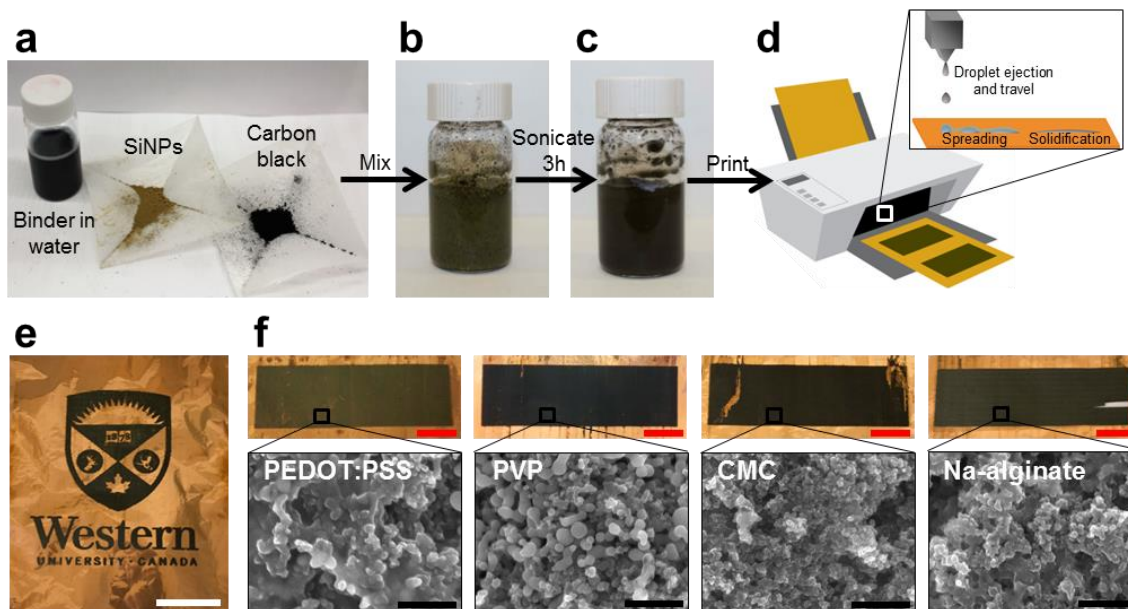


Figure 3.1. Procedure used to print SiNP anodes on copper foil. (a,b) First, the ink was prepared by mixing SiNPs, carbon black, and the polymer binder in water. (c) After 3 hours of sonication, the solution was well-mixed and (d) injected into an inkjet printer cartridge and printed. (e) Photograph of the Western University logo printed with the SiNP ink. (f) Optical photographs and SEM images of the inkjet-printed SiNP anode films on copper foil. Scale bars red, white, and black represent 3 cm, 5 cm, and 500 nm, respectively.

3.3.2 Electrochemical performance

To characterize the electrochemical properties of the inkjet-printed silicon anodes with different polymer binders, deep galvanostatic cycling measurements were performed on printed Si/metallic Li half cells between 0.01 and 1 V (Figure 3.2). At a current rate of 0.1 C (where 1 C = 4200 mA g⁻¹), Si anodes with PEDOT:PSS binder exhibited the most stable cycling performance (Figure 3.2a). Anodes with PEDOT:PSS and PVP binders exhibited very high first-cycle discharge capacities, close to the theoretical value for silicon. Anodes with CMC and sodium alginate binders displayed low initial capacities that rapidly faded to zero within a few cycles. This may be due to low electron

conduction through the electrode, resulting in electrical isolation of SiNPs not adjacent to the current collector, possibly as a result of poor ink-jetting compatibility of these polymer binders. After the first cycle, Si anodes with all binders demonstrated an irreversible capacity loss, which can be attributed to solid electrolyte interphase (SEI) formation. Following this initial drop, anodes prepared with PEDOT:PSS show stable performance for 100 cycles. Furthermore, cells prepared with electrolyte containing dimethyl carbonate and fluoroethylene carbonate (DMC:FEC) demonstrated increased stability compared to those with electrolyte containing ethylene carbonate, diethyl carbonate, and ethyl methyl carbonate (EC:DEC:EMC), with 100th cycle capacities of 1714 mAh g⁻¹ and 961 mAh g⁻¹ based on the mass of Si, respectively. Anodes with PEDOT:PSS binder and DMC:FEC electrolyte were also cycled at 1 C and show excellent performance for 2000 cycles (Figure S3.3). The stabilizing effect of FEC has been previously reported and is attributed to the formation of a more stable SEI layer that prevents cracking of the Si surface [33, 34].

The voltage profiles of printed anodes using PEDOT:PSS binder and DMC:FEC electrolyte are shown in Figure 3.2b. The first cycle exhibits a long plateau around 0.1 V during lithiation, characteristic of crystalline silicon. Subsequent cycles have sloping plateau regions between 0.3 and 0.01 V vs. Li/Li⁺, indicative of lithium insertion into amorphous Li_xSi [35].

PEDOT:PSS forms a continuous and conductive network that connects SiNPs to the current collector, providing rapid electron transport at elevated current densities. The specific capacity of an inkjet-printed silicon anode with PEDOT:PSS binder varied from 2500 mAh g⁻¹ at 0.1 C to 900 mAh g⁻¹ at 5 C (Figure 3.2c). Even at a charge/discharge rate of 2 C, a sloping plateau region is observed between 0.25 and 0.01 V vs. Li/Li⁺ (Figure 3.2d), similar to those shown in Figure 3.2b. This demonstrates the ability of lithium ions to rapidly penetrate the PEDOT:PSS coating and alloy with the Si at high cycling rates. However, no obvious plateau is observed in the charging profile when cycling at 5 C, due to increasing polarization under high current densities.

Limited depth-of-discharge measurements were also carried out to a capacity cut-off of 1000 mAh g⁻¹ at 0.1C (Figure 3.2e). Cells were also limited to a maximum charging voltage of 2.5 V to prevent oxidation and dissolution of the copper current collector. Anodes prepared with binders other than PEDOT:PSS faded rapidly. Cells made with EC:DEC:EMC electrolyte and PEDOT:PSS binder lasted only 150 cycles at 1000 mAh g⁻¹ before fading. When using DMC:FEC electrolyte, printed Si anodes with PEDOT:PSS binder exhibited further superior cycling stability, with over 600 cycles at 1000 mAh g⁻¹. This can be attributed to less stable SEI formation of the EC-based electrolyte than of the FEC-based electrolyte. To compare the inkjet printing technique to conventional fabrication methods, anodes with Na-alginate and poly(vinylidene fluoride) (PVDF) binders were also prepared using the conventional doctor-blade casting method. These anodes were unable to maintain a discharge capacity of 1000 mAh g⁻¹ after 22 and 5 cycles for Na-alginate and PVDF binders, respectively. Previous studies have shown that PVDF is unable to accommodate the large volume changes during the lithiation of silicon, causing the binder to detach from the current collector and leading to increased cell resistance and poor cycling performance [36].

The Coulombic efficiency (CE) of the Si anode with PEDOT:PSS binder in DMC:FEC is 31% and 75% for the first two cycles and increases to around 98.6% for the remaining cycles. The low CE for the first two cycles is attributed to irreversible capacity loss from SEI formation. High initial resistance of the cell, as measured by electrochemical impedance spectroscopy (EIS) (Figure S3.4), may also contribute to the low first-cycle CE. Once a stable SEI is formed, the CE remains constant and the anodes continue to exhibit a stable capacity of 1000 mAh g⁻¹. However, by the 5th cycle the charge capacity reaches nearly 1000 mAh g⁻¹ and the CE remains stable. The discharge plateaus remain relatively constant during cycling and all discharge plateaus occur at lower voltages than the first cycle, indicating a decreased internal resistance.

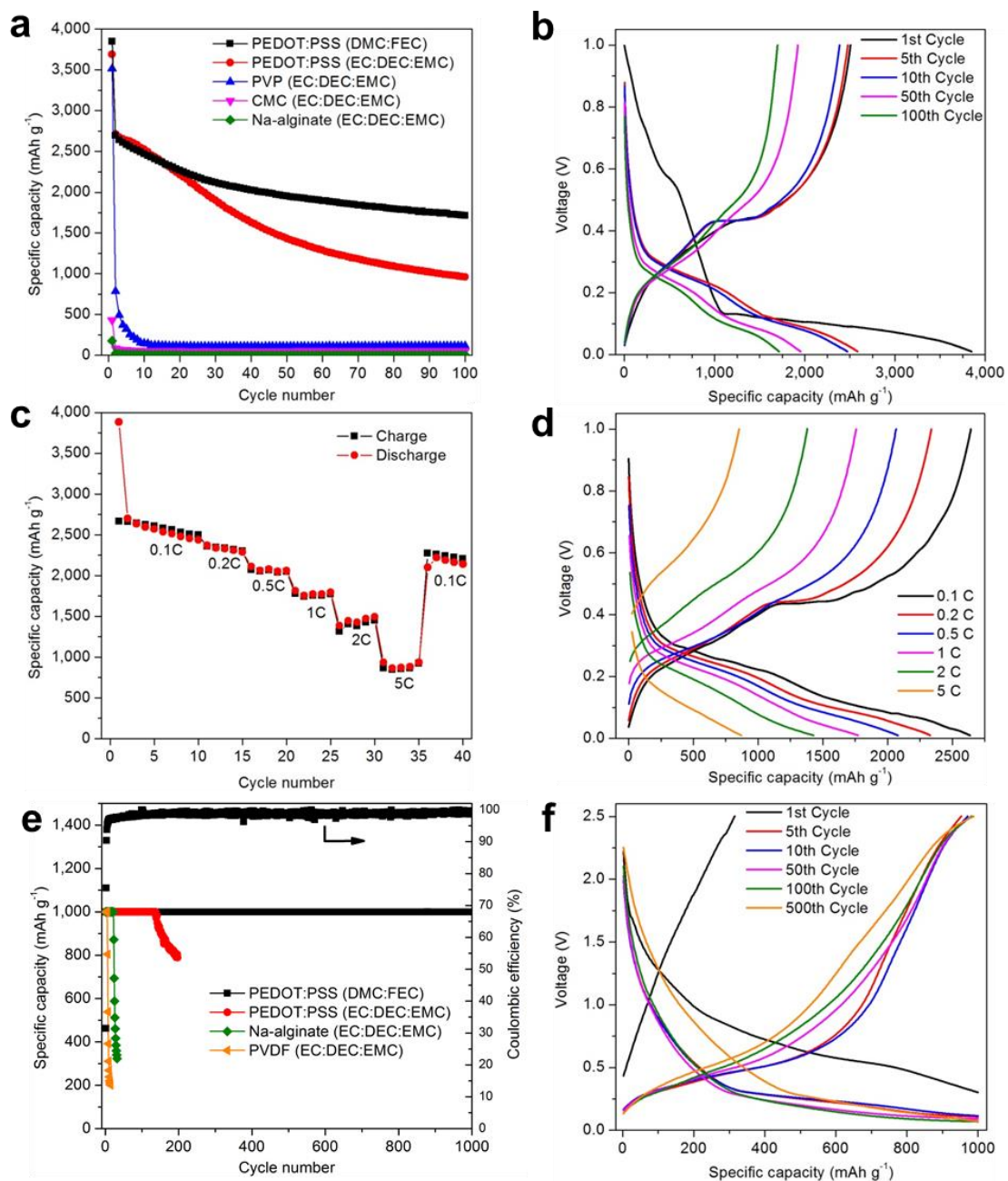


Figure 3.2. (a) Cycling performance of inkjet-printed silicon anodes prepared with different polymer binders at 0.1C. (b) Voltage profiles of selected cycles for the PEDOT:PSS (DMC:FEC) cell from (a). (c, d) Rate capability measurements of Si anodes with PEDOT:PSS binder in DMC:FEC electrolyte. (e) Limited depth-of-discharge tests performed to a capacity cut-off of 1000 mAh g^{-1} . The Coulombic efficiency shown is for PEDOT:PSS (DMC:FEC). (f) Voltage profiles of selected cycles for the PEDOT:PSS (DMC:FEC) cell shown in (e).

3.3.3 Physical characterization

Ex-situ measurements were taken at three stages of the charge/discharge cycle of anodes prepared with PEDOT:PSS binder: before cycling, after lithiation, and after delithiation. As seen in the SEM images shown in Figure 3.3a, the anode began in the pristine state as a continuous polymer network with embedded SiNPs. Upon lithiation the SiNPs expanded, causing the polymer binder to stretch into a fibrous structure. After delithiation, the SiNPs contracted and the morphology of the electrode returned to its pristine condition, indicating that the PEDOT:PSS network remains intact during volume expansion and is able to maintain intimate contact with the SiNPs. The continuous conductive network is preserved, ensuring that all SiNPs remain electrically connected to the current collector, which is critical to the overall electrochemical performance of the electrode.

Furthermore, this self-healing effect is also consistent with results obtained from FTIR (Figure 3.3b) and Raman (Figure S3.5) spectroscopy. The IR peaks at 1635 and 667 cm^{-1} represent C=C stretching and C-S stretching in the thiophene ring, respectively [37-39]. Upon lithiation the intensity of both these peaks decreases, indicating reduced stretching vibrations in the thiophene ring of the PEDOT chain. This can be explained by considering the structure of PEDOT:PSS (Figure 3.3c). In the initial state, positively-charged thiophene groups exist in the PEDOT molecules and negatively-charged sulfonyl groups exist in the PSS molecules, which stabilize one another by electrostatic attraction. The lower electron densities in the positive thiophene rings result in more asymmetric stretching vibrations compared to the neutral thiophene rings. When the polymer chains stretch during lithiation, the PEDOT and PSS molecules slide past one another, reducing the interaction between the two polymer units. The decreased number of sulfonyl groups nearby to stabilize positively-charged thiophene rings leads to a decreased number of positive thiophene rings. The increased electron density of the neutral thiophene groups suppresses the asymmetric stretching modes of the C=C and C-S bonds in PEDOT, resulting in a lower IR absorbance. During delithiation, the polymer chains contract, increasing the interaction between PEDOT and PSS molecules and therefore increasing the number of positively-charged thiophene rings, as evident from the return of the IR

intensity to that of the pristine state. This explanation is further supported by changes to the IR peaks at 1382 and 648 cm^{-1} , which represent S=O stretching and S-O stretching, respectively [39, 40]. Similar to above, these peaks are present in the IR spectra of the pristine and delithiated samples, but absent in that of the lithiated electrode. This is due to the suppressed asymmetric stretching of the sulfonic acid groups in PSS when Li^+ ions are available to ionically stabilize the negative sulfonyl groups that were previously paired with the positive thiophene ring in the pristine and delithiated electrodes. These IR results provide more evidence for the mechanism of the self-healing effect of the PEDOT:PSS binder as shown in the SEM images.

The additional peak at 864 cm^{-1} corresponds to residual LiPF_6 [41, 42] and the peaks at 1435 and 1508 cm^{-1} are attributable to the formation of Li_2CO_3 or other organic carbonates in the SEI [42, 43]. As expected, these peaks appear after lithiation and are not present in the pristine state. The SEI peaks are still present after delithiation, indicating irreversible SEI formation. This also supports the cycling performance results above, in which there is significant irreversible capacity loss after the first cycle. The SEI formed at the PEDOT-electrolyte interface may differ chemically and mechanically from the SEI formed at the Si-electrolyte interface, and it has been suggested that this difference may also contribute to improved cycling stability [44].

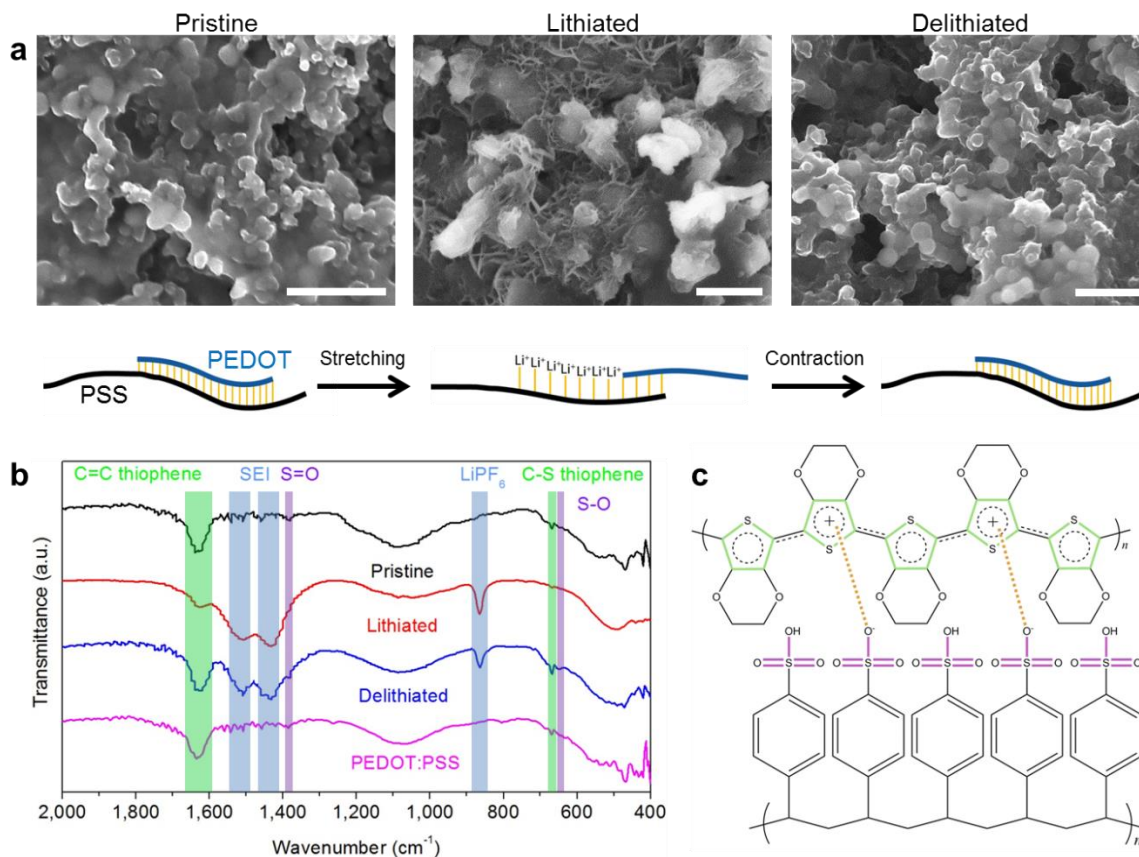


Figure 3.3. Ex-situ (a) SEM images and (b) FTIR spectra of SiNP anodes with PEDOT:PSS binder taken at three stages of a discharge/charge cycle: before cycling (pristine), after first discharge (lithiated), and after first full discharge and charge (delithiated). The green highlighted regions in the FTIR spectra indicate the PEDOT:PSS thiophene C=C and C-S stretching vibrations, the blue highlighted regions indicate SEI formation and residual electrolyte salt, and the purple highlighted regions indicate the sulfonic acid groups. (c) The structure of PEDOT:PSS. Scale bars are 500 nm.

3.4 Discussion

The superior performance of the inkjet-printed silicon anodes with PEDOT:PSS binder can be attributed to the favourable properties of PEDOT:PSS. First, the PEDOT:PSS formulation used was specifically designed for use in inkjet printers, with optimal

viscosity, surface tension, and density for ideal jetting conditions. It therefore readily formed uniform films without modification. Second, PEDOT:PSS is both electrically and ionically conductive. A conductive network is maintained during cycling, ensuring that SiNPs do not become electrically isolated while simultaneously allowing lithium ions to migrate to and alloy with the SiNPs. Third, PEDOT:PSS is able to reversibly deform, allowing it to stretch and contract with the SiNPs and accommodate the large volume changes. It is also rigid enough to confine any particles that fracture during cycling. Additionally, there may be a chemical interaction between Si and PEDOT:PSS that stabilizes the electrode structure during charging/discharging [45].

An explanation of the varying electrochemical performance of printed Si anodes prepared with different binders is proposed in Figure 3.4. First, CMC and Na-alginate binders surround groups of SiNPs and carbon black, electrically isolating them from each other. There are no electron conduction pathways to these isolated particles, and therefore only SiNPs in direct contact with the current collector can contribute to energy storage. This results in the low initial capacity of electrodes prepared with these binders.

In the case of PVP, a continuous conductive network of carbon black initially exists, so that SiNPs not in direct contact with the current collector are electrically connected. Printed Si anodes prepared with PVP therefore exhibited high initial capacities. However, as the SiNPs expand and contract they lose contact with the conductive carbon black. The conductive network becomes disrupted after only a few lithiation and delithiation cycles and the battery's capacity rapidly decreases.

Similar to PVP, PEDOT:PSS initially forms a conductive network of carbon black. However, when SiNPs become disconnected from the carbon black network, they maintain electrical contact with the remainder of the electrode through the conductive PEDOT:PSS matrix. Printed Si anodes prepared with PEDOT:PSS thereby exhibited high initial capacities and more stable performance than anodes prepared with non-conductive polymer binders. This mechanism is also consistent with other reported conductive binders for Si electrodes, such as polypyrrole [46], polyaniline [30], and poly(9,9-dioctylfluorene-co-fluorenone-co-methylbenzoic acid) (PFFOMB) [47]. However,

compared to other studies, the PEDOT:PSS formulation used here is commercially available with no modification or polymerization required, which is favourable for printing technology.

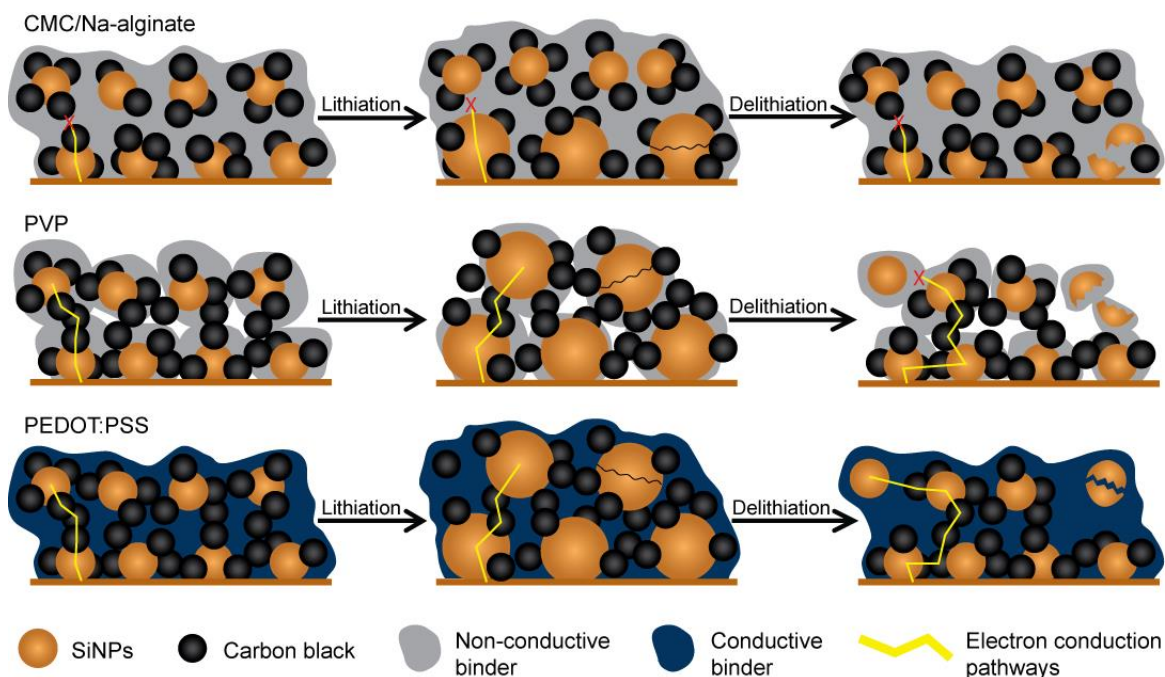


Figure 3.4. Schematic illustration of the proposed mechanism explaining the electrochemical performance of anodes prepared with different binders. The use of non-conductive binders (CMC, Na-alginate, and PVP) leads to electrical isolation of SiNPs. In the case of CMC and Na-alginate, electrical isolation occurs from the start, leading to poor initial capacity, while in the case of PVP the conductive carbon black network is destroyed during large volume changes. With PEDOT:PSS, the SiNPs remain electrically connected throughout charging/discharging and are therefore able to maintain a stable cycling capacity.

3.5 Conclusions

In conclusion, SiNP anodes were fabricated for the first time by inkjet printing. Inkjet printing resulted in very uniform, thin film electrodes with precise control over the thickness. The effect of the binder on cycling performance was investigated and anodes

with PEDOT:PSS binder were the most stable, attributed to its electrical conductivity and reversible deformation upon electrode expansion. The continuous conductive network formed by PEDOT:PSS allows for rapid electron transfer and, at the same time, stretches to accommodate the large volume changes of SiNPs during charging and discharging. These anodes exhibit very high capacities of greater than 1700 mAh g^{-1} for 100 cycles, as well as very stable cycling performance when cycled at a limited depth-of-discharge of 1000 mAh g^{-1} , with over 600 successful cycles. Anodes prepared with non-conductive polymer binders, on the other hand, had capacities that quickly degraded to zero after only a few cycles. This was attributed to some SiNPs losing electrical contact with the remaining electrode each cycle, preventing them from contributing to capacity. This proposed mechanism was supported with *ex-situ* SEM, FTIR, and Raman spectroscopy measurements. Overall, we have shown that inkjet printing is a viable fabrication method for high capacity thin film Si electrodes and that the polymer binder plays an important role in the electrochemical behavior of printed electrodes. This technique may be extended to other electrode materials as well as a printable electrolyte, for the fabrication of a fully inkjet-printed cell.

Acknowledgements

This work was supported by the Natural Sciences and Engineering Research Council of Canada (NSERC), Canada Research Chair (CRC) Program, Canada Foundation for Innovation (CFI), Ontario Research Fund (ORF), and University of Western Ontario. Stephen Lawes also acknowledges the Province of Ontario and the University of Western Ontario for the Queen Elizabeth II Graduate Scholarship in Science and Technology.

References

- [1] D. Wei, S. Haque, P. Andrew, J. Kivioja, T. Ryhänen, A. Pesquera, A. Centeno, B. Alonso, A. Chuvilin, and A. Zurutuza, "Ultrathin rechargeable all-solid-state batteries based on monolayer graphene," *Journal of Materials Chemistry A*, vol. 1, pp. 3177-3781, 2013.

- [2] S. Liu, Z. Wang, C. Yu, H. B. Wu, G. Wang, Q. Dong, J. Qiu, A. Eychmuller, and X. W. David Lou, "A flexible TiO₂(B)-based battery electrode with superior power rate and ultralong cycle life," *Advanced Materials*, vol. 25, pp. 3462-3467, 2013.
- [3] J. Schwenzel, V. Thangadurai, and W. Weppner, "Developments of high-voltage all-solid-state thin-film lithium ion batteries," *Journal of Power Sources*, vol. 154, pp. 232-238, 2006.
- [4] N. Li, Z. Chen, W. Ren, F. Li, and H.-M. Cheng, "Flexible graphene-based lithium ion batteries with ultrafast charge and discharge rates," *Proceedings of the National Academy of Sciences of the United States of America*, vol. 109, pp. 17360-17365, 2012.
- [5] N. J. Dudney, "Thin Film Micro-Batteries," *Electrochemical Society Interface*, vol. 17, pp. 44-48, 2008.
- [6] L. Hu, H. Wu, F. La Mantia, Y. Yang, and Y. Cui, "Thin, Flexible Secondary Li-Ion Paper Batteries," *ACS Nano*, vol. 4, pp. 5843-5848, 2010.
- [7] P. Chen, H. Chen, J. Qiu, and C. Zhou, "Inkjet printing of single-walled carbon nanotube/RuO₂ nanowire supercapacitors on cloth fabrics and flexible substrates," *Nano Research*, vol. 3, pp. 594-603, 2010.
- [8] L. T. Le, M. H. Ervin, H. Qiu, B. E. Fuchs, and W. Y. Lee, "Graphene supercapacitor electrodes fabricated by inkjet printing and thermal reduction of graphene oxide," *Electrochemistry Communications*, vol. 13, pp. 355-358, 2011.
- [9] N. Stutzmann, R. H. Friend, and H. Sirringhaus, "Self-aligned, vertical-channel, polymer field-effect transistors," *Science*, vol. 299, pp. 1881-4, 2003.
- [10] T. Kawase, T. Shimoda, C. Newsome, H. Sirringhaus, and R. H. Friend, "Inkjet printing of polymer thin film transistors," *Thin Solid Films*, vol. 438-439, pp. 279-287, 2003.
- [11] M.-S. Park, S.-H. Hyun, and S.-C. Nam, "Mechanical and electrical properties of a LiCoO₂ cathode prepared by screen-printing for a lithium-ion micro-battery," *Electrochimica Acta*, vol. 52, pp. 7895-7902, 2007.
- [12] J. Huang, J. Yang, W. Li, W. Cai, and Z. Jiang, "Electrochemical properties of LiCoO₂ thin film electrode prepared by ink-jet printing technique," *Thin Solid Films*, vol. 516, pp. 3314-3319, 2008.
- [13] H. Li, Z. Wang, L. Chen, and X. Huang, "Research on Advanced Materials for Li-ion Batteries," *Advanced Materials*, vol. 21, pp. 4593-4607, 2009.
- [14] M. T. McDowell, S. W. Lee, W. D. Nix, and Y. Cui, "25th Anniversary Article: Understanding the Lithiation of Silicon and Other Alloying Anodes for Lithium-Ion Batteries," *Advanced Materials*, vol. 25, pp. 4966-4985, 2013.

- [15] M. R. Zamfir, H. T. Nguyen, E. Moyon, Y. H. Lee, and D. Pribat, "Silicon nanowires for Li-based battery anodes: a review," *Journal of Materials Chemistry A*, vol. 1, pp. 9566-9586, 2013.
- [16] X. Su, Q. Wu, J. Li, X. Xiao, A. Lott, W. Lu, B. W. Sheldon, and J. Wu, "Silicon-Based Nanomaterials for Lithium-Ion Batteries: A Review," *Advanced Energy Materials*, vol. 4, pp. 1300882, 2014.
- [17] B. A. Boukamp, G. C. Lesh, and R. A. Huggins, "All-Solid Lithium Electrodes with Mixed-Conductor Matrix," *Journal of The Electrochemical Society*, vol. 128, pp. 725-729, 1981.
- [18] W. J. Weydanz, M. Wohlfahrt-Mehrens, and R. A. Huggins, "A room temperature study of the binary lithium-silicon and the ternary lithium-chromium-silicon system for use in rechargeable lithium batteries," *Journal of Power Sources*, vol. 81-82, pp. 237-242, 1999.
- [19] U. Kasavajjula, C. Wang, and A. J. Appleby, "Nano- and bulk-silicon-based insertion anodes for lithium-ion secondary cells," *Journal of Power Sources*, vol. 163, pp. 1003-1039, 2007.
- [20] C. K. Chan, H. Peng, G. Liu, K. McIlwrath, X. F. Zhang, R. A. Huggins, and Y. Cui, "High-performance lithium battery anodes using silicon nanowires," *Nat Nano*, vol. 3, pp. 31-35, 2008.
- [21] M.-H. Park, M. G. Kim, J. Joo, K. Kim, J. Kim, S. Ahn, Y. Cui, and J. Cho, "Silicon Nanotube Battery Anodes," *Nano Letters*, vol. 9, pp. 3844-3847, 2009.
- [22] Y. Yao, M. T. McDowell, I. Ryu, H. Wu, N. Liu, L. Hu, W. D. Nix, and Y. Cui, "Interconnected Silicon Hollow Nanospheres for Lithium-Ion Battery Anodes with Long Cycle Life," *Nano Letters*, vol. 11, pp. 2949-2954, 2011.
- [23] H. Kim and J. Cho, "Superior Lithium Electroactive Mesoporous Si@Carbon Core-Shell Nanowires for Lithium Battery Anode Material," *Nano Letters*, vol. 8, pp. 3688-3691, 2008.
- [24] P. Gao, J. Fu, J. Yang, R. Lv, J. Wang, Y. Nuli, and X. Tang, "Microporous carbon coated silicon core/shell nanocomposite via in situ polymerization for advanced Li-ion battery anode material," *Physical Chemistry Chemical Physics*, vol. 11, pp. 11101-11105, 2009.
- [25] F. M. Courtel, S. Niketic, D. Duguay, Y. Abu-Lebdeh, and I. J. Davidson, "Water-soluble binders for MCMB carbon anodes for lithium-ion batteries," *Journal of Power Sources*, vol. 196, pp. 2128-2134, 2011.
- [26] I. Kovalenko, B. Zdyrko, A. Magasinski, B. Hertzberg, Z. Milicev, R. Burtovyy, I. Luginov, and G. Yushin, "A major constituent of brown algae for use in high-capacity Li-ion batteries," *Science*, vol. 334, pp. 75-9, 2011.

- [27] H. Buqa, M. Holzapfel, F. Krumeich, C. Veit, and P. Novák, "Study of styrene butadiene rubber and sodium methyl cellulose as binder for negative electrodes in lithium-ion batteries," *Journal of Power Sources*, vol. 161, pp. 617-622, 2006.
- [28] N. S. Hochgatterer, M. R. Schweiger, S. Koller, P. R. Raimann, T. Wöhrle, C. Wurm, and M. Winter, "Silicon/Graphite Composite Electrodes for High-Capacity Anodes: Influence of Binder Chemistry on Cycling Stability," *Electrochemical and Solid-State Letters*, vol. 11, p. A76, 2008.
- [29] W.-R. Liu, M.-H. Yang, H.-C. Wu, S. M. Chiao, and N.-L. Wu, "Enhanced Cycle Life of Si Anode for Li-Ion Batteries by Using Modified Elastomeric Binder," *Electrochemical and Solid-State Letters*, vol. 8, p. A100, 2005.
- [30] H. Wu, G. Yu, L. Pan, N. Liu, M. T. McDowell, Z. Bao, and Y. Cui, "Stable Li-ion battery anodes by in-situ polymerization of conducting hydrogel to conformally coat silicon nanoparticles," *Nat Commun*, vol. 4, 2013.
- [31] S. D. Hoath, S. Jung, W.-K. Hsiao, and I. M. Hutchings, "How PEDOT:PSS solutions produce satellite-free inkjets," *Organic Electronics*, vol. 13, pp. 3259-3262, 2012.
- [32] N. J. Dudney and Y.-I. Jang, "Analysis of thin-film lithium batteries with cathodes of 50 nm to 4 μm thick LiCoO_2 ," *Journal of Power Sources*, vol. 119-121, pp. 300-304, 2003.
- [33] C. Xu, F. Lindgren, B. Philippe, M. Gorgoi, F. Björefors, K. Edström, and T. Gustafsson, "Improved Performance of the Silicon Anode for Li-Ion Batteries: Understanding the Surface Modification Mechanism of Fluoroethylene Carbonate as an Effective Electrolyte Additive," *Chemistry of Materials*, vol. 27, pp. 2591-2599, 2015.
- [34] Y.-M. Lin, K. C. Klavetter, P. R. Abel, N. C. Davy, J. L. Snider, A. Heller, and C. B. Mullins, "High performance silicon nanoparticle anode in fluoroethylene carbonate-based electrolyte for Li-ion batteries," *Chemical Communications*, vol. 48, pp. 7268-7270, 2012.
- [35] C.-M. Park, J.-H. Kim, H. Kim, and H.-J. Sohn, "Li-alloy based anode materials for Li secondary batteries," *Chemical Society Reviews*, vol. 39, pp. 3115-3141, 2010.
- [36] S. Komaba, N. Yabuuchi, T. Ozeki, Z.-J. Han, K. Shimomura, H. Yui, Y. Katayama, and T. Miura, "Comparative Study of Sodium Polyacrylate and Poly(vinylidene fluoride) as Binders for High Capacity Si-Graphite Composite Negative Electrodes in Li-Ion Batteries," *The Journal of Physical Chemistry C*, vol. 116, pp. 1380-1389, 2011.
- [37] C. Sriprachubwong, C. Karuwan, A. Wisitsorratt, D. Phokharatkul, T. Lomas, P. Sritongkham, and A. Tuantranont, "Inkjet-printed graphene-PEDOT:PSS modified screen printed carbon electrode for biochemical sensing," *Journal of Materials Chemistry*, vol. 22, pp. 5478-5485, 2012.

- [38] Y. Xiao, J.-Y. Lin, S.-Y. Tai, S.-W. Chou, G. Yue, and J. Wu, "Pulse electropolymerization of high performance PEDOT/MWCNT counter electrodes for Pt-free dye-sensitized solar cells," *Journal of Materials Chemistry*, vol. 22, pp. 19919-19925, 2012.
- [39] D. Pavia, G. Lampman, G. Kriz, and J. Vyvyan, *Introduction to Spectroscopy*, 4th ed. Belmont, CA: Cengage Learning, 2009.
- [40] M. Marti, G. Fabregat, F. Estrany, C. Aleman, and E. Armelin, "Nanostructured conducting polymer for dopamine detection," *Journal of Materials Chemistry*, vol. 20, pp. 10652-10660, 2010.
- [41] A. Xiao, L. Yang, B. L. Lucht, S.-H. Kang, and D. P. Abraham, "Examining the Solid Electrolyte Interphase on Binder-Free Graphite Electrodes," *Journal of the Electrochemical Society*, vol. 156, pp. A318-A327, 2009.
- [42] M. Nie, D. P. Abraham, Y. Chen, A. Bose, and B. L. Lucht, "Silicon Solid Electrolyte Interphase (SEI) of Lithium Ion Battery Characterized by Microscopy and Spectroscopy," *The Journal of Physical Chemistry C*, vol. 117, pp. 13403-13412, 2013.
- [43] T. Zhang and H. Zhou, "A reversible long-life lithium-air battery in ambient air," *Nat Commun*, vol. 4, p. 1817, 2013.
- [44] Y. Yao, N. Liu, M. T. McDowell, M. Pasta, and Y. Cui, "Improving the cycling stability of silicon nanowire anodes with conducting polymer coatings," *Energy & Environmental Science*, vol. 5, pp. 7927-7930, 2012.
- [45] D. Shao, H. Zhong, and L. Zhang, "Water-Soluble Conductive Composite Binder Containing PEDOT:PSS as Conduction Promoting Agent for Si Anode of Lithium-Ion Batteries," *ChemElectroChem*, vol. 1, pp. 1679-1687, 2014.
- [46] Z. Du, S. Zhang, Y. Liu, J. Zhao, R. Lin, and T. Jiang, "Facile fabrication of reticular polypyrrole-silicon core-shell nanofibers for high performance lithium storage," *Journal of Materials Chemistry*, vol. 22, pp. 11636-11641, 2012.
- [47] G. Liu, S. Xun, N. Vukmirovic, X. Song, P. Olalde-Velasco, H. Zheng, V. S. Battaglia, L. Wang, and W. Yang, "Polymers with tailored electronic structure for high capacity lithium battery electrodes," *Advanced Materials*, vol. 23, pp. 4679-83, 2011.

Supporting Information

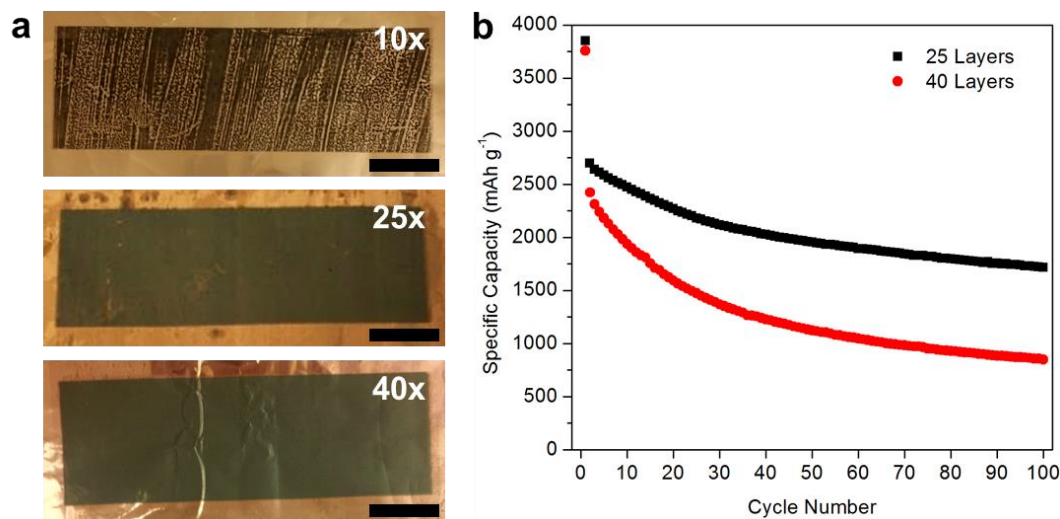


Figure S3.1. (a) Photographs of printed films with different numbers of printing passes. Too few passes (10x) results in non-uniform films that cannot be used for electrodes. More passes (25x and 40x) result in uniform films. However, too many passes decreases capacity. (b) Discharge capacity of Si anodes with PEDOT:PSS binder and DMC:FEC electrolyte, with different numbers of printing passes.

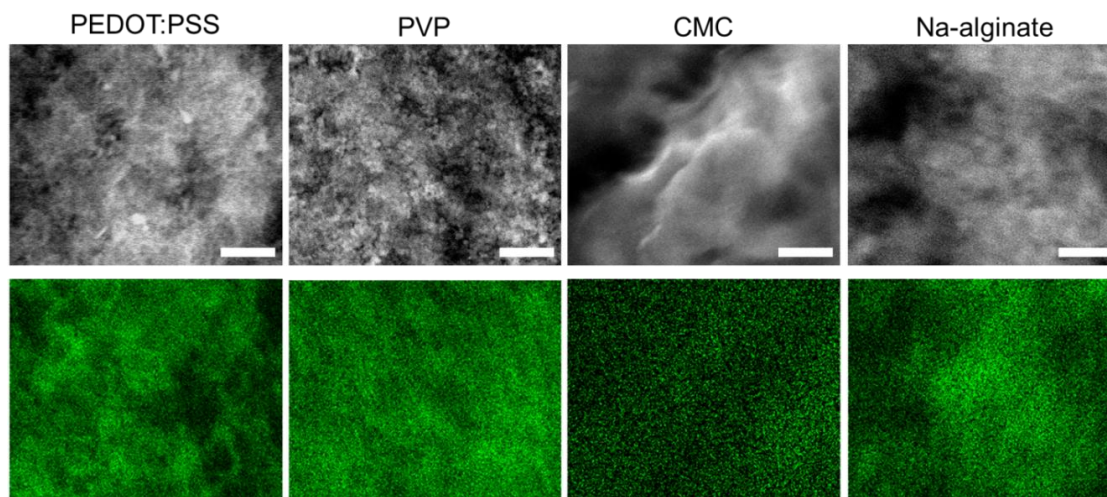


Figure S3.2. EDX mapping of inkjet printed Si films with four different binders, each prepared with 25 printing passes. The top images show the SEM image of where the mapping was performed and the bottom images show the EDX mapping for Si. All four films show uniform Si dispersion throughout, with some fluctuations due to variations in the surface morphology. Scale bars are 2 μm.

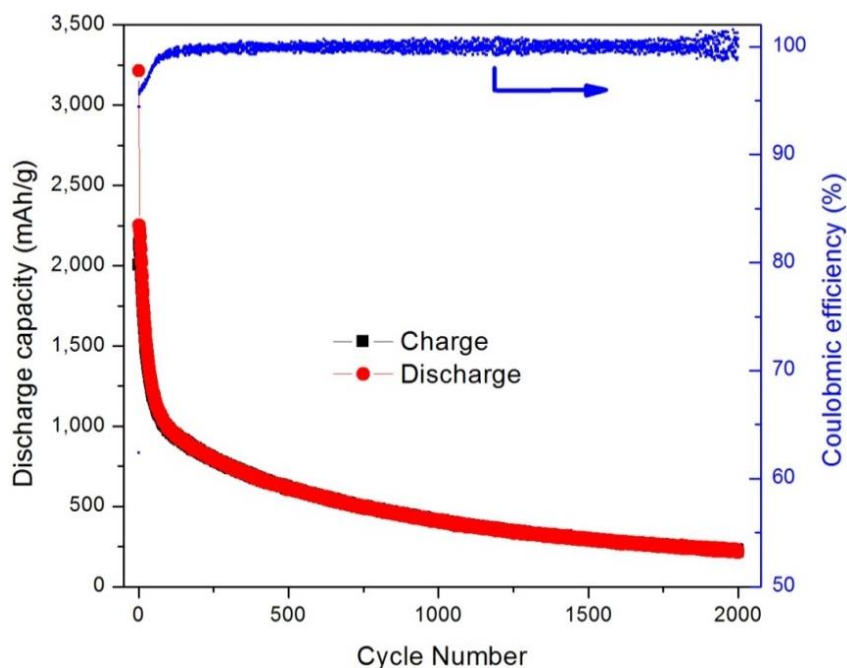


Figure S3.3. Cycling performance of Si anodes with PEDOT:PSS binder and DMC:FEC electrolyte at 1 C. The average CE over 2000 cycles is 99.8%.

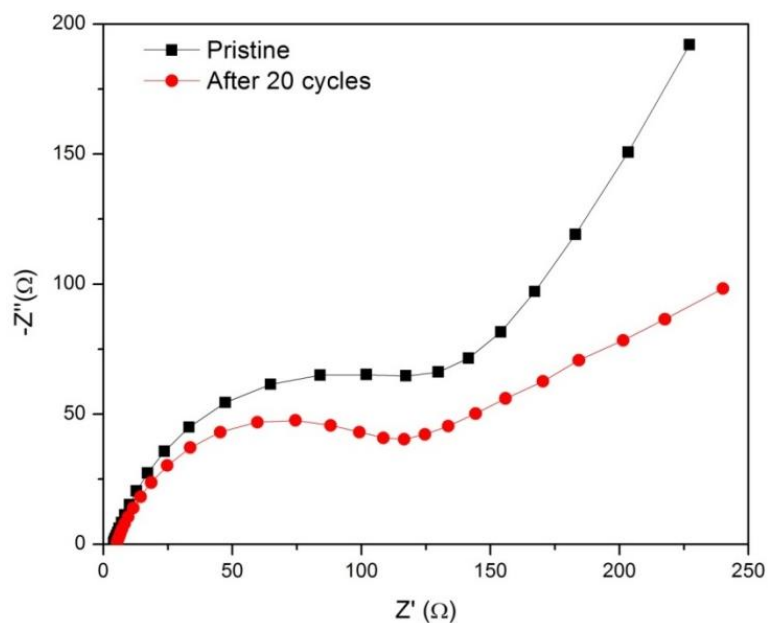


Figure S3.4. EIS spectra of inkjet printed SiNP anodes prepared with PEDOT:PSS binder. Cells were fabricated with EC:DEC:EMC electrolyte. The electrode starts with relatively high impedance that decreases during cycling. This may be due to increased electrolyte wetting of the printed anode layers and the higher conductivity of Li-doped Si, as discussed in [30].

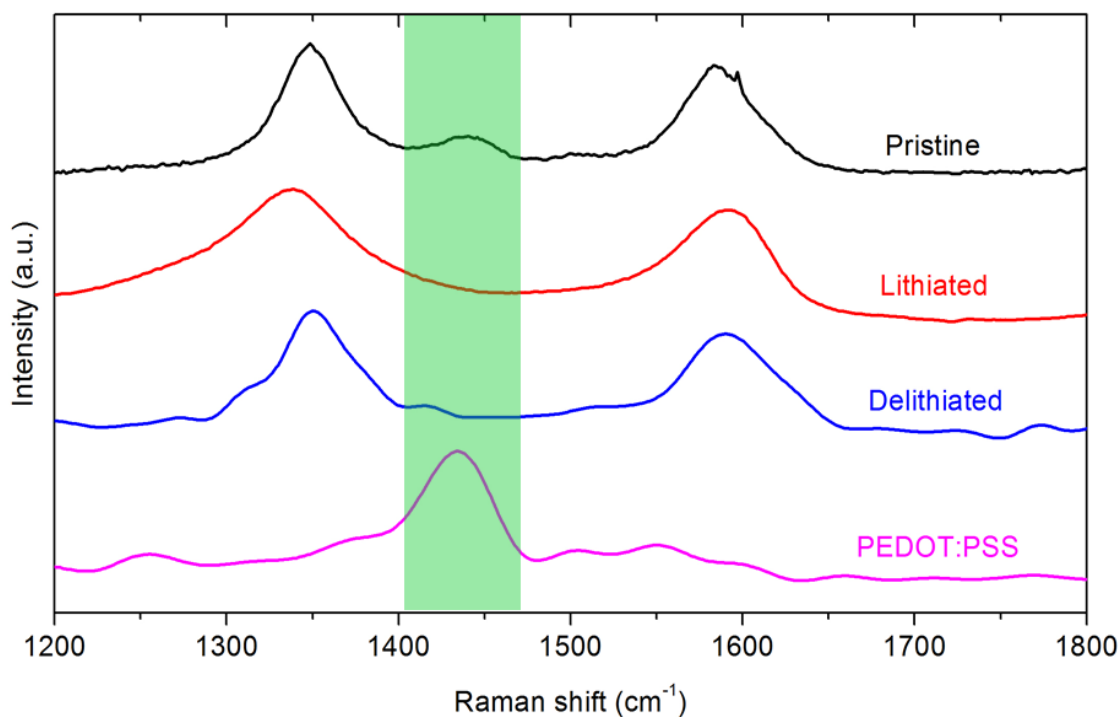


Figure S3.5. Raman spectra taken at three stages of a discharge/charge cycle: before cycling (pristine), after one discharge cycle (lithiated), and after one full discharge/charge cycle (delithiated). The peak at 1435 cm^{-1} represents thiophene ring stretching vibrations, from the thiophene ring present in the PEDOT molecules. Similar to the C=C and C-S thiophene stretching shown in the FTIR spectra, the thiophene ring stretching peak disappears after lithiation, due to stretching being inhibited by the already stretched polymer chains. However, after delithiation there is no return of this peak. This may be due to the SEI binding to the PEDOT molecules and preventing further stretching of the thiophene rings.

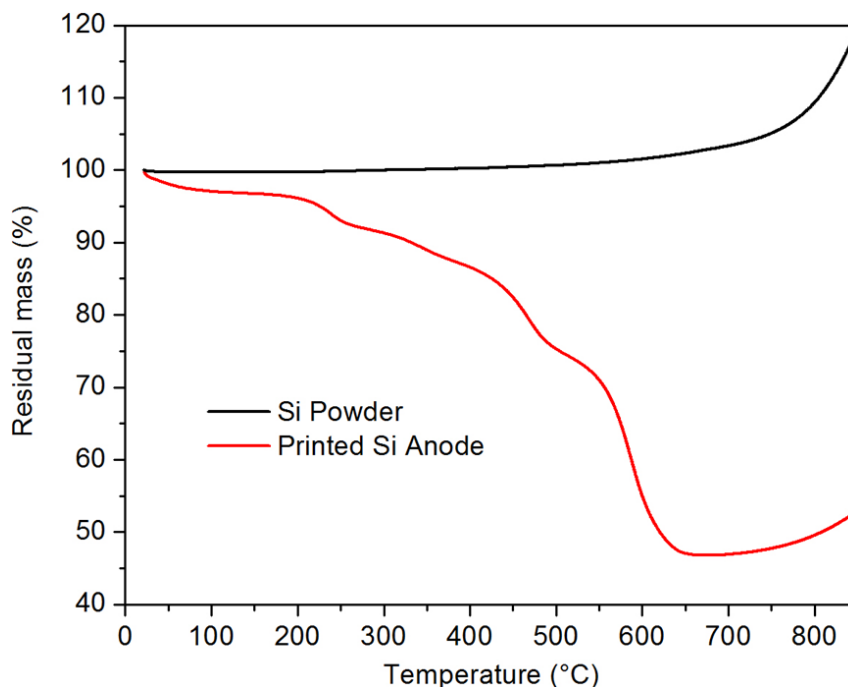


Figure S3.6. TGA of a film of inkjet printed SiNP anode material prepared with PEDOT:PSS binder, used to determine the mass percentage of Si in the printed films. Since Si is stable in the temperature range used here, all mass loss is due to the removal of the polymer binder and carbon black. We therefore used the minimum point (46%) on the curve as the % mass of Si in the anode for calculating charge/discharge rates and capacities. To confirm that this assumption was valid, we also measured a sample of Si powder. No mass loss was observed; in fact, oxidation of the SiNPs resulted in a mass gain. This increase is negligible (2%) at the minimum point of the printed Si anode curve and will anyways result in lower reported capacity values.

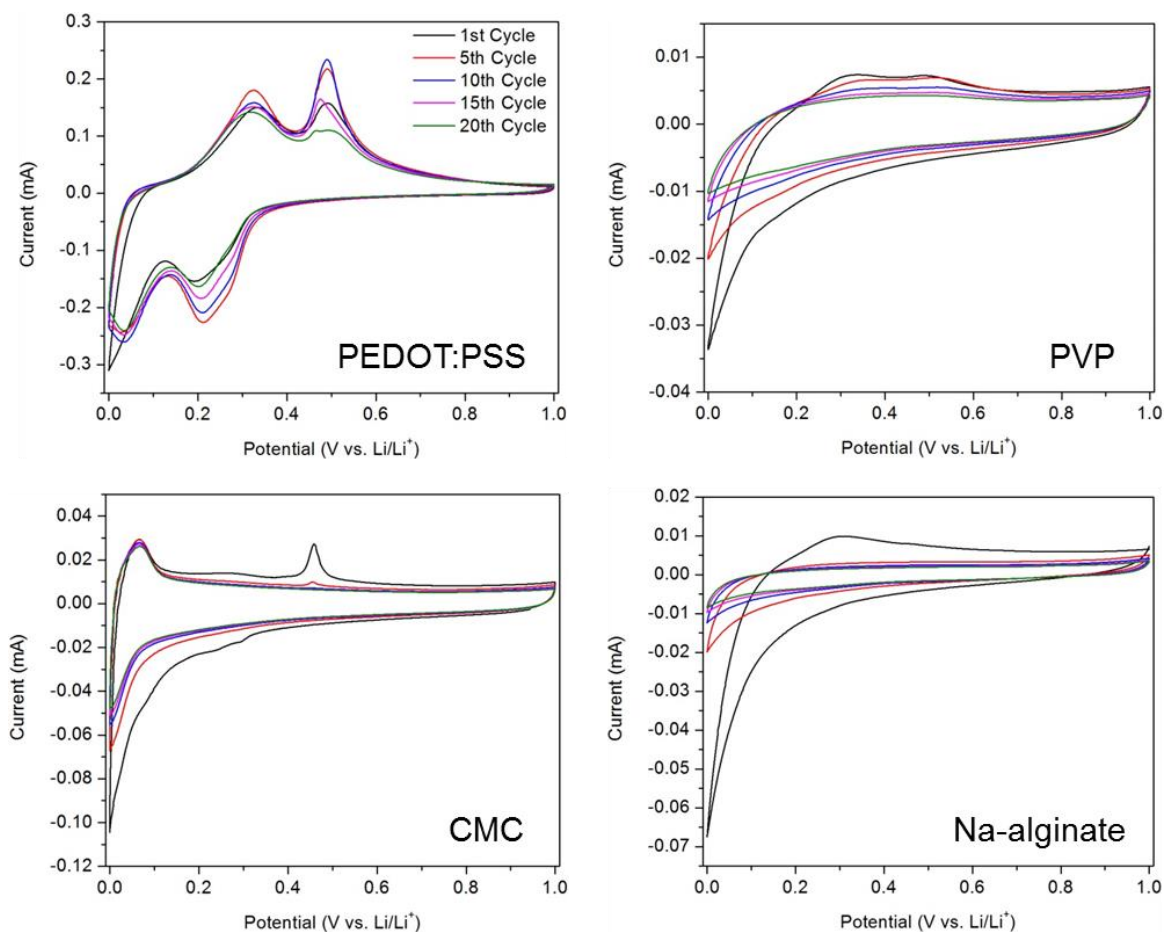


Figure S3.7. Cyclic voltammety curves of inkjet printed SiNP anodes prepared with four different binders. All cells were fabricated with EC:DEC:EMC electrolyte.

Chapter 4

4 High performance inkjet-printed titanium dioxide anodes for lithium-ion batteries

*This chapter is to be submitted for peer-reviewed publication.

A facile and economical inkjet printing technique was developed to fabricate thin film titanium dioxide anodes for lithium-ion batteries with a desktop inkjet printer. The home-made ink, composed of stable dispersions of TiO₂ nanoparticles, carbon black, and polymer binder, was printed on copper foil substrates. The thickness of the thin film electrodes could be precisely controlled by printing multiple layers in succession, with each layer having a thickness of about 125 nm. The morphology, composition, and electrochemical performance of the TiO₂ anodes were characterized by scanning electron microscope, X-ray diffraction, cyclic voltammetry, electrochemical impedance spectroscopy, and galvanostatic cycling tests, respectively. Electrochemical measurements revealed that the TiO₂ electrodes with an optimal thickness of 3 μm, corresponding to 25 printed layers, exhibited the best electrochemical performance, i.e. a large initial capacity of around 290 mAh g⁻¹, stable cycling (above 150 mAh g⁻¹ after 100 cycles, i.e. a capacity retention of ~53%), and high rate performance up to 5C (capacity retention of 58% after 100 cycles). We have thus demonstrated that inkjet printing can be used as a simple and low-cost method to fabricate thin film TiO₂ electrodes for lithium-ion batteries.

4.1 Introduction

As portable electronic devices continue to decrease in size, intensive research efforts have focused on developing thin film batteries (TFBs) in recent years. Due to their reduced thickness that enables fast reaction kinetics, thin film batteries have great potential for applications in RFID tags, wireless sensors, and implantable medical

devices. Current fabrication techniques for thin film electrodes or all-solid-state TFBs mainly include sputtering [1, 2], chemical vapor deposition [3, 4], pulsed laser deposition [5, 6], spin coating [7], and sol-gel methods [8, 9]. However, many of these techniques typically require expensive equipment, high temperatures, and/or post-annealing treatments that can damage the films and the substrate. These obstacles greatly restrict the development of state-of-the-art TFBs.

Inkjet printing is a simple and inexpensive alternative to fabricate thin film electrodes with typical thicknesses on the scale of micrometers [10-12]. It is an additive process in which picoliter-sized droplets of ink are deposited onto a substrate in a desired pattern. By repeating this process multiple times, the thickness of thin films can be precisely controlled. Additionally, the structure of the thin film electrodes can be patterned by following a computer-aided design (CAD). Inkjet printing has many advantages compared to other thin film fabrication techniques, including cost-effectiveness, ease of use, minimal wasted material, and the ability to deposit material in any pattern. It has therefore been used to fabricate thin films for various energy storage and conversion devices, including battery electrodes, supercapacitors, fuel cells, and solar cells [12].

The key to achieving high performance inkjet-printed thin film electrodes is the optimization of the ink's composition and the printing process. The solid contents of the ink must be uniformly dispersed in solution; if the ink is not well-mixed, the particles can agglomerate and cause the printer's nozzles to clog. Additionally, if the solid content of the ink is too low, ideal jetting cannot be achieved due to satellite droplet formation and a high number of printing passes required to deposit sufficient material. Previously, printing processes for various LIB electrode materials have been developed. Tin oxide [13] and lithium titanate [14] anodes and lithium cobalt oxide [15-17] and lithium manganese oxide [18] cathodes have all been fabricated by inkjet printing. In general, the physical properties of the inks in these studies were not optimized and the electrodes did not exhibit high electrochemical performance. It is therefore critical to control the ink's composition to realize high performance inkjet-printed LIB electrodes.

Titanium dioxide (TiO_2) has been considered a promising alternative anode material for lithium-ion batteries (LIBs) due to its low cost, non-toxicity, safe lithiation potential, high rate capability, and excellent cycling stability [19, 20]. In the present study, we report the fabrication of thin film TiO_2 anodes for LIBs by inkjet printing with a conventional desktop inkjet printer. The TiO_2 inks were optimized with different choices of polymer binders to achieve the best stability and jetting properties. When an ideal ink formulation was determined, thin film anodes were printed directly onto the current collector using a household inkjet printer. The electrochemical performance of the thin film electrodes was examined by charge and discharge cycling, rate performance, cyclic voltammetry (CV), and electrochemical impedance spectroscopy (EIS). We also investigated the effect of film thickness on their electrochemical performance in LIBs, and examined their morphology and chemical composition after extended cycling. The high performance of the inkjet-printed TiO_2 anodes demonstrates that inkjet printing is a viable fabrication method for thin film electrodes for LIBs.

4.2 Methods

4.2.1 TiO_2 ink preparation

Inks were prepared by mixing 80 wt. % TiO_2 nanoparticles (21 nm, Sigma-Aldrich), 10 wt. % carbon black (50 nm, GunBai), and 10 wt. % polymer binder in DI-water. The concentration of the solids in water was optimized to achieve a viscosity of 10 mPa·s, the ideal viscosity for inkjet printing [21, 22] (approximately 20 mg/mL). The polymer binders used in this study were poly(3,4-ethylenedioxythiophene)-poly(styrene sulfonate) (PEDOT:PSS), polyvinylpyrrolidone (PVP), and polyvinylidene fluoride (PVDF), all purchased from Sigma-Aldrich. The mixture was then sonicated for at least 3 hours to break up large agglomerates and ensure uniform dispersion prior to printing.

4.2.2 Electrode and coin cell preparation

The ink was transferred into a well-cleaned HP 61 ink cartridge and printed using an HP Deskjet 2540 inkjet printer (Hewlett-Packard). Different numbers of layers (15, 25, or 35) of TiO₂ thin films were printed on copper foil to investigate the effect of the electrode thickness on electrochemical performance. The inkjet-printed films were dried with a compressed air gun between printing layers. After printing, the films were dried in a vacuum oven at 60°C overnight. The printed films were then cut into round disks and assembled into CR-2032 coin cells with lithium metal as the counter electrode and Celgard 2400 separators in an argon-filled glove box. The electrolyte was composed of 1 M LiPF₆ salt dissolved in a solvent of 1:1:1 ratio by volume of ethylene carbonate (EC) : diethyl carbonate (DEC) : ethyl methyl carbonate (EMC), from BASF. The coin cells were stored overnight at room temperature before testing.

4.2.3 Characterization

A field emission scanning electron microscopy (SEM, Hitachi S-4800) was used to observe the microstructure of the printed films. Compositional information was obtained by X-ray diffraction (XRD, Bruker D8 Advance, Cu K α X-ray source) at a grazing incidence angle of 1° and a step size of 0.02° in 2 θ . Galvanostatic charge-discharge measurements were performed on an Arbin BT-2000 Battery Tester between 1.0 and 2.5 V vs. Li/Li⁺. The charge/discharge currents (rates) and capacities were calculated based on the actual mass of active TiO₂ material in the anode, as determined by thermogravimetric analysis (TGA, TA Instruments SDT Q600). Cyclic voltammetry (CV) and electrochemical impedance spectroscopy (EIS) were performed on a multichannel potentiostat 3/Z (VMP3).

4.3 Results and Discussion

4.3.1 Printing process and morphological characterization of the inkjet-printed thin films

Inkjet printing is an effective technique for fabricating uniform electrodes with tight control over thickness. Ink solutions were prepared with TiO₂ nanoparticles as the electrochemically active material, carbon black as the conductive agent, and three different polymer binders, mixed in water. The as-prepared inks with PVDF, PVP, and PEDOT:PSS binders are shown in Figure 4.1a-c. As seen, inks with PVDF and PVP binders could not be well-mixed; even after 5h of sonicating the carbon black separated from solution, ultimately resulting in clogging of the printer's nozzles. On the other hand, when using PEDOT:PSS the ink was well-dispersed and readily formed uniform films on copper foil. PEDOT:PSS has previously been shown to be an effective binder material for lithium-ion batteries [23, 24] and serves two purposes here: (1) it enables ideal jetting, as it is a commonly used material for inkjet printing [25-27] and therefore commercial ink formulations have been specifically designed with optimized jetting properties; and (2) PEDOT:PSS is electronically conductive and forms a continuous conductive network throughout the electrode, ensuring rapid electron transport to and from the insulating TiO₂ nanoparticles.

The optical image in Figure 4.1d demonstrates the high degree of uniformity of the inkjet-printed TiO₂ films with PEDOT:PSS binder. The SEM image in Figure 4.1e shows the surface morphology of an as-printed TiO₂ thin film electrode before cycling. It can be seen that the PEDOT:PSS binder formed a continuous network in which the TiO₂ nanoparticles were embedded, with many small pores that resulted in a large electrode-electrolyte contact area. After charging and discharging for 100 cycles at 0.1C (Figure 4.1f), the structure of the TiO₂ thin film electrode was well-maintained and no visible physical degradation was observed.

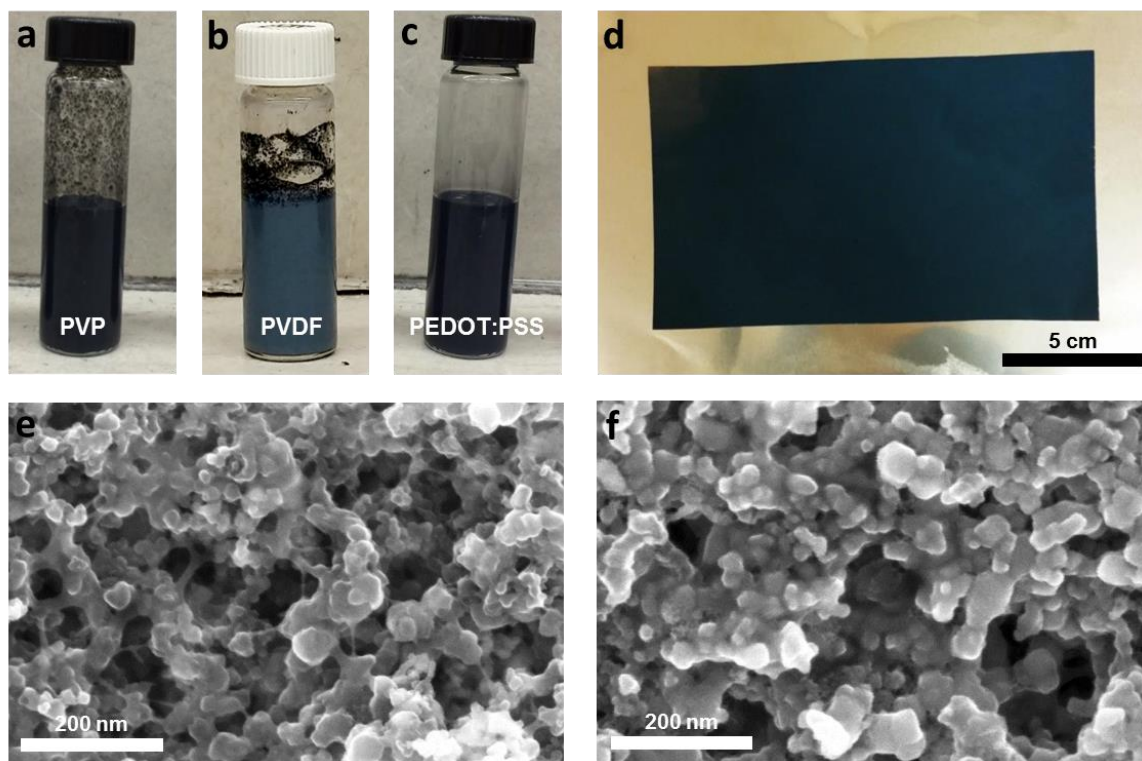


Figure 4.1. Ink solutions prepared with three different polymer binders: (a) PVP, (b) PVDF, and (c) PEDOT:PSS. (d) Optical image of the TiO₂ nanoparticle solution with PEDOT:PSS binder inkjet-printed on copper foil with 25 layers. SEM images of the printed film (e) before and (f) after cycling.

Figure 4.2 shows cross-sectional SEM images of TiO₂ thin films printed with 15, 25, and 35 layers (referred to as TiO₂-15, TiO₂-25, and TiO₂-35, respectively), after post-pressing. The thicknesses of the films were measured to be 1.89, 3.02, and 4.40 μm , respectively. This corresponds to an average thickness of a single printed layer of approximately 125 nm. Therefore it is straightforward to fabricate thin film electrodes with sub-micron precision simply by repeating the inkjet printing process until the desired thickness is achieved.

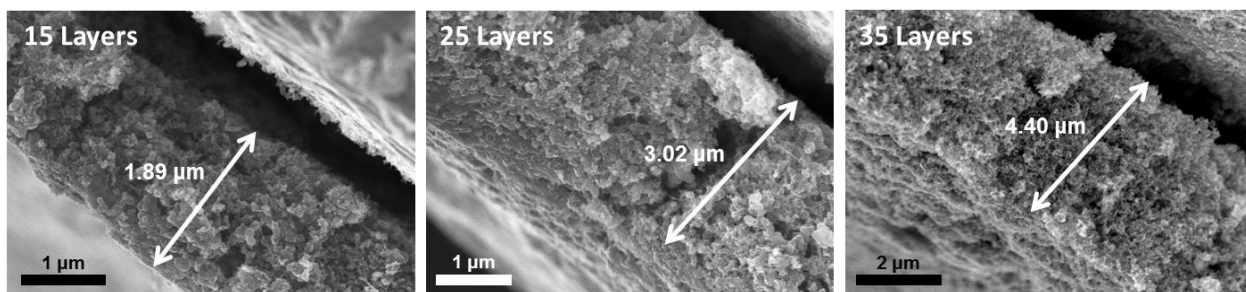


Figure 4.2. Cross-sectional SEM images of TiO₂ films printed with different number of layers.

4.3.2 Structural and compositional characterization of the inkjet-printed thin films

Figure 4.3 shows the XRD patterns of inkjet-printed anodes before and after cycling, along with the TiO₂ powder used. TiO₂ has four polymorphs that have been reported for lithium storage: rutile, anatase, brookite, and bronze (TiO₂-B) [19]. In this study, a commercial TiO₂ nanopowder was directly used. Diffraction peaks at 25.3°, 37.0°, 37.8°, 38.6°, and 48.0° in its XRD pattern correspond to the (101), (103), (004), (112), and (200) crystal faces of anatase TiO₂ respectively (COD 9009086), and peaks at 27.4°, 36.1°, 39.2°, 41.2°, and 44.0° correspond to the (110), (101), (200), (111), and (210) crystal faces of rutile TiO₂, respectively (COD 9004141). The XRD pattern of the printed film well-matched the powder, indicating that a mixture of anatase and rutile TiO₂ coexists in the printed electrode. In addition, the fact that the XRD pattern of the inkjet-printed film before cycling closely matches that of the TiO₂ powder demonstrates that the TiO₂ maintains its crystal structure during the dispersion and printing processes. Because the film is very thin, peaks from the copper substrate underneath are clearly visible at 42.7° and 43.4°, marked with asterisks. Interestingly, after charging and discharging for 100 cycles, diffraction peaks from the initial rutile TiO₂ phase disappeared in the XRD pattern, while those belonging to the anatase phase were still clearly visible. This phenomenon is consistent with what has been observed in a previous study and is believed to be due to the transformation of rutile TiO₂ into an amorphous Li_xTiO₂ phase [28].

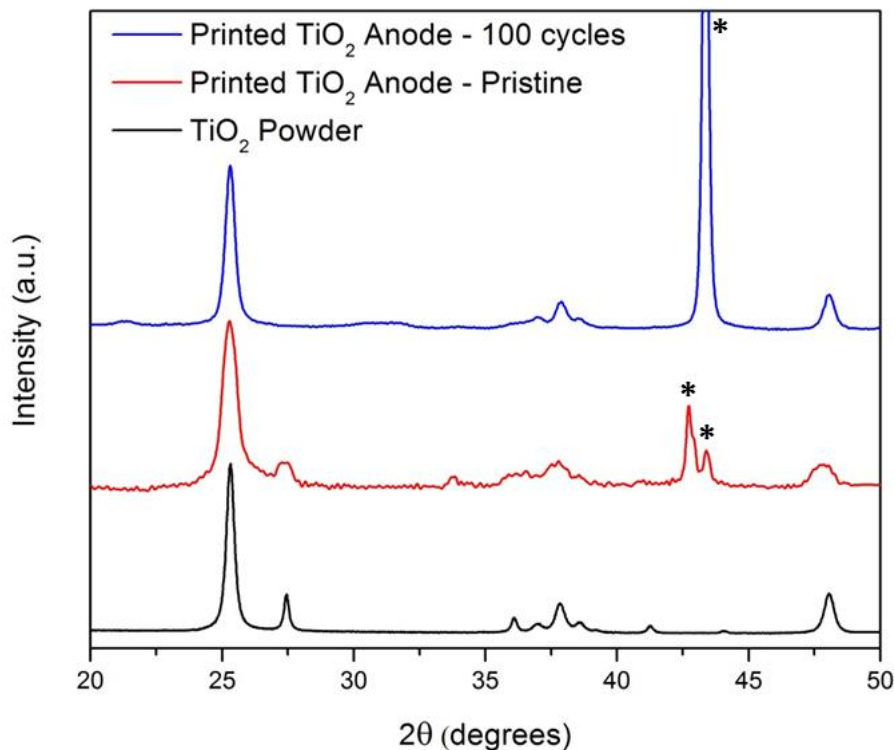


Figure 4.3. XRD patterns of inkjet-printed TiO₂ films before and after cycling. A reference of TiO₂ powder is shown for comparison. Peaks marked with an asterisk (*) are from the underlying copper foil substrate.

It should be noted that the mass percentage of TiO₂ in the printed film may differ from that in the prepared ink solution due to non-ideal jetting conditions or from particles becoming trapped inside the cartridge sponge or nozzles. To address this difference and determine an accurate value for the mass of TiO₂ in the inkjet-printed electrodes, TGA was performed on a printed thin film electrode that was scraped off of the copper substrate (Figure 4.4). Considering the fact that TiO₂ is stable in a temperature range of 25°C to 900°C, as confirmed by TGA of pristine TiO₂ powder (the weight loss below 100°C is due to the removal of adsorbed water), all observed mass loss of the printed thin film can be attributed to the removal of carbon black and PEDOT:PSS polymer binder. Both carbon black and PEDOT:PSS were completely removed, with no remaining mass above 825°C. We therefore used the measured residual mass of the printed TiO₂ anode (76%) as the mass percentage of TiO₂ in the anode when calculating the charge/discharge rates and capacities during electrochemical testing.

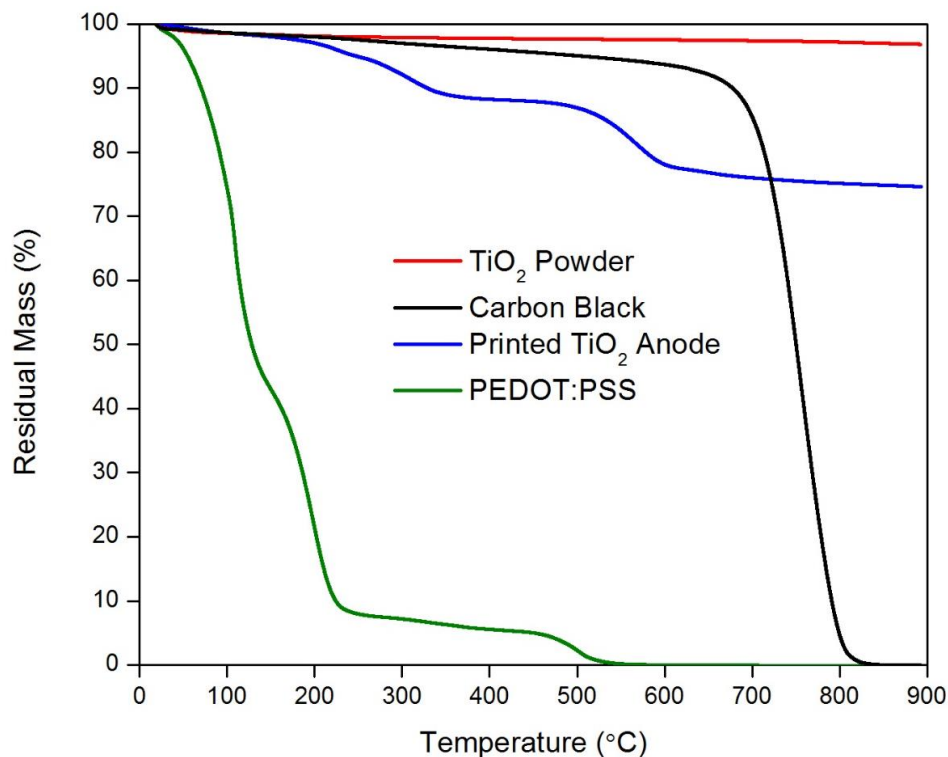


Figure 4.4. TGA curves of an inkjet-printed TiO₂ anode and each of its components individually.

4.3.3 Electrochemical characterization

The lithiation and delithiation processes of titanium dioxide can be expressed by the following insertion/extraction reaction:



The maximum insertion coefficients, x , for bulk anatase and rutile TiO₂ are typically 0.5 and 0.1, respectively [29], corresponding to theoretical capacities of 167.5 mAh g⁻¹ and 33.5 mAh g⁻¹ (with respect to the mass of TiO₂). Nanoscale TiO₂ is reported to be able to be further lithiated up to $x = 0.85$ for anatase and $x = 0.75$ for rutile [29], corresponding to capacities of 285 mAh g⁻¹ and 251 mAh g⁻¹, respectively. This improvement in the electrochemical performance of nanosized TiO₂ is a result of shorter electron and lithium ion diffusion lengths, as well as a larger electrode/electrolyte interfacial area [19]. Figure

4.5a shows the cycling performance of inkjet-printed TiO₂-15, TiO₂-25, and TiO₂-35 anodes with different thicknesses at a current rate of 0.1C (1C = 167 mA g⁻¹). The first lithium insertion capacities were 285 to 300 mAh g⁻¹ for thin film electrodes with different thicknesses, equivalent to lithium insertion coefficients of 0.85 to 0.90. Some minor additional lithium storage by the conductive carbon black and PEDOT:PSS binder may have contributed to these elevated discharge capacities. All cells exhibited irreversible capacity loss during the first few cycles, originating from irreversible lithium insertion. This may also be due to the irreversible phase change of the rutile phase, as observed with XRD. First cycle Coulombic efficiencies of all the TiO₂ electrodes were below 75%; however, after the five cycles their Coulombic efficiencies are above 95%. The electrode printed with 25 layers, corresponding to a thickness of approximately 3 μm, exhibited the highest reversible capacity over 100 cycles. Electrodes with 15 and 35 layers, 1.9 and 4.4 μm thick, respectively, had more rapid capacity fading over 100 cycles. The poorer cycling performance of the thicker anode can be attributed to the cell's higher internal resistance, as measured by EIS (Figure 4.5b). Additionally, the discharge capacity of thicker films is limited by the diffusion and penetration of lithium ions and tends to decrease as the electrode thickness increases [30]. The decreased performance of the thinner anode may be due to non-uniformities in the film created during the inkjet-printing process, such as pin-holes and isolated islands of deposited electroactive material. With more printed layers these defects are filled in, resulting in an optimized thickness of 3 μm for inkjet-printed TiO₂ anodes.

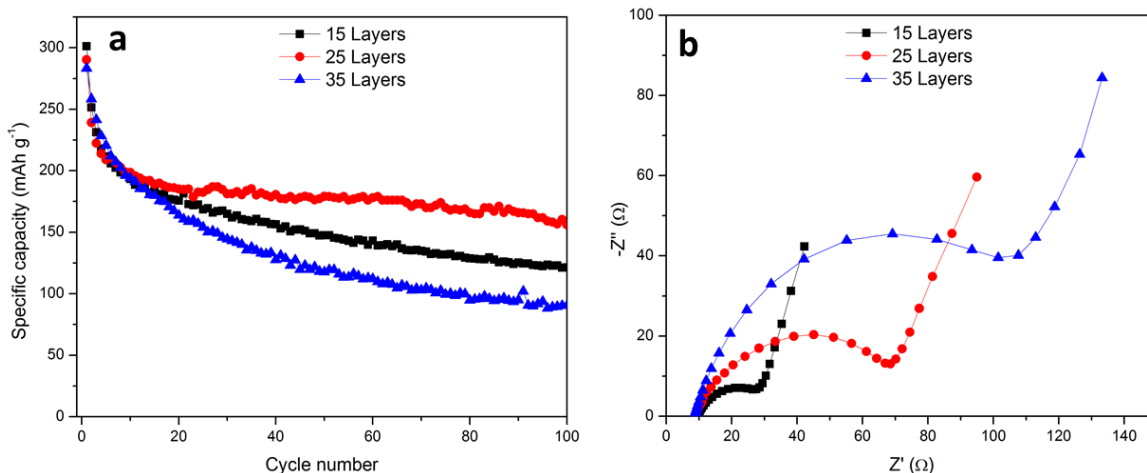


Figure 4.5. (a) Galvanostatic cycling at 0.1C and (b) EIS measurements of three inkjet-printed TiO₂ anodes with different thicknesses, controlled by the number of printed layers. 15 layers = 1.9 μm, 25 layers = 3.0 μm, and 35 layers = 4.4 μm.

Figure 4.6 shows the rate capability of an inkjet-printed TiO₂-25 anode with the optimal thickness. Its reversible specific discharge capacity varied from 180 mAh g⁻¹ at 0.1C to 37 mAh g⁻¹ at 5C (Figure 4.6a). After cycling at elevated rates, the capacity returned to 165 mAh g⁻¹ at 0.1C, corresponding to irreversible capacity loss of approximately 8%. The length of the discharge plateau region at approximately 1.7 V, seen in the voltage profiles (Figure 4.6b), clearly decreased as the cycling rate increased. This plateau corresponds to the formation of a bi-phase region where Li-rich phases coexist with Li-poor anatase and rutile TiO₂, and is where the majority of the anode's capacity is derived [31]. The plateau was relatively flat at low cycling rates of 0.1 and 0.2C, but at the higher rates above 0.5C no obvious plateau was observed in the discharge profiles, due to increasing polarization under high current densities brought around by sluggish Li-ion diffusion and intercalation kinetics. Instead, most of the reversible lithium storage at high rates was surface-confined charge storage that occurs at particle interfaces, indicated by the sloping region below 1.7 V [32]. This ultimately led to the decreased cycling capacity observed at 1C and 5C (Figure 4.6c). However, the Coulombic efficiency of the 25 printed-layer electrode was above 99.2% at 1C and 99.5% at 5C after the first few cycles, compared to 98% at 0.1C, demonstrating stable cycling performance at elevated rates.

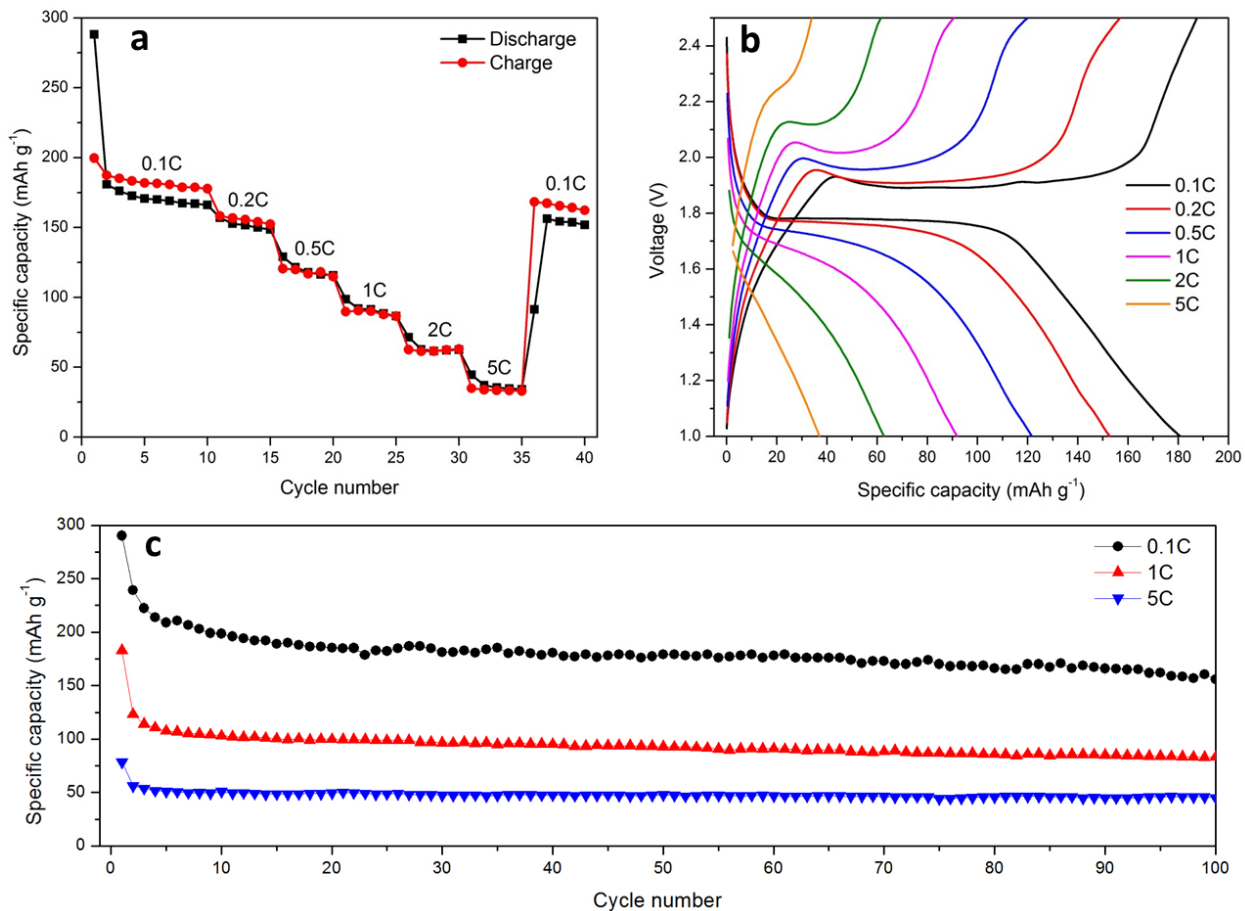


Figure 4.6. (a) Rate capability of a TiO₂-25 anode and (b) the corresponding 2nd-cycle charge and discharge voltage profiles at each different current rate. (c) Long-term cycling performance of TiO₂-25 anodes at varying charge/discharge rates.

At high current rates, the specific capacity was limited by the diffusion of Li ions into and out of the TiO₂ nanoparticles. To measure the diffusion coefficient in these inkjet-printed anodes, CV curves at varying scan rates were taken, as shown in Figure 4.7a. A linear relationship exists between the peak current and square root of the applied voltage scan rate (Figure 4.7b), confirming that the reaction kinetics are diffusion-limited [33, 34]. From this plot, the apparent Li-ion diffusion coefficient, D , can be calculated using equation 4.2 [35]:

$$i_p = 0.4958nFAC \left(\frac{F\alpha n_\alpha Dv}{RT} \right)^{1/2} \quad (4.2)$$

where i_p is the peak current, n and n_a are the number of electrons involved in the overall and rate-determining processes (here, both 1), F is the Faraday constant, A is the surface area of the electrode (estimated using the method outlined in [36]), C is the concentration of lithium ions in $\text{Li}_{0.5}\text{TiO}_2$ ($0.024 \text{ mol cm}^{-3}$ [37]), α is the transfer coefficient (0.5 for anatase TiO_2 [34]), ν is the scan rate, R is the gas constant, and T is the absolute temperature (here, 298 K). Apparent diffusion coefficients for lithium-ion intercalation and extraction are calculated as 1.1×10^{-15} and $5.6 \times 10^{-15} \text{ cm}^2 \text{ s}^{-1}$, respectively, which are in good agreement with other studies [33, 34, 38, 39]. The higher rate of Li-ion extraction compared to insertion into the TiO_2 host can be attributed to the faster Li-ion diffusion rates observed in TiO_2 compared to lithiated TiO_2 ($\text{Li}_{0.5}\text{TiO}_2$), due to the greater number of unoccupied octahedral sites available for Li ions in anatase TiO_2 [33].

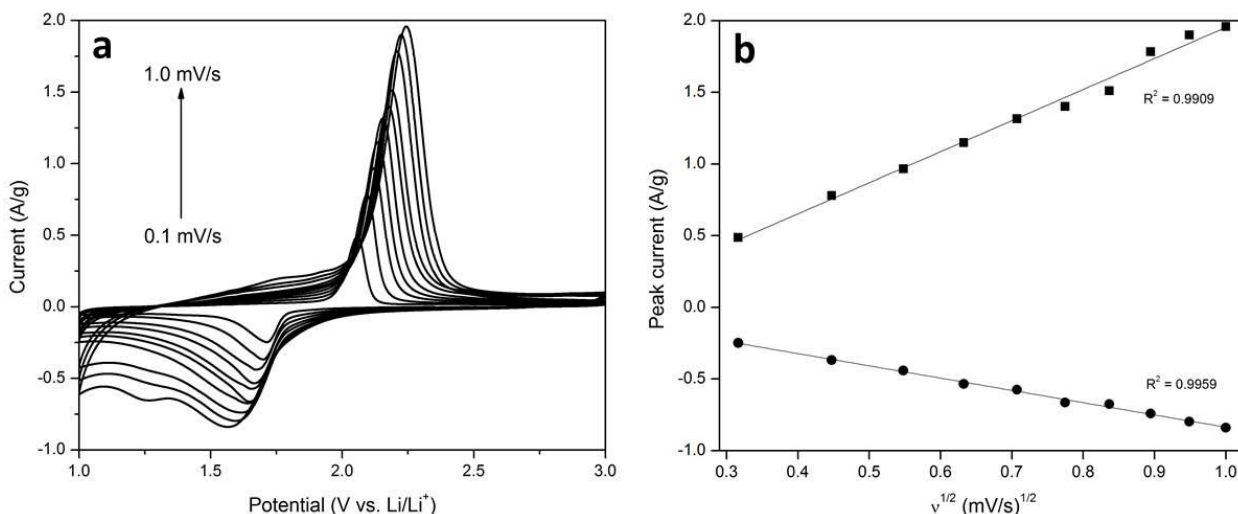


Figure 4.7. (a) CV scans of inkjet-printed TiO_2 anodes at varying scan rates. (b) Plot of peak current vs. square root of the scan rate for both anodic (top) and cathodic (bottom) peaks.

Herein, an inkjet-printing technology was applied to fabricate TiO_2 thin film electrodes. The parameters for inkjet printing have been optimized to achieve the highest performance of TiO_2 thin film electrodes. The cycling performance of these anodes in LIBs is similar to other reported values for anatase and rutile TiO_2 electrodes prepared by conventional methods [32, 40, 41]. It should be noted that commercial TiO_2 nano-powder has been used in this study to give a universal demonstration of the ability and potential

of inkjet printing technology in the application of LIBs. Further improved performance of the printed TiO₂ electrodes can be expected by replacing it with battery-grade or tailored nanostructured TiO₂ powders. Accordingly, inkjet printing can therefore be a viable fabrication method for thin film electrodes. It may find a niche in designing various patterned electrodes for applications in which irregularly-shaped electrodes are needed, such as terraced batteries or foldable devices. In addition, further work on applying this technique to cathode materials and polymer electrolytes is ongoing in our group, in the aim of fabricating a fully inkjet-printed cell.

4.4 Conclusions

In summary, we have fabricated thin film titanium dioxide anodes for LIBs by inkjet printing and optimized the process in terms of selection of the polymer binder used and control of thickness. The thickness of the electrode can be precisely controlled by varying the number of printed layers, with each layer adding approximately 125 nm to the film. By tuning the thickness of the anode it was possible to optimize the electrochemical performance, with electrodes 3 μm thick exhibiting the highest reversible capacity, above 150 mAh g⁻¹ for 100 cycles. In terms of rate performance, these inkjet-printed TiO₂ anodes also demonstrated excellent capacity retention after 100 cycles up to 5C. Overall, inkjet printing has been used as a feasible, simple, and inexpensive thin film electrode fabrication technique and it is expected that inkjet printing will be further applied to various types of electrode materials in the future.

Acknowledgements

This work was supported by the Natural Sciences and Engineering Research Council of Canada (NSERC), Canada Research Chair (CRC) Program, Canada Foundation for Innovation (CFI), Ontario Research Fund (ORF), and University of Western Ontario. Stephen Lawes also acknowledges the Province of Ontario and the University of Western Ontario for the Queen Elizabeth II Graduate Scholarship in Science and Technology.

References

- [1] W.-S. Kim, "Characteristics of LiCoO₂ thin film cathodes according to the annealing ambient for the post-annealing process," *Journal of Power Sources*, vol. 134, pp. 103-109, 2004.
- [2] S.-J. Kim, H.-C. Park, M.-C. Kim, D.-M. Kim, Y.-W. Lee, and K.-W. Park, "Sputtered amorphous thin film nanocomposites as an anode for lithium-ion batteries," *Journal of Power Sources*, vol. 273, pp. 707-715, 2015.
- [3] H. Jung, M. Park, S. H. Han, H. Lim, and S.-K. Joo, "Amorphous silicon thin-film negative electrode prepared by low pressure chemical vapor deposition for lithium-ion batteries," *Solid State Communications*, vol. 125, pp. 387-390, 2003.
- [4] A. Jena, N. Munichandraiah, and S. A. Shivashankar, "Metal-organic chemical vapor-deposited cobalt oxide films as negative electrodes for thin film Li-ion battery," *Journal of Power Sources*, vol. 277, pp. 198-204, 2015.
- [5] J. D. Perkins, C. S. Bahn, J. M. McGraw, P. A. Parilla, and D. S. Ginley, "Pulsed Laser Deposition and Characterization of Crystalline Lithium Cobalt Dioxide (LiCoO₂) Thin Films," *Journal of the Electrochemical Society*, vol. 148, pp. A1302-A1312, 2001.
- [6] D. Fujimoto, N. Kuwata, Y. Matsuda, J. Kawamura, and F. Kang, "Fabrication of solid-state thin-film batteries using LiMnPO₄ thin films deposited by pulsed laser deposition," *Thin Solid Films*, vol. 579, pp. 81-88, 2015.
- [7] J. P. Maranchi, A. F. Hepp, and P. N. Kumta, "LiCoO₂ and SnO₂ thin film electrodes for lithium-ion battery applications," *Materials Science and Engineering: B*, vol. 116, pp. 327-340, 2005.
- [8] Y. H. Rho and K. Kanamura, "Preparation of Li_{4/3}Ti_{5/3}O₄ Thin Film Electrodes by a PVP Sol-Gel Coating Method and Their Electrochemical Properties," *Journal of the Electrochemical Society*, vol. 151, pp. A106-A110, 2004.
- [9] T. Kwon, T. Ohnishi, K. Mitsuishi, T. C. Ozawa, and K. Takada, "Synthesis of LiCoO₂ epitaxial thin films using a sol-gel method," *Journal of Power Sources*, vol. 274, pp. 417-423, 2015.
- [10] G. Cummins and M. P. Y. Desmulliez, "Inkjet printing of conductive materials: a review," *Circuit World*, vol. 38, pp. 193-213, 2012.
- [11] B. Derby, "Inkjet Printing of Functional and Structural Materials: Fluid Property Requirements, Feature Stability, and Resolution," *Annual Review of Materials Research*, vol. 40, pp. 395-414, 2010.

- [12] S. Lawes, A. Riese, Q. Sun, N. Cheng, and X. Sun, "Printing nanostructured carbon for energy storage and conversion applications," *Carbon*, vol. 92, pp. 150-176, 2015.
- [13] Y. Zhao, Q. Zhou, L. Liu, J. Xu, M. Yan, and Z. Jiang, "A novel and facile route of ink-jet printing to thin film SnO₂ anode for rechargeable lithium ion batteries," *Electrochimica Acta*, vol. 51, pp. 2639-2645, 2006.
- [14] Y. Zhao, G. Liu, L. Liu, and Z. Jiang, "High-performance thin-film Li₄Ti₅O₁₂ electrodes fabricated by using ink-jet printing technique and their electrochemical properties," *Journal of Solid State Electrochemistry*, vol. 13, pp. 705-711, 2008.
- [15] Y. M. Zhao, J. Xu, L. Liu, J. Yang, and Z. Y. Jiang, "Thin Film LiCoO₂ Cathode Prepared by Using Ink-jet Printing Technique and Its Electrochemical Properties," *Chemical Journal of Chinese Universities*, vol. 28, pp. 1122-1125, 2007.
- [16] J. Huang, J. Yang, W. Li, W. Cai, and Z. Jiang, "Electrochemical properties of LiCoO₂ thin film electrode prepared by ink-jet printing technique," *Thin Solid Films*, vol. 516, pp. 3314-3319, 2008.
- [17] J.-H. Lee, S.-B. Wee, M.-S. Kwon, H.-H. Kim, J.-M. Choi, M. S. Song, *et al.*, "Strategic dispersion of carbon black and its application to ink-jet-printed lithium cobalt oxide electrodes for lithium ion batteries," *Journal of Power Sources*, vol. 196, pp. 6449-6455, 2011.
- [18] J. J. Huang and Z. Y. Jiang, "Electrochemical Performance of LiMn₂O₄ Thin Film Electrode Fabricated by Ink-Jet Printing Technique," *Acta Physico-Chimica Sinica*, vol. 24, pp. 1563-1567, 2008.
- [19] Z. Yang, D. Choi, S. Kerisit, K. M. Rosso, D. Wang, J. Zhang, *et al.*, "Nanostructures and lithium electrochemical reactivity of lithium titanites and titanium oxides: A review," *Journal of Power Sources*, vol. 192, pp. 588-598, 2009.
- [20] T. Froschl, U. Hormann, P. Kubiak, G. Kucerova, M. Pfanzelt, C. K. Weiss, *et al.*, "High surface area crystalline titanium dioxide: potential and limits in electrochemical energy storage and catalysis," *Chemical Society Reviews*, vol. 41, pp. 5313-5360, 2012.
- [21] J. Li, F. Ye, S. Vaziri, M. Muhammed, M. C. Lemme, and M. Östling, "Efficient Inkjet Printing of Graphene," *Advanced Materials*, vol. 25, pp. 3985-3992, 2013.
- [22] X. Wang, W. W. Carr, D. G. Bucknall, and J. F. Morris, "High-shear-rate capillary viscometer for inkjet inks," *Review of Scientific Instruments*, vol. 81, p. 065106, 2010.

- [23] P. R. Das, L. Komsiyiska, O. Osters, and G. Wittstock, "PEDOT: PSS as a Functional Binder for Cathodes in Lithium Ion Batteries," *Journal of the Electrochemical Society*, vol. 162, pp. A674-A678, 2015.
- [24] D. Shao, H. Zhong, and L. Zhang, "Water-Soluble Conductive Composite Binder Containing PEDOT:PSS as Conduction Promoting Agent for Si Anode of Lithium-Ion Batteries," *ChemElectroChem*, vol. 1, pp. 1679-1687, 2014.
- [25] S. H. Eom, S. Senthilarasu, P. Uthirakumar, S. C. Yoon, J. Lim, C. Lee, *et al.*, "Polymer solar cells based on inkjet-printed PEDOT:PSS layer," *Organic Electronics*, vol. 10, pp. 536-542, 2009.
- [26] K. X. Steirer, J. J. Berry, M. O. Reese, M. F. A. M. van Hest, A. Miedaner, M. W. Liberatore, *et al.*, "Ultrasonically sprayed and inkjet printed thin film electrodes for organic solar cells," *Thin Solid Films*, vol. 517, pp. 2781-2786, 2009.
- [27] Y. Galagan, E. W. C. Coenen, S. Sabik, H. H. Gorter, M. Barink, S. C. Veenstra, *et al.*, "Evaluation of ink-jet printed current collecting grids and busbars for ITO-free organic solar cells," *Solar Energy Materials and Solar Cells*, vol. 104, pp. 32-38, 2012.
- [28] D. Wang, D. Choi, Z. Yang, V. V. Viswanathan, Z. Nie, C. Wang, *et al.*, "Synthesis and Li-Ion Insertion Properties of Highly Crystalline Mesoporous Rutile TiO₂," *Chemistry of Materials*, vol. 20, pp. 3435-3442, 2008.
- [29] A. G. Dylla, G. Henkelman, and K. J. Stevenson, "Lithium Insertion in Nanostructured TiO₂(B) Architectures," *Accounts of Chemical Research*, vol. 46, pp. 1104-1112, 2013.
- [30] N. J. Dudney and Y.-I. Jang, "Analysis of thin-film lithium batteries with cathodes of 50 nm to 4 μ m thick LiCoO₂," *Journal of Power Sources*, vol. 119-121, pp. 300-304, 2003.
- [31] Y.-G. Guo, Y.-S. Hu, and J. Maier, "Synthesis of hierarchically mesoporous anatase spheres and their application in lithium batteries," *Chemical Communications*, pp. 2783-2785, 2006.
- [32] J.-Y. Shin, D. Samuelis, and J. Maier, "Sustained Lithium-Storage Performance of Hierarchical, Nanoporous Anatase TiO₂ at High Rates: Emphasis on Interfacial Storage Phenomena," *Advanced Functional Materials*, vol. 21, pp. 3464-3472, 2011.
- [33] R. van de Krol, A. Goossens, and J. Schoonman, "Spatial Extent of Lithium Intercalation in Anatase TiO₂," *The Journal of Physical Chemistry B*, vol. 103, pp. 7151-7159, 1999.

- [34] H. Lindström, S. Södergren, A. Solbrand, H. Rensmo, J. Hjelm, A. Hagfeldt, *et al.*, "Li⁺ Ion Insertion in TiO₂ (Anatase). 2. Voltammetry on Nanoporous Films," *The Journal of Physical Chemistry B*, vol. 101, pp. 7717-7722, 1997.
- [35] A. J. Bard and L. R. Faulkner, *Electrochemical Methods: Fundamentals and Applications*. New York: John Wiley & Sons, 2001.
- [36] H. Lindström, S. Södergren, A. Solbrand, H. Rensmo, J. Hjelm, A. Hagfeldt, *et al.*, "Li⁺ Ion Insertion in TiO₂ (Anatase). 1. Chronoamperometry on CVD Films and Nanoporous Films," *The Journal of Physical Chemistry B*, vol. 101, pp. 7710-7716, 1997.
- [37] L. Kavan, M. Grätzel, S. E. Gilbert, C. Klemenz, and H. J. Scheel, "Electrochemical and Photoelectrochemical Investigation of Single-Crystal Anatase," *Journal of the American Chemical Society*, vol. 118, pp. 6716-6723, 1996.
- [38] A. G. Dylla, J. A. Lee, and K. J. Stevenson, "Influence of Mesoporosity on Lithium-Ion Storage Capacity and Rate Performance of Nanostructured TiO₂(B)," *Langmuir*, vol. 28, pp. 2897-2903, 2012.
- [39] J. Wang, J. Polleux, J. Lim, and B. Dunn, "Pseudocapacitive Contributions to Electrochemical Energy Storage in TiO₂ (Anatase) Nanoparticles," *The Journal of Physical Chemistry C*, vol. 111, pp. 14925-14931, 2007.
- [40] D. Wang, D. Choi, J. Li, Z. Yang, Z. Nie, R. Kou, *et al.*, "Self-Assembled TiO₂-Graphene Hybrid Nanostructures for Enhanced Li-Ion Insertion," *ACS Nano*, vol. 3, pp. 907-914, 2009.
- [41] Y. S. Hu, L. Kienle, Y. G. Guo, and J. Maier, "High Lithium Electroactivity of Nanometer-Sized Rutile TiO₂," *Advanced Materials*, vol. 18, pp. 1421-1426, 2006.

Chapter 5

5 Conclusions and Future Work

5.1 Conclusions

Two studies were conducted for this thesis, both developing an inkjet printing fabrication process for thin film lithium-ion battery electrodes. Next-generation anode materials, silicon and titanium dioxide, were inkjet printed for TFBs for the first time. The application of these thin film electrodes in LIBs was demonstrated and further experiments were performed to enhance their cycling performance and to investigate the underlying mechanisms of these improvements.

Both studies followed the same basic plan: first develop nanoparticle inks with ideal jetting characteristics, print them onto copper foil current collector, and then characterize the physical, chemical, and electrochemical properties of these anodes. This process involved determining the relationships between printing parameters and electrochemical performance of the thin film electrodes. The effects of the polymer binder, number of printed layers (thickness), and ink concentration on both inkjet printing quality and cycling of LIBs were investigated.

In the first study, silicon nanoparticle anodes were fabricated by inkjet printing. The ink's physical properties were optimized to achieve excellent jetting conditions. The relationship between the concentration of solid particles in the ink, the number of printed layers, and the jetting performance was determined to ensure good printing properties. Once it was possible to repeatedly achieve uniform films, four polymer binders were investigated for their effect on the electrochemical performance of these printed anodes. The conductive polymer PEDOT:PSS gave the best results; in cycling tests, inkjet-printed silicon anodes with PEDOT:PSS binder outperformed those with conventionally-used binders and those fabricated by the conventional doctor-blading technique. To determine the reason for this, a number of *ex-situ* characterization techniques were used to study the morphological and chemical structure of the anodes during electrochemical cycling. A mechanism was proposed, which attributed the improved performance to the ability of

PEDOT:PSS to accommodate the large volume expansion of silicon during lithiation and maintain an electrically conductive network. This study demonstrated the efficacy of using inkjet printing for silicon anode fabrication, as well as furthered our understanding of the role of the polymer binder in LIB performance.

In the second study, titanium dioxide anodes were fabricated using the same inkjet printing process. Variations in the ink formulation were made to ensure proper jetting and good electrochemical performance. Specifically, a higher loading content of active material was possible for the TiO₂ inks (80%) compared to the silicon inks (40%). This was due to the smaller size of the TiO₂ nanoparticles (21 nm) compared to silicon (50 nm), which resulted in shorter electron and lithium-ion diffusion lengths. This meant that less conductive material was required to ensure sufficient electrical conductivity throughout the electrode. Similarly, the optimal thickness of the TiO₂ anodes (3 μm) was greater than that of the silicon anodes (1 μm). The inkjet-printed TiO₂ anodes exhibited excellent cycling stability, even at high current densities. In particular, the performance at high rates was investigated and it was determined that diffusion-limited kinetics accounted for the decrease in capacity as the charge-discharge rate increased.

Overall, this work demonstrates that inkjet printing is a viable fabrication method for thin film LIB electrodes. Inkjet printing can be used as a simple, inexpensive, and scalable production technique for TFBs. Additionally, precise control over thickness, the ability to deposit patterns, and minimal wasted material are all advantages of using inkjet printing for TFB electrode fabrication. While the work here demonstrated a proof-of-concept for the efficacy of inkjet printing for next-generation LIB anode materials, further studies should be conducted to further improve the printing speed and reliability of this technique, as well as fabricate other battery components (cathode and electrolyte) for full cell assembly.

5.2 Recommendations for Future Work

Fabrication of battery components by printing is still a relatively new concept and more work must be done to prove its commercial efficacy. Printing techniques are more suited for fabricating smaller batteries for consumer electronics; however they may be feasible for manufacturing larger cells for electric vehicles by using a scaled-up printer or roll-to-roll technology. On the research side, additional studies should be performed to develop inkjet printing fabrication methods for LIBs. To directly continue the work of this thesis, a few projects of varying complexity and timescales are suggested here.

First, as a natural progression of the work presented here, next-generation cathode materials for LIBs should be inkjet printed. A number of studies have already developed inkjet printing techniques for fabricating LCO cathodes [1-3], but none have used high-capacity lithium iron phosphate (LFP) or nickel manganese cobalt oxide (NMC). One potential challenge may be synthesizing these cathode materials into particles small enough for inkjet printing (less than a few microns) to prevent clogging of the nozzles. However, with ball milling or other techniques it should be possible. This would be a relatively short project, as ink development would be straightforward following the work presented in this thesis.

A more interesting project would be the development of a printable electrolyte. To date, no LIB electrolyte has been deposited by inkjet printing. It would require the development of a low-viscosity electrolyte solution that is stable in air, or operating an inkjet printer inside a glovebox. Gel polymer electrolytes may be a promising choice, as they can be stable in air and are initially liquids with sufficiently low viscosity for inkjet printing before solidifying [4]. This means that they could be printed as a liquid and then solidified by evaporation or other post-treatment (e.g. UV light).

Moreover, the combination of the above two projects plus the work in this thesis would be high impact work: a fully inkjet-printed LIB. Ideally, a fully integrated process would be developed, in which the anode, electrolyte, and cathode are sequentially printed on top of one another. An insulating polymer could also be printed for the packaging of the cell.

It should be noted that the application of inkjet printing technology to other advanced battery systems, including lithium-sulfur, sodium-ion, and metal-air batteries, has not yet been demonstrated in any reported study so far. However, the printing techniques discussed here may also be suitable for these batteries. For example, carbon encapsulated sulfur (C-S) composite materials are the most commonly used electrodes for Li-S batteries in the state-of-the-art. These microporous carbons used as the sulfur host have a similar morphology as the carbon blacks commonly used in black inks for inkjet printing. It can therefore be expected that such materials can be easily adopted for printed electrodes. Additionally, porous carbon cathodes are indispensable in metal-air cells. Printing technology can not only ensure the large-scale uniform fabrication of these air cathodes, but can also be used to fabricate 3D-structured air electrodes to efficiently accommodate the discharge products.

The true power of battery printing technology will be realized with 3D printing techniques in the future, in which electrodes can be readily patterned into micro- and nano-structures. Interdigitated electrodes can be used to minimize the ionic path length and achieve high charge/discharge rates, as well as increase the volumetric energy density by using the limited space within the cell [5]. And 3D printers are able to extrude much higher viscosity fluids than inkjet printers, making it easier to print polymer electrolytes and fabricate fully-printed batteries. In brief, the potential of printing technology for batteries is still far from being fully realized.

References

- [1] Y. M. Zhao, J. Xu, L. Liu, J. Yang, and Z. Y. Jiang, "Thin Film LiCoO₂ Cathode Prepared by Using Ink-jet Printing Technique and Its Electrochemical Properties," *Chemical Journal of Chinese Universities*, vol. 28, pp. 1122-1125, 2007.
- [2] J. Huang, J. Yang, W. Li, W. Cai, and Z. Jiang, "Electrochemical properties of LiCoO₂ thin film electrode prepared by ink-jet printing technique," *Thin Solid Films*, vol. 516, pp. 3314-3319, 2008.
- [3] J.-H. Lee, S.-B. Wee, M.-S. Kwon, H.-H. Kim, J.-M. Choi, M. S. Song, H. B. Park, H. Kim, and U. Paik, "Strategic dispersion of carbon black and its

application to ink-jet-printed lithium cobalt oxide electrodes for lithium ion batteries," *Journal of Power Sources*, vol. 196, pp. 6449-6455, 2011.

- [4] J. Y. Song, Y. Y. Wang, and C. C. Wan, "Review of gel-type polymer electrolytes for lithium-ion batteries," *Journal of Power Sources*, vol. 77, pp. 183-197, 1999.
- [5] K. Sun, T. S. Wei, B. Y. Ahn, J. Y. Seo, S. J. Dillon, and J. A. Lewis, "3D printing of interdigitated Li-ion microbattery architectures," *Advanced Materials*, vol. 25, pp. 4539-43, 2013.

Curriculum Vitae

Name: Stephen Lawes

Post-secondary Education and Degrees: University of Waterloo
Waterloo, Ontario, Canada
2008-2013 B.A.Sc.

The University of Western Ontario
London, Ontario, Canada
2014-2015 M.E.Sc.

Honours and Awards: OGS Queen Elizabeth II Graduate Scholarship in Science and Technology
2014

NSERC Canadian Graduate Scholarship
Masters Level
2015

Related Work Experience Teaching Assistant
The University of Western Ontario
2014-2015

Publications:

Lawes S, Riese A, Sun Q, Cheng N, and Sun X. Printing Nanostructured Carbon for Energy Storage and Conversion Applications. Carbon, 2015.

Lawes S, Sun Q, and Sun X. Printing Graphene and Carbon Nanotubes for Energy Storage and Conversion Applications. Handbook of Carbon Nano Materials: Volume 8, World Scientific, 2015.

Lawes S, Sun Q, Lushington A, Xiao B, Liu Y, and Sun X. High performance inkjet-printed silicon anodes for lithium-ion batteries. To be submitted.

Lawes S, Sun Q, Guo H, Banis M, and Sun X. High performance inkjet-printed titanium dioxide anodes for lithium-ion batteries. To be submitted.

Zhao Y, Yan B, Li X, Li D, Lawes S, and Sun X. Significant impact of 2D graphene nanosheets on large volume change tin-based anodes in lithium-ion batteries: A review. Journal of Power Sources, 2015.

Sun Q, Wang B, Xiao B, Liu J, Banis M, Yadegari H, Lawes S, Li R, and Sun X. Self-stacked nitrogen-doped carbon nanotubes as long-life air electrode for sodium-air

batteries: Elucidating the evolution of discharge product morphology. *Nano Energy*, 2015.

Pu N, Shi G, Liu Y, Sun X, Chang J, Sun C, Ger M, Chen C, Wang P, Peng Y, Wu C, Lawes S. Graphene grown on stainless steel as a high-performance and ecofriendly anti-corrosion coating for bipolar plates. *Journal of Power Sources*, 2015.

Lushington A, Liu J, Banis M, Xiao B, Lawes S, Li R, and Sun X. A Novel Approach in Controlling the Conductivity of Thin Films using Molecular Layer Deposition. *Applied Surface Science*, in press.

Shan H, Xiong D, Li X, Sun Y, Yan B, Li D, Lawes S, and Sun X. Tailored Lithium Storage Performance of Graphene Aerogel Anodes with Controlled Surface Defects for Lithium-Ion Batteries. Submitted.